The Design and Implementation of Continuous Frequency and Bandwidth Tunable Combline Filters

Submitted in accordance with the requirements for the degree of Doctor of Philosophy

School of Electronic and Electrical Engineering
Pollard Institute
The University of Leeds

James S. Parish

February 2018

Declaration

The candidate confirms that the work submitted is his own, except where work which has formed part of jointly-authored publications has been included. The contribution of the candidate and the other authors to this work has been explicitly indicated below. The candidate confirms that appropriate credit has been given within the thesis where reference has been made to the work of others. Further details of the jointly-authored publications and the contributions of the candidate and the other authors to the work should be included below this statement.

The details of chapters 4 and 5 are based on the following published paper:

Parish, J.S. & Somjit, N. & Hunter, I.C. "Continuous Frequency and Bandwidth Tunable Combline Cavity Bandpass Filters with Internally Mounted Motors" IET Microwaves, Antennas and Propagation. 2018.

The candidate performed all the computational as well as experimental work and wrote the paper. Supervisor (Professor Ian Hunter) provided advice and feedback throughout the undertaking of the work. Doctor Nutapong Somjit proof-read the paper.

Acknowledgements

I would like to express my gratitude to both Radio Design as well as the Engineering and Physical Sciences Research Council (EPSRC) who provide the funding that makes this research possible. The engineers at Radio Design offered their advice on many occasions and the company provided me with access to their facilities when needed.

.

I am very grateful to my primary supervisor, Professor Ian Hunter, under whose supervision I have been given the support and guidance needed for the undertaking of this project. My gratitude also goes to to Dr. Nutapong Somjit for his role as co-supervisor.

.

Additional thanks should be extended to Roland Clarke who selflessly gave up his time in helping to explain the finer details in the usage of equipment in the labs.

.

Lastly I would like to thank my colleagues who have provided daily support to me throughout my PhD.

Abstract

Design methods for the implementation of continuous centre frequency and bandwidth tunability in bandpass filtering structures are presented in this thesis.

Initially, the use of discrete electronic components as providers of tunability are explored for use in planar filters. PIN and varactor diodes are used to control capacitance at key nodes in the circuit through use of voltage or current biasing. The limitations of these devices are explored in terms of linearity. Intermodulation distortion is measured using two-tone characterisation tests.

Configurations of three-dimensional combline filters are analysed using HFSS. Filter structures are treated as a combination of resonant frequencies, external couplings and inter-resonator couplings which control centre frequency, return loss ripple level and bandwidth and respectively. A variety of bespoke components are introduced and compared with each other through simulation for their effectiveness of tunability with actuation.

Novel, and independent techniques for tuning both resonant frequency and coupling bandwidths are proposed and implemented in physical TEM combline filters simultaneously. The method introduced for resonance tuning allows for the mounting of motorised actuators to be internal to the filter cavity — thereby adding the complexity of tunability to the structure without needing to increase the volume.

Two filters of differing complexity incorporating the developed tuning methods (for centre frequency, return loss and bandwidth) are designed and fabricated to the same tuning specifications as each other — centre frequency from 1.8 GHz to 2.0 GHz and bandwidth from 40 MHz to 60 MHz. The first filter is a second-order combline cavity filter capable of bandwidth tunability from 49 MHz to 67 MHz for all centre-frequencies in the range of 1.751 GHz to 1.998 GHz. Passband insertion loss is kept below 1.2 dB for all tuning states with return loss above 10 dB. The second filter is a five-pole design. This filter achieves frequency tunability from 1.764 GHz to 2.015 GHz and 15 dB bandwidth tunability from 41 MHz to 85 MHz. Midband insertion loss is kept below 1.4 dB in all tuned states.

Contents

List of Figures

List of Tables

Chapter 1

Introduction

1.1 Background

EM waves with frequencies from 300 MHz to 3 GHz are designated as the ultra high frequency (UHF) band of the radio frequency (RF) range. These frequencies are used for numerous applications including television broadcasting, GPS, personal radio, Wi-Fi, Bluetooth and cellular communication. Standards are imposed by regulatory bodies in order to fairly allocate particular frequencies of the UHF band for each application.

Due to the Shannon-Hartley theorem, which shows there is a tight upper bound on a channels ability to transfer information per bandwidth, the EM spectrum is shown to be a finite resource. Thus the amount of bandwidth made available for each application is limited. Taking the case of cellular communications; as the number of mobile phones being used continues to rise, coupled with the demand for each new device to require higher data rates the result is a higher demand for an already overcrowded spectrum. It is because of this congestion that regulatory bodies are required to divide and share the spectrum between different users and applications. Thus microwave filters are employed in communications systems to efficiently manage this resource.

RF and microwave filters are an essential part of digital wireless communications systems. They are required in situations where discrimination between wanted and unwanted signal frequencies is required.

Filters can be categorised into four basic types: lowpass, highpass, bandpass and bandstop. In general, all filters are used to either suppress unwanted noise present in a channel, or to reject interference from adjacent communication channels. Lowpass and highpass filters perform the opposite role to each other. Where a lowpass filter allows signals below a cutoff frequency through and rejects signals above, a highpass filter rejects all signals below a cuttoff frequency and frequencies higher. Similarly bandpass and bandstop filters are each others counter example. Where a bandpass filter accepts a given frequency band defined by lower and upper cutoff frequencies

where their difference is the bandwidth. Conversely a bandstop filter will accept all frequencies other than a given band.

Classification of a filters performance is determined by their signal transmission and reflection characteristics with frequency, which can be extracted from the scattering parameter (S-parameter) matrix.

1.2 Motivation

Mobile telephony has been the fastest growing technology to be integrated into everyday life on a global scale. It is estimated that worldwide, there are over 5 billion end user devices in use every day. This number is expected to continue rising sharply over the coming years as the integration of electronic devices to the internet of things (IOT) gains momentum. Since the first commercial rollout of a mobile phone network, the industry has undergone a series of complete paradigm shifts to the industry-wide standards (ie. 2G, 3G, 4G etc.) [1]. Each update in standards, colloquially referred to as a generation, has introduced new technologies as well as a redistribution of the spectrum from the previous generation. Consequently, backwards compatibility between generations is, for the most part, impossible. It follows that for the rollout of a new generation, the infrastructure requires a complete update, while simultaneously maintaining the network already in place. Ultimately this can prove to be an expensive affair. As such, there is a demand to be able to develop parts of the infrastructure that can be selectively adapted to any future changes in the protocols.

Take for example the case of a microwave filter at the front end of a cellular base station transceiver. The ability to have reconfigurable hardware on the front end would benefit the operator by affording the means to efficiently manage the resources currently in place, whilst simultaneously accommodating the requirements of multiple standards, optimising network capacity.

The installation and modification of wireless infrastructure equipment can be costly both rurally; where a remote radio head (RRH) can be the equivalent of 15 stories high to service large areas, and in urban areas; where space is at a premium due to a number of factors including expensive real estate as well as stringent size and weight loading constraints. Therefore network operators naturally incline to use tunable filters in order to include as many multistandard and multiband functions as possible on one site. The added benefit of being electronically tunable, allows for a single installation to be in service for many years by updating the hardware remotely when necessary [2].

1.3 Scope

A typical Cellular basestation transceiver utilises a single antenna to service both transmit and receive channels. There is an inherent difference in signal power amplitudes between the transmit (Tx) and receive (Rx) paths — potentially over 10 orders of magnitude! Consequently, in order to avoid signal leakage from the transmit path damaging the sensitive receiver circuitry, transmit filters need to attenuate heavily in the stop band.

Due to a variety of propagation effects, the communication signal of a wireless link will degrade quite heavily between transmitter and receiver. Thus transmitter and receiver front end filters must have very low internal losses to balance the systems link budget.

Modern commercial cellular basestation filters are required to adhere to strict specifications in order to separate different channels and limit the signal attenuation outside of the wireless link as much as possible.

A filter is typically made up of coupled resonant sections, where the order of the filter is given by the number of resonant sections. The higher order a filter is, the closer it can approximate an ideal response. This comes at the expense of network complexity and consequently the time required to take the filter from the design stages to realised working product.

This thesis will aim provide research on novel methods for achieving bandwidth and centre frequency tunability of RF filters, while also maintaining good insertion and return loss in the passband.

1.4 Organisation of the thesis

Firstly, chapter one explains the need for reconfigurable basestation front-end filters. An overview of the cellular communications system is provided here, with the context of microwave filters specifically highlighted. Objectives of the research are presented in this chapter.

Chapter two presents an overview of the design process of microwave filters from specification to fabrication. Commonly used approximations for filter transfer functions are provided. EM modelling and optimisation techniques are introduced.

A review of the literature is presented in chapter three. Methods for providing tunability and reconfigurability in microwave filters are explored. Characterisation of intermodulation distortion generated by discreet electronic components is introduced. Two types of discrete components are explored for their use in providing tunability in microwave filters — namely varactor and PIN diodes. A two-pole prototype filter

with passband switching provided by PIN diodes is realised in microstrip and measured.

The fourth chapter explores the region in between resonators of a combline cavity filter structure. Through simulated experimental testing, a thorough understanding of the interaction of electric and magnetic fields in the coupling region is developed. A variety of mechanisms to exploit these fields as a means of tuning filter bandwidth are proposed and compared with each other.

Chapter 5 explores methods for performing centre-frequency and external-coupling tuning. Simulation testing is performed using HFSS and tuning methods using both metals and dielectric materials are explored. Additionally, techniques for characterising the coupling bandwidths (inter-resonator and external) are described. The chapter is concluded with the fabrication and measurement of two filters. The first is a second order prototype filter integrating inter-resonator and external coupling tunability along with centre-frequency tuning simultaneously to prodice a fully tunable filter with control over centre-frequency, bandwidth and return loss. The second filter is a a novel mechanically tunable 5-pole filter with both centre frequency and bandwidth control. Control of tuning by a small commercial 6 mm diameter motor housed within the filter cavity is also demonstrated.

Chapter 6 concludes the thesis and provides some insight into potential future projects and their applications.

Chapter 2

Microwave Filter Design Procedure

2.1 Overview of Microwave Filter Design Procedure

A general method for obtaining a working physical microwave filter has become well established process over a number of decades. The fundamental steps are illustrated in figure 2.1. Design begins with the generation a filter transfer function to satisfy the required attenuation levels of the filter specifications. Next a generalised lowpass prototype network is synthesised with characteristic impedance of 1 Ω and a cutoff frequency of 1 $\mathrm{rad\,s^{-1}}$, before being converted into highpass, bandpass or bandstop filtering configurations. Additional transformations can be applied at this stage to determine the characteristic impedance and operating frequency of the network specific to the criteria. Finally the filter is implemented in a physical structure such as microstrip, coaxial cavity, waveguide or ceramic. Filter specifications typically concern centre frequency, bandwidth, passband insertion loss, return loss and selectivity. The Q-factor of resonators determines the passband insertion loss and selectivity of a filter.

A transfer function is defined by the specifications at the beginning of the procedure. Increasing the order of the filter increases the selectivity at the expense of the in band insertion loss. As a result, transmission zeroes can be added to the filter response in

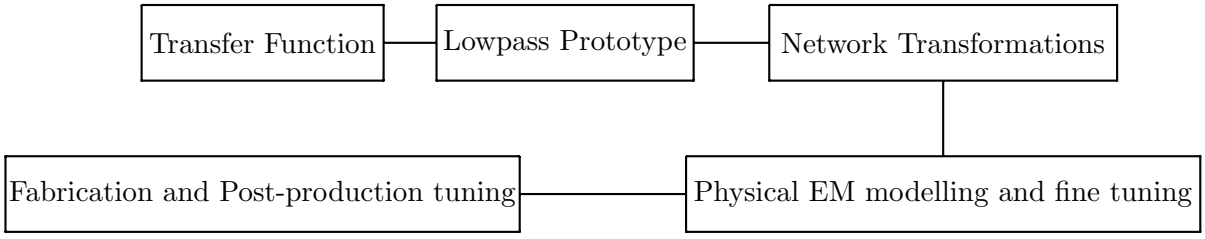

Figure 2.1: A block diagram of the complete filter design process.

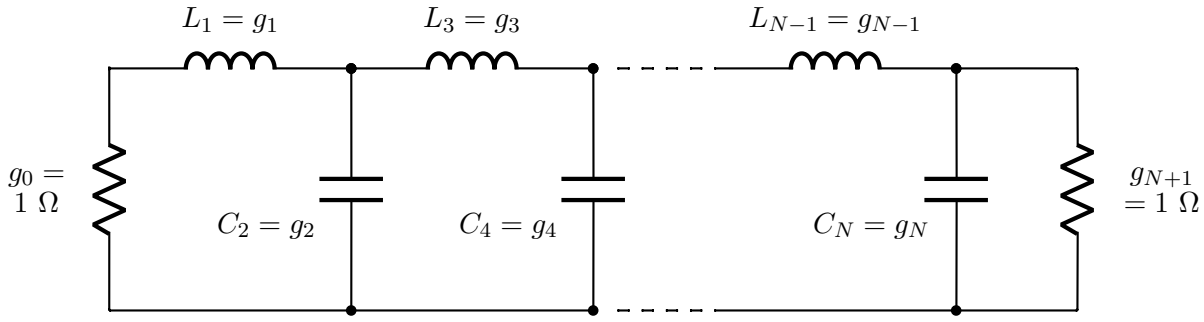

Figure 2.2: Low pass prototype ladder network

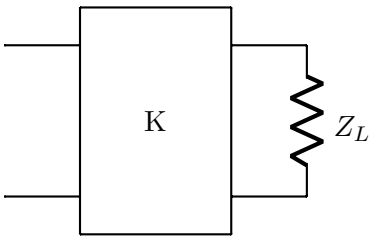

Figure 2.3: Impedance inverter terminated with load Z_L

order to increase the selectivity without increasing the number of reactive components. The realisation of transmission zeroes can be achieved in a number of ways, such as the introduction of cross-coupled paths or using extracted pole techniques [3]. Microwave filters can be designed by applying lumped element ladder network synthesis [4]. For more complex filter configurations, especially those with complicated cross-couplings, a coupling matrix approach can be utilised in order to simplify the process [5].

After applying conversions to generate physical dimensions of a filter it is necessary to optimise using simulation tools in order to correct the effects of approximations. In practice, filters are designed with post production tuning mechanisms, usually adjustable screws fixed with a nut, to compensate for tolerances in the manufacturing process.

2.2 Lowpass Prototypes

A lowpass prototype is a two-port, passive, reciprocal network with a normalised impedance of 1 Ω. It is designed such that it has a cutoff frequency at $\omega = 1\ \mathrm{rad\,s^{-1}}$. The network is designed to meet a specified criteria for passband return loss, RL and stopband insertion loss, IL. Given that the network is considered to be lossless, the inband insertion loss is linked to the passband return loss by the unitary condition. The prototype can be specified in either lumped or distributed element format. As mentioned previously, transformations can later be applied in order to convert the network into any type of filter of arbitrary bandwidth and frequency of operation. Figure 2.2 above shows a normalised lowpass prototype filter.

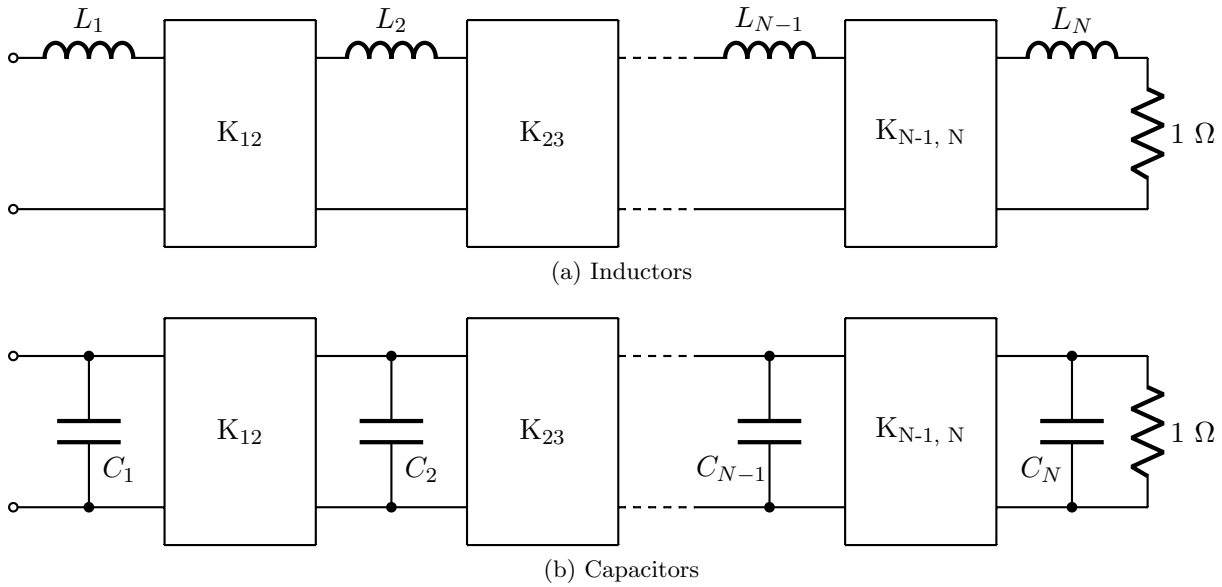

(a) Inductors

(b) Capacitors

Figure 2.4: Inverter coupled low pass prototype

Alternatively, ladder networks can be realised using elements called impedance (or admittance) inverters shown in figure below. Impedance inverters are lossless reciprocal two-port networks with frequency independence. They are defined by the transfer matrix:

$$\left[T\right] = \begin{bmatrix} 0 & jK \\ {}^{j}/_{K} & 0 \end{bmatrix} \tag{2.1}$$

Where K denotes the characteristic impedance or admittance of the inverter. It relates the input impedance to the load impedance as follows:

$$Z_{in} = \frac{K^2}{Z_L} \tag{2.2}$$

And so the input impedance is inversely proportional to the load impedance.

Applying an inverter to a ladder network allows for the network to be designed using only one type of reactive element as shown in figure 2.4. There are a number of response shapes that can be designed in the prototype stage in order to exploit a given trait. For example, Butterworth (or maximally flat) prototypes (figure 2.5(a)) are designed such that the amplitude response approximates zero gradient at the centre frequency. Consequently this means that the filter rolls off slowly to 3 dB at $\omega = 1$. On the other hand, an elliptical filter function is designed to ripple in both the passband and stopband in order to produce a very sharp transition between the passband and stopband. This is afforded at the expense of the ability to arbitrarily define transmission zeroes. The Chebyshev prototype (figure 2.5(b)) provides a decent trade-off between the Butterworth and Elliptic prototypes. It utilises ripples in the passband between two amplitude values to achieve a steep rolloff to the stopband. There are several transfer functions that approximate the lowpass prototype depending on the nature of the ripples in the passband and stopband.

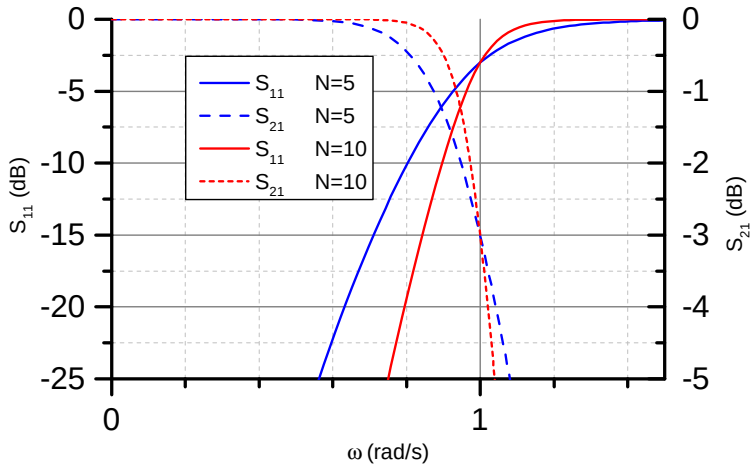

(a) Butterworth (maximally-flat) low pass response

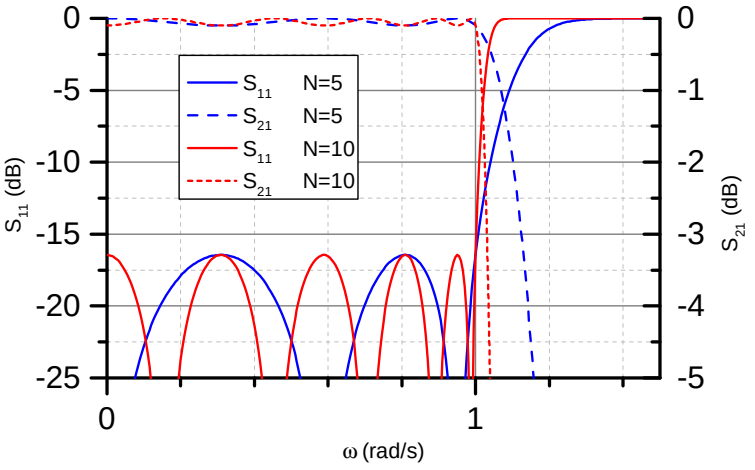

(b) Chebyshev low pass response

Figure 2.5: Prototype responses of different low pass approximations with cutoff frequency $\omega_c = 1$ rad s^{-1}

For a Chebyshev prototype transfer function, it is given that

$$|S_{21}(j\omega)|^2 = \frac{1}{1+\epsilon^2 T_N^2(\omega)} \tag{2.3}$$

Where ϵ relates to the ripple in the passband and $T_N(\omega)$ is the Chebyshev polynomial. S_{21} is the forward transmission coefficient which represents the ratio of signal power at the output relative to the power incident to the network. It is often referenced in terms of decibels, known as the insertion loss (IL) which represents the attenuation of a signal passing through the network.

$$IL(\omega) = -10\log|S_{21}(j\omega)|^2 \quad dB \tag{2.4}$$

The forward transmission (S_{21}) and input reflection (S_{11}) coefficients of a lossless two-port network are related by the unitary condition as follows

$$|S_{11}(j\omega)|^2 + |S_{21}(j\omega)|^2 = 1 \tag{2.5}$$

The input reflection is also referenced in terms of decibels denoting the attenuation of the reflected signal. In this format it is known as the return loss (RL).

$$RL(\omega) = -10log|S_{11}(j\omega)|^2 \quad dB \tag{2.6}$$

Return loss provides a measurement on how well matched a filter is. When a filter is perfectly matched the return loss would be infinite. Returning to equation 2.3 it was stated that ϵ relates to the passband ripple. It is given by

$$\epsilon = \frac{1}{\sqrt{10^{\frac{RL}{10}}-1}} \tag{2.7}$$

Where RL in this case is the desired minimum passband return loss ripple level in decibels.
$T_N(\omega)$ is the Nth order Chebyshev polynomial given by the formula:

$$T_N(\omega) = \cos\left\{N\cos^{-1}(\omega)\right\} \tag{2.8}$$

The degree of a Chebyshev filter for a specified passband ripple and stopband rejection level can be calculated using the following formula

$$N \geq \frac{IL + RL + 6}{20\log\left(S + \sqrt{S^2-1}\right)} \tag{2.9}$$

Where IL and RL are the minimum specifications of stopband insertion loss and passband return loss respectively. S denotes the desired selectivity of the filter calculated as the ratio of stopband to passband frequencies.

In order to calculate a general N$^{\text{th}}$ order Chebyshev prototype another parameter, η,

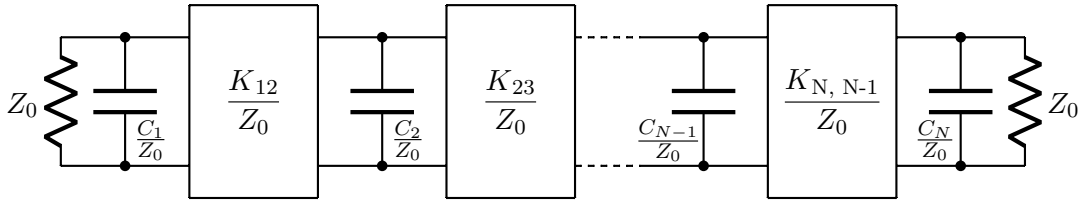

Figure 2.6: An impedance transformed inverter coupled lowpass prototype with shunt capacitances

is introduced, where:

$$\eta = \sinh\left\{\frac{1}{N}\sinh^{-1}\frac{1}{\epsilon}\right\} \tag{2.10}$$

Thus impedance inverters are given by:

$$K_{r,r+1} = \frac{\sqrt{\eta^2 + \sin^2\left(\frac{r\pi}{N}\right)}}{\eta} \qquad r = 1, 2, \ldots, N-1 \tag{2.11}$$

And the reactive elements of an inverter-coupled Chebyshev lowpass prototype are calculated as follows:

$$L_r = C_r = \frac{2}{\eta}\sin\left\{\frac{(2r-1)\pi}{2N}\right\} \tag{2.12}$$

2.2.1 Impedance transformation

Low pass prototype filters are designed such that they give a normalised lowpass response with cutoff frequency $\omega_c = 1\ \mathrm{rad\,s^{-1}}$ for a source and load impedance of 1 Ω. In reality, most communications subsystems are matched to 50 Ω. In order to convert from a 1 Ω impedance to an arbitrary impedance of Z_0 Ω, the impedance of each element must be scaled by a factor of Z_0. Therefore for an inductor:

$$L' = Z_0 L \tag{2.13}$$

$$C' = \frac{C}{Z_0} \tag{2.14}$$

$$K' = Z_0 K \tag{2.15}$$

Where L', C' and K' represent the post impedance transformation variants of inductance, capacitance and inverter impedance respectively. Note that for an admittance inverter, $K' = K/Z_0$ should be used instead. Figure 2.6 shows an example of an inverter coupled network with the impedance tranformation applied. Here admittance inverters have been used.

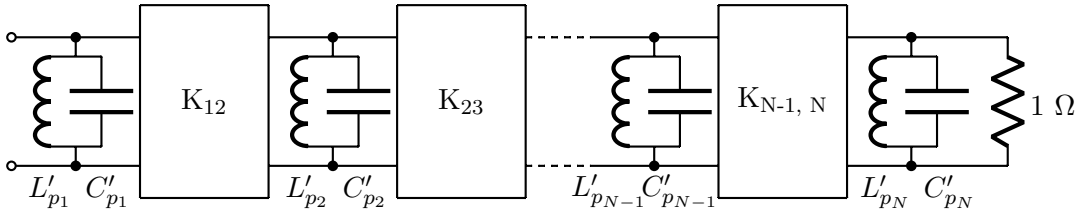

Figure 2.7: Inverter coupled shunt-C circuit after bandpass transformation

2.2.2 Bandpass transformation

The lowpass prototype can be transformed into a bandpass filter with arbitrary bandwidth and centre frequency. The band edges of the lowpass prototype at $\omega = \pm 1\ \mathrm{rad\,s^{-1}}$ are mapped to the band edges of the bandpass filter at ω_1 and ω_2. The following transformation is used in order to attain this:

$$\omega \mapsto \alpha \left(\frac{\omega}{\omega_0} - \frac{\omega_0}{\omega} \right) \tag{2.16}$$

Where

$$\alpha = \frac{\omega_2 - \omega_1}{\omega_0} \tag{2.17}$$

And

$$\omega_0 = \sqrt{\omega_1 \omega_2} \tag{2.18}$$

Where α is the reciprocal of the fractional bandwidth, referred to as the bandwidth scaling factor and ω_0 is the centre frequency of the passband.

When applying the bandpass transformation to a series inductance L, a series LC resonant circuit is formed where the resultant capacitance, C'_s, and inductance, L'_S, are given by:

$$L'_s = \frac{\alpha L}{\omega_0} \tag{2.19}$$

$$C'_s = \frac{1}{\alpha L \omega_0} \tag{2.20}$$

Conversely a shunt capacitor from the lowpass prototype is transformed into a parallel resonant LC circuit with element values:

$$L'_p = \frac{1}{\alpha C \omega_0} \tag{2.21}$$

$$C'_p = \frac{\alpha C}{\omega_0} \tag{2.22}$$

Due to the frequency independence of impedance and admittance inverters they remain unaffected by bandpass transformations. Figure 2.7 shows the resultant circuit from figure 2.4 (b) after the bandpass transformation has been applied.

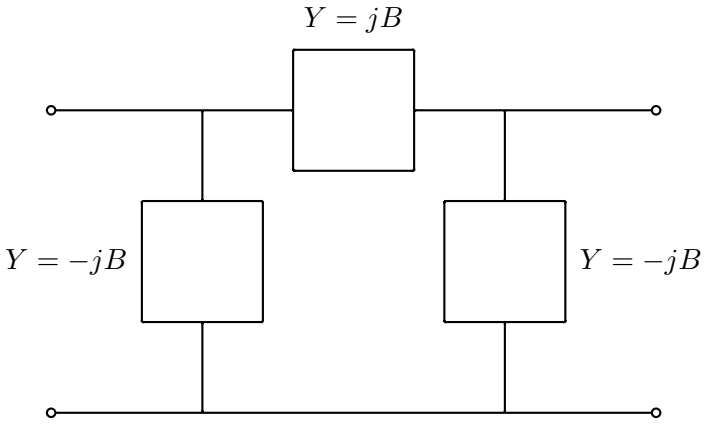

Figure 2.8: Equivalent of an inverter using a pi-network of susceptances

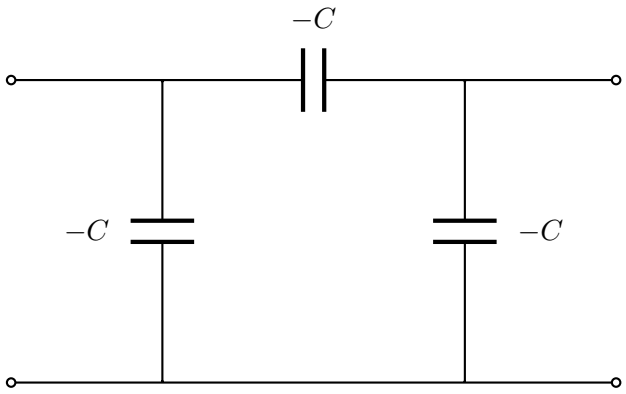

Figure 2.9: Narrowband approximation of an inverter

2.2.3 Realisation of an inverter

As individual elements, inverters cannot exist in the real world. They can be formed however, by using a pi-network of shunt negative susceptances jB and a series positive susceptance of $+jB$ as shown in figure 2.8. The transfer matrix of this network is

$$\left[T\right] = \begin{bmatrix} 0 & {}^{-j}/_{B} \\ -jB & 0 \end{bmatrix} \tag{2.23}$$

Which is equivalent to an admittance inverter where

$$K = -B \tag{2.24}$$

$$Y = jB = j\omega C \tag{2.25}$$

Therefore

$$K = -\omega C \tag{2.26}$$

The negative shunt capacitances are absorbed by the larger positive capacitances of the resonators. It is of interest to note that the inverters are now frequency dependent. This means that inverter coupled filter networks are only suitable for sufficiently nar-

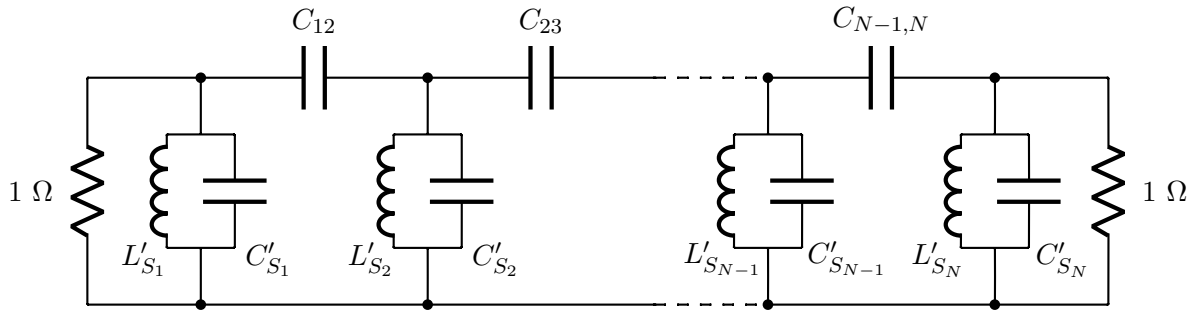

Figure 2.10: A capacitively coupled bandpass filter

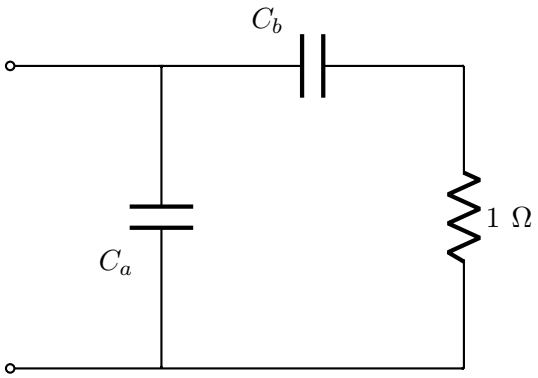

Figure 2.11: Narrowband impedance transformer

rowband applications. Filters with less than 10% fractional bandwidth are considered acceptable for this type of application. Replacing the inverters from figure 2.4 (b) with a pi network of capacitors results in the formation of a capacitively coupled bandpass filter 2.10

2.2.4 Narrowband impedance transformer

The frequency dependence of the capacitive inverters presents another issue. The filter bandwidth must be sufficiently narrowband for the inverters to work properly, however with reference to equation 2.19 it can be seen that very narrowband filters would result in inductances too small to be realisable in practice. In order to counter this and allow for realistic inductance values the network admittance should be scaled by a factor of $1/\alpha$. This makes the element values independent of the filter bandwidth. A narrowband transformer can be approximated by a two capacitor circuit shown in figure 2.11. Where

$$C_a = \frac{-\sqrt{\alpha - 1}}{\omega_0 \alpha} \tag{2.27}$$

And

$$C_b = \frac{1}{\omega_0 \sqrt{\alpha - 1}} \tag{2.28}$$

C_b becomes the series coupling from and to the source and load respectively, and C_a is absorbed into the first and last resonators of the filter.

2.3 Distributed Network Filters

Lumped element filters are by definition zero-dimensional. In other words they are significantly smaller than the wavelength at the operating frequency. At microwave frequencies lumped element theories become impractical since circuit elements can easily have dimensions comparable to a quarter-wavelength. It becomes practical to model lumped element circuits in terms of distributed circuit networks.

Components based in transmission line theory are used when designing practical filters. For frequencies of 300 MHz to 30 GHz, filters are typically realised in microstrip, stripline and coaxial cavities. At higher microwave frequencies of 30 GHz to 300 GHz, dielectric and waveguide resonators are utilised due to the diminished waveguide dimensions at these frequencies. Other parameters for consideration are defined by constraints in unloaded quality factor, power handling and physical size for the given application when choosing the application technology [3].

A unit element (UE) is a basic section of lossless line. Assuming sinusoidal excitation, a UE has the following transfer matrix:

$$\left[T\right] = \begin{bmatrix} \cos(\beta l) & jZ_0 \sin(\beta l) \\ jY_0 \sin(\beta l) & \cos(\beta l) \end{bmatrix} \tag{2.29}$$

Where l is the physical length of the line, and Z_0 is its characteristic impedance. β is known as the propagation constant which is defined as:

$$\beta = \frac{2\pi}{\lambda} \tag{2.30}$$

The product of β and l gives the electrical length, θ of the line. Since the electrical length is proportional to frequency it can be written as:

$$\beta l = \theta = a\omega \tag{2.31}$$

Where a is the ratio of line length, l, to velocity of propagation, v.

$$a = \frac{l}{v} \tag{2.32}$$

Thus for a UE

$$\left[T\right] = \begin{bmatrix} \cos(a\omega) & jZ_0 \sin(a\omega) \\ jY_0 \sin(a\omega) & \cos(a\omega) \end{bmatrix} \tag{2.33}$$

And for complex frequencies

$$\left[T\right] = \begin{bmatrix} \cosh(as) & Z_0 \sinh(as) \\ Y_0 \sinh(as) & \cosh(as) \end{bmatrix} \tag{2.34}$$

$$= \frac{1}{\cosh(as)} \begin{bmatrix} 1 & Z_0 \tanh(as) \\ Y_0 \tanh(as) & 1 \end{bmatrix} \tag{2.35}$$

Where s is the complex frequency variable of the form

$$s = \sigma + j\omega \tag{2.36}$$

Therefore letting

$$t = \tanh(as) \tag{2.37}$$

Gives

$$\Big[T\Big] = \frac{1}{\sqrt{1-t^2}} \begin{bmatrix} 1 & Z_0 t \\ Y_0 t & 1 \end{bmatrix} \tag{2.38}$$

Circuits consisting of interconnections of commensurate lines can be defined in terms of rational polynomial functions of t.

It is possible to borrow from lumped theory to design certain types of filter. This is achieved by applying Richards transformation [Richards 1948] as follows:

$$\omega \mapsto \alpha \tan(a\omega) \tag{2.39}$$

Or

$$s \mapsto \alpha \tanh(as) \tag{2.40}$$

For a capacitor in the complex frequency domain, applying the Richards transformation gives:

$$Y(s) = sC \mapsto \alpha C \tanh(as) \tag{2.41}$$

Where

$$Y_0 = \alpha C \tag{2.42}$$

Therefore

$$Y(s) = Y_0 \tanh(as) \tag{2.43}$$

Applying the same transformation to an inductor gives:

$$Z(s) = sL \mapsto \alpha L \tanh(as) \tag{2.44}$$

Where

$$Z_0 = \alpha L \tag{2.45}$$

And so

$$Z(s) = Z_0 \tanh(as) \tag{2.46}$$

Taking equations 2.43 and 2.46 it can be seen that the conversion of a lumped element inductor and capacitor into their distributed forms results in a short circuited stub and an open circuited stub respectively. This has been illustrated in figure 2.12.

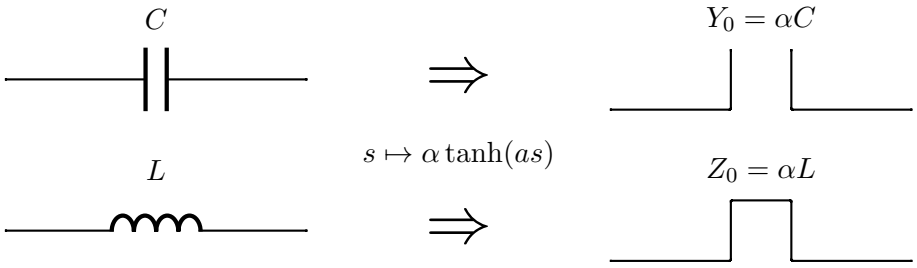

Figure 2.12: Richards' transformation of passive lumped elements

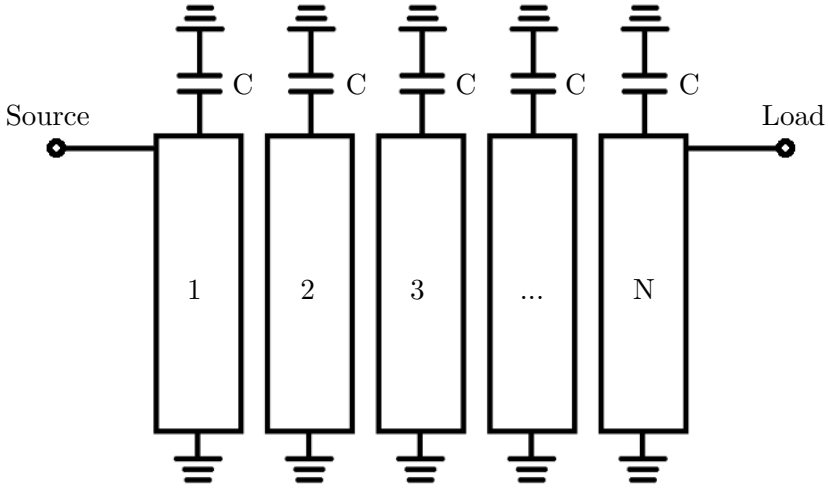

Figure 2.13: An N^{th} order Combline filter.

2.3.1 The Combline Filter

A combline filter is a filter that consists of an in-line array of coupled commensurate length TEM transmission lines where coupling is restricted to neighbouring pairs as in figure 2.13. Each line is short circuited at one end (the same end for each line). The opposite ends are loaded to ground via a capacitor. Without the capacitors present in the circuit, the TEM lines would resonate at their quarter-wave freqeuncy. Similarly so would the couplings between them — creating an all stop network. The presence of the capacitors forces the TEM lines to act as inductors. Consequently they resonate with the capacitors below the quarter wave frequency. The couplings are fairly weak in comparison to other filter types (such as the interdigital filter), meaning that resonators can be spaced closer together. This added to the fact that the line lengths can be significantly less than a quarter wavelength means that a combline filter can provide considerable volume savings for a filter of a prescribed centre frequency and bandwidth.

The Combline filter has an equivalent circuit made up of characteristic impedances with commensurate electrical lengths and capacitance, which is illustrated in figure 2.14. The values for each characteristic impedance, Z, and capacitance, C, can be calculated for an arbitrary electrical length using the design procedure in [4]. After which, three-dimensional structure dimensions can be estimated by calculating

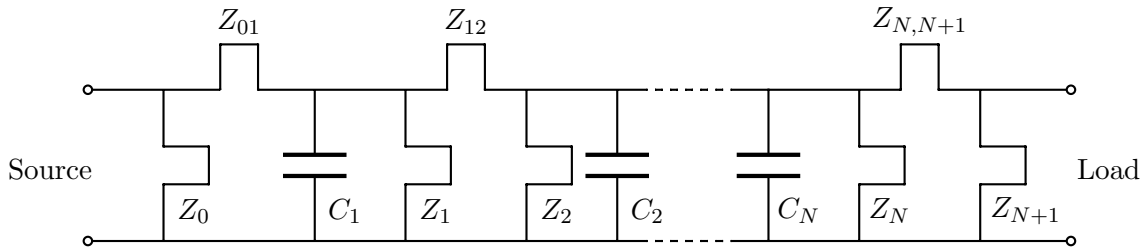

Figure 2.14: The equivalent circuit for a Combline filter.

even/odd mode capacitances as well as static capacitance to ground and using the data provided by Getsinger [6] for rectangular structures or Cristal [7] for cylindrical structures.

2.4 Design and Fabrication Procedures

2.4.1 Electromagnetic Modelling and Optimisation

Once a filter has been synthesised and a suitable implementation for the design has been chosen, electromagnetic field simulator software is used to model, analyse and optimise the design to ensure it meets the requirements. High Frequency Structure Simulator (HFSS) from ANSYS provides a powerful piece of software to perform this task. It provides an interactive graphical user interface environment which allows the user to build a three-dimensional model of their design from a built-in database of real-world materials cataloguing their electrical properties (permittivity, permeability, conductivity, loss tangent etc.). The user has the ability to edit existing material properties as well as create new materials with custom properties of their choice. HFSS can be used to simulate a variety complex three-dimensional microwave components using field solvers based on the finite element method (FEM), integral equation and hybrid methods. The eigenmodes or resonances of a structure can be calculated along with unloaded-Q and field patterns at resonance using the eigenmode solution type. Scattering parameter solutions can be attained through the driven mode solution type. Here the simulator applies an external source of energy to a physical access port in the structure in order to determine the incident and reflected powers of waveguide modes for discrete frequency points in the desired spectrum.

When a driven solution simulation has been initiated by the user, the simulator first defines a triangulated mesh to approximate the surface textures of the model. A tetrahedral mesh is then generated from the triangulated surfaces across the entire three dimensional structure. The mesh is refined based on electromagnetic fields that exist in those regions when excited at the solution frequency. An error value is calculated in each region of the mesh based on differences in S-parameter magnitudes between one refinement and the next. For regions where the error is large, tetrahedra are refined and another solution is generated. This process iteratively continues to adapt the mesh

until the maximum error for each element in the model falls below a defined threshold. At this point the mesh is deemed to have converged and solutions are calculated for each frequency point in the desired sweep. Accuracy of the results increase with the resolution of the mesh at the expense of computational complexity. The convergence criteria can be modified by the user in order to trade-off between accuracy and runtime.

The modelling and simulation of a structure in HFSS allows the designer to tweak aspects of a design without having to incur the necessary material, labour and temporal costs involved in the production of a prototype. This affords the opportunity to optimise the design to the exact specifications and limits the possibility of faulty hardware being produced when finally fabricated.

2.4.2 Fabrication and post-production tuning

Fabrication of a Combline cavity filter is a conceptually simple process. It starts with a single block of metal cut to the size of the outer dimensions of the filter. Mechanical machining tools cut away sections inside the block to form the cavity to the specified dimensions leaving just the resonators and cavity walls from the original block. A lid is then fashioned and securely attached with screws to the base block. If the situation arises where a gap between two parts of the filter is too small for a machining drill to pass through, these parts can be fabricated separately and either pressed or screwed into the cavity base. It is often the case that transformers are attached to the base in this way due to the small spacing between them and the first resonator.

As with any mechanical process, there is a tolerance involved in the fabrication procedure due to the capabilities of the machining processes and tools used. Any minor imperfection can cause a discrepancy in the desired response of the filter. In order to account for this, filter designs are made with the acceptance that resultant hardware will not be perfect. Tuning screws are strategically introduced at designated sections of the hardware in order to electrically correct for any deviations in the response. These screws are typically inserted through the cavity lid over resonators, where tuning of the screws alters the resonance. Additional screws may also be added in order to correct the couplings.

2.5 Review

This chapter provides a brief overview of the full filter design process from the definition of a transfer function based on the desired attenuation levels, through to physical implementation of a design in an appropriate technology — in this case, with context to this work, narrowband Combline cavity filters are presented. Firstly a normalised lowpass prototype filter is synthesised from the transfer function. Transformations are

then applied in order to achieve bandpass characteristics of arbitrary frequency, bandwidth and termination impedances. The Combline model is presented and described by its circuit model, from which three-dimensional structures can be designed and optimised using electromagnetic field structure simulator software. Finally the filter is realised in an appropriate material and tuning screws are added in order to counter the effects of tolerance in the mechanical processes.

Chapter 3

Reconfigurable Microstrip Bandpass Filter

3.1 Uses of Discrete Components for Tunable Applications

3.1.1 Background

The earliest types of tunable filters were mechanically tuned. They suffered however, from being too bulky and having tuning speeds too slow for applications in the communications industry. *Yttrium-Iron-Garnet* (YIG) filters utilise a phenomenon of a changing ferromagnetic response frequency in YIG spheres as a function of an externally applied DC magnetic field [8]. Despite exhibiting multi-octave tuning ranges and high Q-factors (up to 10'000) [9], YIG filters are large in size and difficult to integrate with *monolithic microwave integrated circuits* (MMIC). Furthermore, due to the inherent hysteresis of a ferromagnetic device, the tuning speed of a YIG filter is limited to the order of GHz/ms.

When it comes to electronically tunable filters a number of techniques can be exploited. Many methods utilise a variation in capacitance in order to alter the frequency of resonators. An ideal capacitor is a two-terminal electrical component that stores energy in the electric field between two electrical conductors separated by a layer of dielectric insulation as shown in Figure 3.1. When a positive charge forms at one terminal it applies an electrostatic force on the charge carriers at the second terminal, causing a negative charge of the same magnitude to be observed on the other terminal.

Due to this effect, dc signals are blocked from passing between the terminals. When driving a terminal with an alternating current however, only a difference in the amplitude and phase of the signal will be seen on the opposite terminal; leaving the frequency component of the signal intact. The current flowing is proportional to the time derivative of the potential difference across the terminals. The constant of proportionality

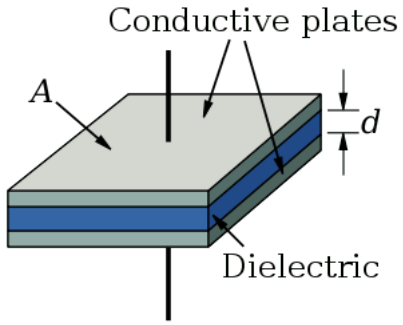

Figure 3.1: A parallel plate capacitor

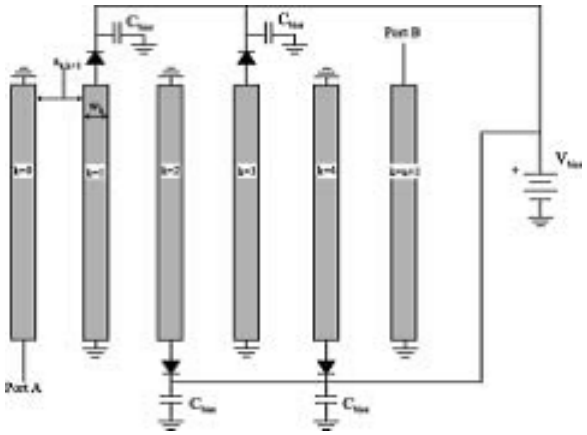

Figure 3.2: Topology of a varactor loaded interdigital bandpass filter [11].

is referred to as capacitance [10]:

$$i(t) = C\frac{dV}{dt} \tag{3.1}$$

The capacitance, C, is proportional to the ratio of the conductive plate area, A, to the separation distance between the conductors, d, such that:

$$C = \frac{\varepsilon A}{d} \tag{3.2}$$

Where ε is the permittivity of the insulator.
It is clear from equation 3.2 that capcitance can be tuned by controllably adjusting either of the insulator permittivity, the conductor plate area, or the plate separation distance.

3.1.2 Varactor Diodes

Semiconductor varactors exploit the change in the depletion region width of a p-n junction diode as a function of reverse bias; effectively controlling the plate separation distance of a capacitor. Varactor diodes typically exhibit low Q-factors and suffer from poor intermodulation performance. The junction capacitance is dependent upon the magnitude of the bias voltage. RF signals of the same order as the tuning voltage can

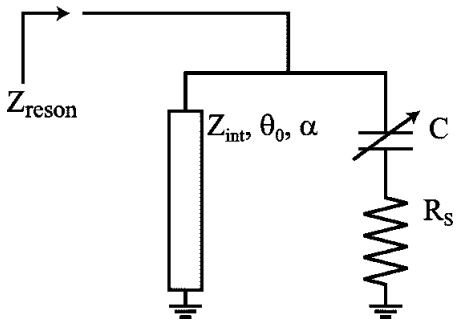

Figure 3.3: Model of varactor loaded transmission line resonator [11]

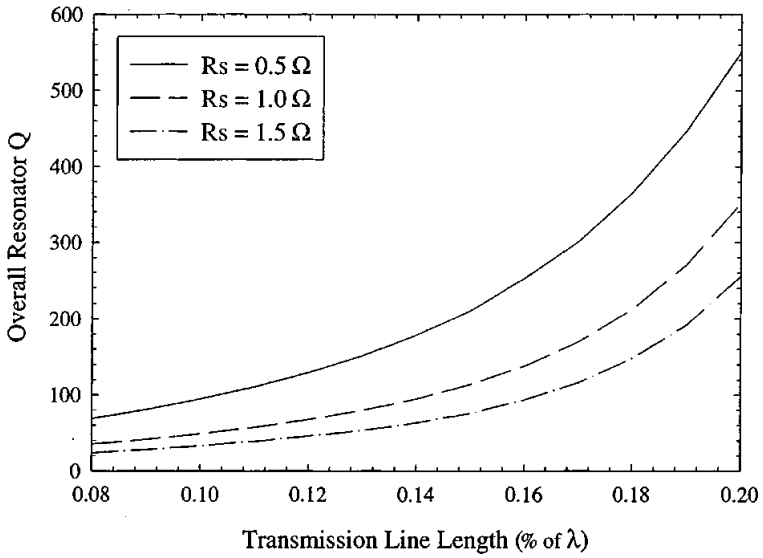

Figure 3.4: Overall resonator quality factor a function of transmission-line length for a transmission-line quality factor of 1030 [11].

modulate the capacitance of the junction. Under these conditions distortion can occur. For this reason varactors are not ideal for high power applications. Nevertheless, the properties of semiconductor varactors for uses in tunable filters are being extensively explored.

Brown and Rebeiz [11] discuss the impact of varactor series resistance and the electrical length of a distributed resonator on the overall resonator quality factor and filter insertion loss. They fabricated an interdigital filter in suspended substrate stripline where the capacitive loading of the resonators was provided by commercially available varactors in a parallel bias configuration as shown in Figure 3.2. Large capacitors were added to allow for the bias. The suspended substrate allowed for a very low effective dielectric constant therefore allowing the use of low-loss, wide transmission lines.

The structure is easily replicated in batch and therefore could be produced cheaply in large quantities. However, this configuration means that the inter-resonator coupling is fixed, and so despite the bandwidth changing over the tuning range, there is no way of controllably a desired bandwidth.

Each resonator can be shown as an equivalent circuit of a transmission line in parallel

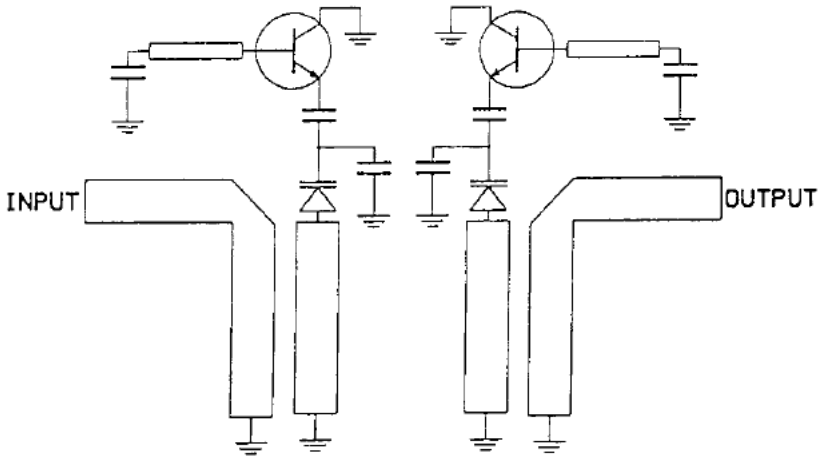

Figure 3.5: Schematic view of active varactor tunable combline filter [12].

with a varactor to ground as shown in Figure 3.3. Where R_S is the series resistance of the varactor and α is the loss of the transmission line.

The authors show that for small transmission line lengths the overall resonator quality factor is heavily influenced by the varactor's series resistance. Increasing the electrical length of the transmission line causes the overall resonator quality factor to become strongly dependent on the quality factor of the transmission line, illustrated in Figure 3.4.

The low quality factor of a varactor leads to a high insertion loss seen in a filter implemented with a varactor.

Chandler and Hunter [12] looked at ways of mitigating this characteristic high insertion loss by exploiting the negative resistance provided by transistors in a tunable two-pole combline structure shown in Figure 3.5.

The filter, fabricated in microstrip, has a centre frequency of 1.8 GHz and is tunable from 1.4 GHz to 2.2 GHz. Without the active transistor providing negative resistance, an insertion loss of between 4 dB to 5 dB is observed in Figure 3.6.

The measured response of the active filter is shown in Figure 3.7. By including active transistors in the filter, the measured return loss was shown to be better than 15 dB and presented a flat, zero insertion loss pass band.

The drawback of this type of filter lies in the nonlinear effects of the components implemented in the design. The nonlinearities lead to mixing products of tones at the input being generated within the filter. Nonlinear effects are characterised by the 1 dB compression point and the IP3 point for intermodulation distortion products which fall within the passband.

As shown in Figures 3.8 and 3.9, active varactor tunable bandpass filters would only be useful for low input power signals of less than a milliwatt. The 1 dB compression points for the active and passive filters are -1 dBm and 9 dBm respectively and both

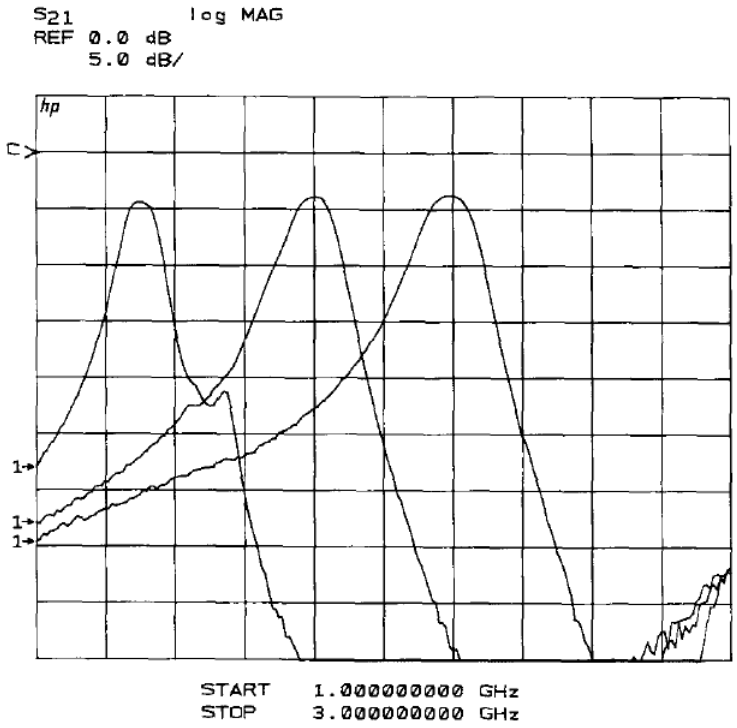

Figure 3.6: Performance of a varactor tunable passive filter [12].

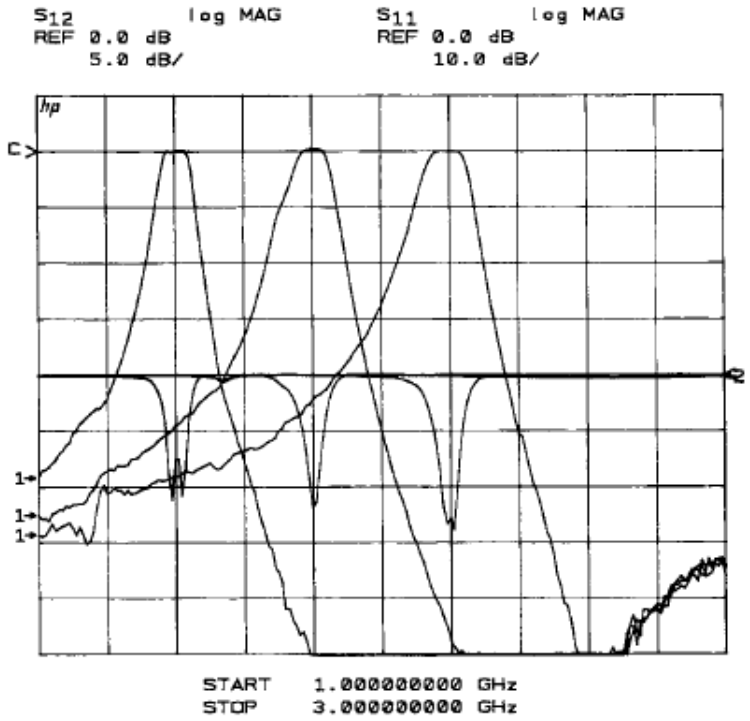

Figure 3.7: Performance of varactor tunable active filter [12].

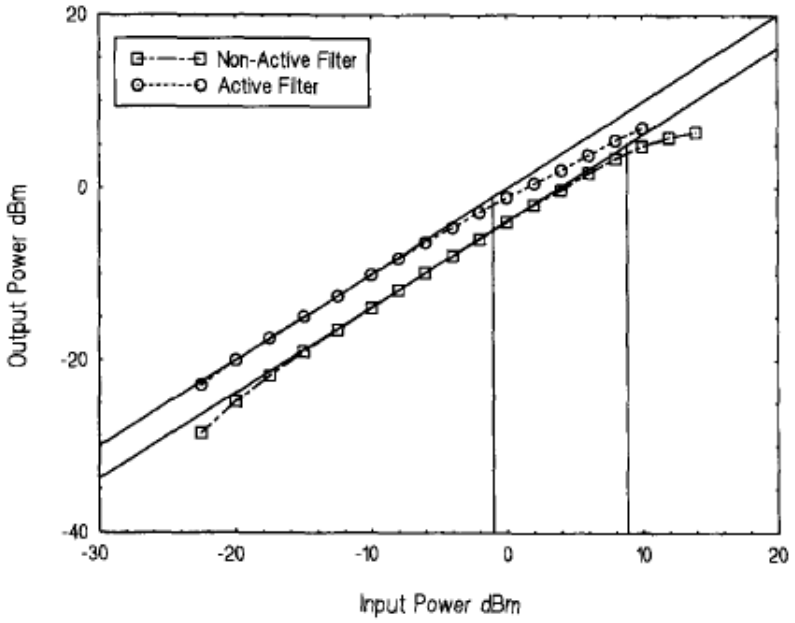

Figure 3.8: 1-dB compression curves at 1.8GHz [12].

filters exhibited a third-order intercept power of $P_{IP3} < 15$ dBm.

Buiseman et al. [13] propose a special case of varactor topology which theoretically provides no second- or third-order distortion.

The capacitance of a single varactor is given by equation 3.3:

$$C(v) = \frac{K}{(\phi + V)^n} \tag{3.3}$$

Where ϕ is the built-in junction potential, K represents the capacitance constant of the junction, V is the applied voltage, and n is the power law exponent of the diode capacitance. When a dc voltage is applied to the junction, the capacitance can be expressed as a function of incremental voltage, v:

$$C(v) = C_0 + C_1 v + C_2 v^2 + \ldots \tag{3.4}$$

Where the C_1 and C_2 terms give rise to the second- and third-order distortion products respectively.

By placing two diodes in an anti-series configuration as shown in Figure 3.10, a case where cancellation of third-order distortion arises.

Where D_A and D_B refer to the diode areas, and the ratio of D_B/D_A is s. The nonlinear

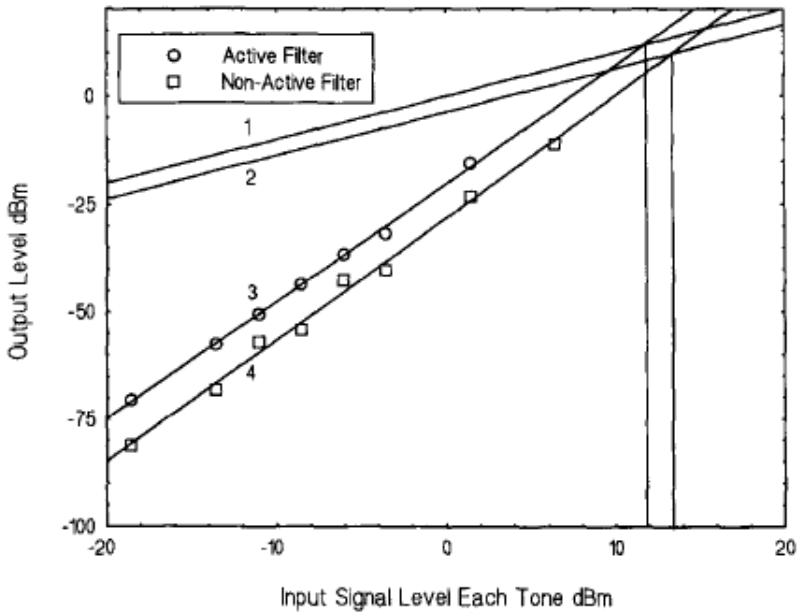

Figure 3.9: Two-tone 3rd order input intermodulation curves at 1.8 GHz centre frequency for active and passive filter. 1) Wanted signal active filter. 2) Wanted signal passive filter. 3) 3rd order IM products active filter. 4) 3rd order IM products passive filter [12].

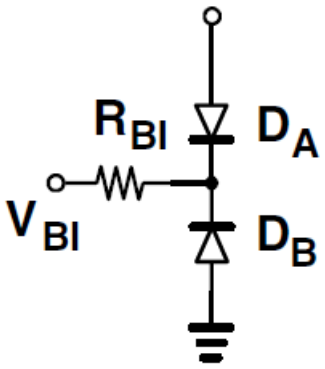

Figure 3.10: Anti-series connection of varactor diodes [13].

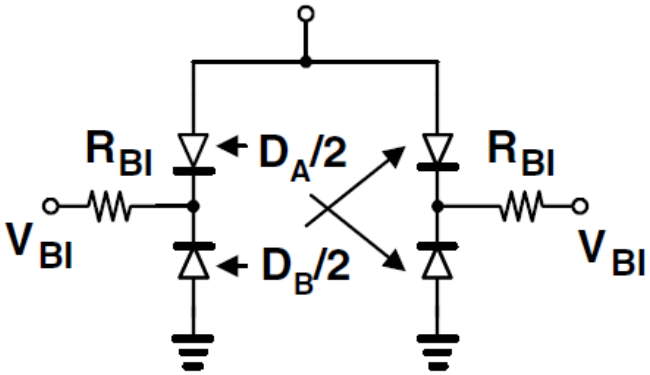

Figure 3.11: Anti-series anti-parallel connection of varactor diodes [13].

terms of capacitance in this case are given by:

$$C_1 = \frac{(1-s)nC_0}{(1+s)(\phi + V_{dc})} \tag{3.5}$$

And

$$C_2 = \frac{C_0[(s^2+1)(n+1) - s(4n+1)]}{2(\phi + V_{dc})^2(s+1)^2} \tag{3.6}$$

Where C_2 in (3.6) can be reduced to zero by setting:

$$s = \frac{4n + 1 + \sqrt{12n^2 - 3}}{2(n+1)} \tag{3.7}$$

The special case of $n = 0.5$ and $s = 1$ sets both C_1 and C_2 to zero, theoretically leading to a distortion-free operation. In cases where $s \neq 1$, C_1 will have a finite value and due to secondary mixing of the fundamental product with the second order product third-order intermodulation distortion will be present in the signal.

Fortunately this too can be cancelled using the anti-series anti-parallel *distortion-free varactor stack* (DFVS) configuration shown in Figure 3.11:

Linearity degradation occurs when the AC current through the bias network becomes significant compared to the desired AC current through the diodes in the varactor stack. The authors do not explicitly give third-order intercept or 1-dB compression measurements, however a significant improvement in IM3 for a single varactor is shown in Figure 3.12 when employing a DFVS. It compares the measured and simulated third-order intermodulation components as a function of power for tone spacings of 100 kHz and 10 MHz. It can be seen from the measured data that the intermodulation power levels were up to 30 dB lower than the predicted levels for the individual diode.

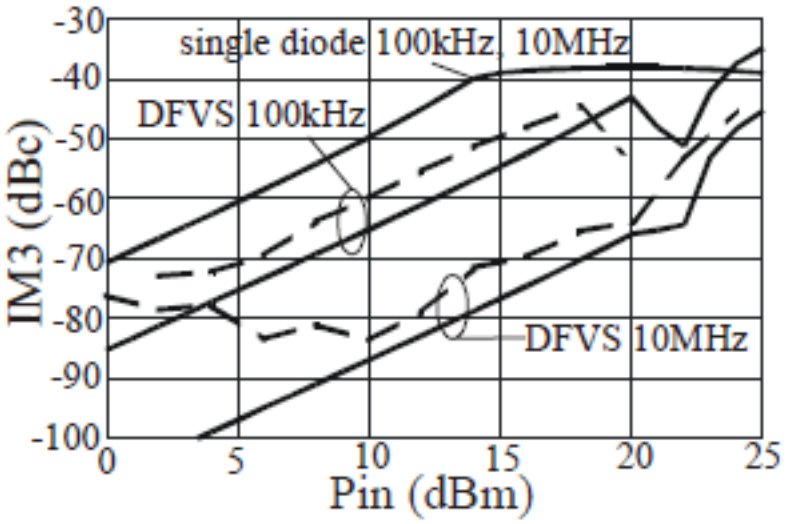

Figure 3.12: Measured and simulated IM3 components for a single varactor and a DFVS for $\Delta f = 100$ kHz and 10 MHz [13].

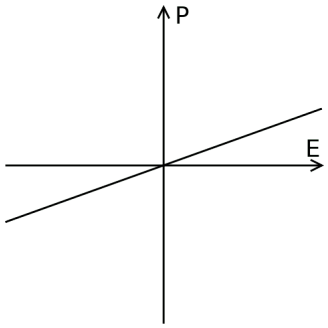

Figure 3.13: Change in dielectric polarisation in relation to an applied electric field.

3.1.3 BST Varactors

Diode varactors exploit a change in depletion layer width as a function of applied dc bias in order to provide capacitive tuning. Other methods for tuning capacitance exploit a change in material permittivity as a function of bias. A dielectric material is an insulator through which electric charges do not flow. Instead charges shift their average equilibrium positions causing dielectric polarisation to be observed. For a dielectric material induced polarisation has a linear correlation to the applied electric field as shown in Figure 3.13 where the gradient is the electric permittivity.

A ferroelectric material exhibits electric polarisation which, with the application of an external electric field of sufficient magnitude, can be reversed. Therefore the polarisation of a ferroelectric material is not just dependent on the immediate electric field, but also upon its history, yielding a hysteresis loop depicted in Figure 3.14.

Ferroelectric materials have a specific temperature, known as the Curie temperature, at which the type of polarisation exhibited shifts from being ferroelectric to paraelectric. These are known as the ferroelectric and paraelectric phases. Shown in Figure 3.15, paraelectric polarisation undergoes a nonlinear change in polarisation, however without

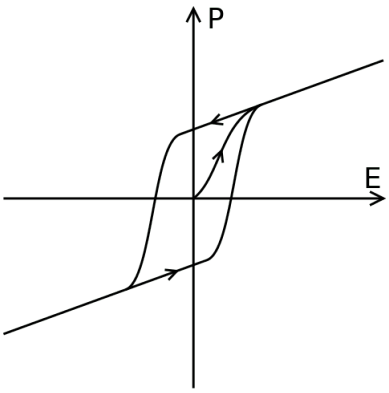

Figure 3.14: Change in ferroelectric polarisation in relation to an applied electric field.

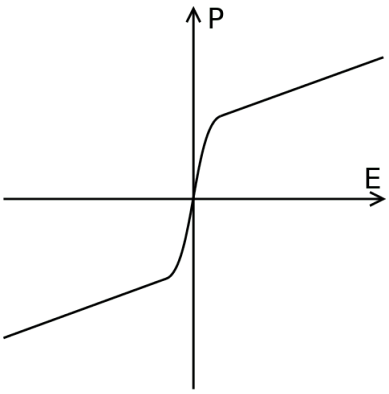

Figure 3.15: Change in paraelectric polarisation in relation to an applied electric field.

the effects of hysteresis seen in the ferroelectric phase.

The Curie temperature of *Barium Strontium Titanate* (BST) can be modified in such a way that it is in the paraelectric phase at room temperature. For this reason, BST could be a good candidate for use in the design of tunable circuitry [14]. As with varactor diodes, Q-factor and linearity are limiting factors in the application of BST based devices in tunable filters. The quality factor of a varactor diode deteriorates at higher frequencies since the Q of a p-n junction varactor is inversely proportional to frequency. BST varactors have an advantage in insertion loss over varactor diodes at frequencies approaching 10 GHz and above [15, 16]. By reducing the barium concentration, cryogenic BST filters with a much lower Curie temperature can be fabricated. These filters can have a lower insertion loss than their low temperature equivalents, however the available tuning range is reduced and a bulky cooling system is required for normal operation [17, 18].

Nath et al. [19] fabricate a tunable third-order combline bandpass filter using BST varactors over a large bias range (0-200 V). It is stated that the large bias helps to reduce intermodulation distortion generated in the filter due to the nonlinear change in capacitance with voltage at low bias levels. Additionally the large bias voltages have little impact on power consumption due to the low leakage current of BST capacitors. The total leakage current drawn by all three varactors (Table 3.1) at a bias of 175 V

was just 67.54 nA meaning that the power consumption of each varactor is about 4 µW under large bias. Incidentally this drops to below 0.6 µA per varactor for a smaller dc bias of 25 V.

Table 3.1: Leakage current versus bias voltage

Bias (V)	Current (nA)
25	22.68
75	48.87
125	66.20
175	67.54

Using a two-tone test, the IP3 power was measured to be +41 dBm, better than most varactor diodes, however the low Q of the varactors means that an insertion loss of no better than 3.1 dB is achieved across the tuning range. It is unclear as to what the bias conditions were for the IP3 measurement since it is not stated in the paper. One can assume however that +41 dBm is the best case scenario for this filter. Furthermore, after experimenting with different electrode thicknesses, it was deemed that the majority of the insertion loss is caused by losses in the electrodes and not the BST.

A paper by Yoon et al. [20] demonstrates how different architectures of BST varactor can be used to limit the intermodulation distortion generated, as well as reducing the bias voltage required. Five different techniques were investigated; wide and narrow gap capacitors (Figure 3.16), long and short attached-bias-electrode (ABE) and a long isolated-bias-electrode (IBE) (Figure 3.17).

The conventional narrow gap capacitor requires a smaller dc bias voltage than the wide gap capacitor since the permittivity of the BST is modified relative to the electric field present. The expense of a lower bias voltage means that the IMD generated is higher than in the wider gap equivalent since the RF signal and the DC bias signal are supplied to the same electrodes. Similarly the wide gap capacitor requires a larger bias voltage to achieve the same electric field across the gap and so is not as affected by IMD. The ABE and IBE architectures use high resistivity electrodes to isolate the bias from the RF signal allowing a wide RF gap to be maintained while the DC bias gap can be narrowed. This means that tunability can be increased without affecting the IMD.

Yoon reports IP3 measurements of 58 dBm for the long ABE architecture. The main drawback is that the Q-factors reported for the different structures are all lower than 30.

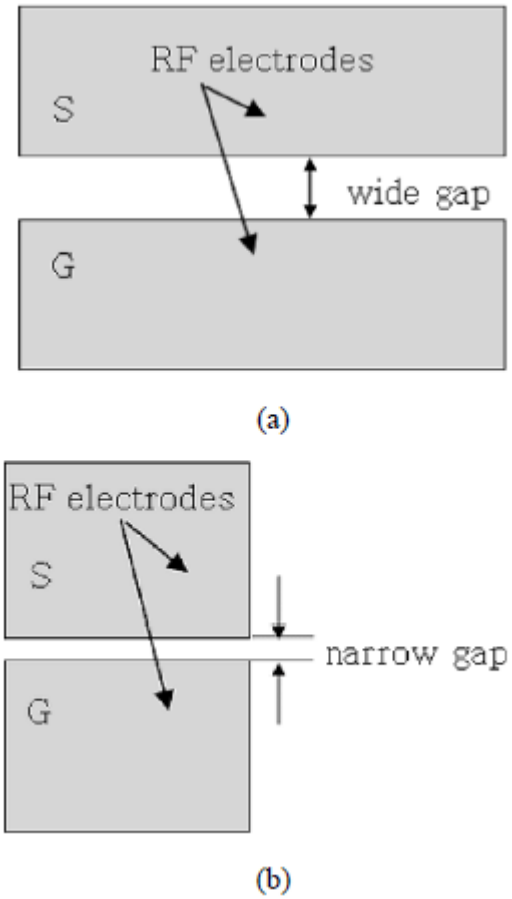

Figure 3.16: Conventional gap capacitors. (a) Wide gap capacitors. (b) Narrow gap capacitors [20].

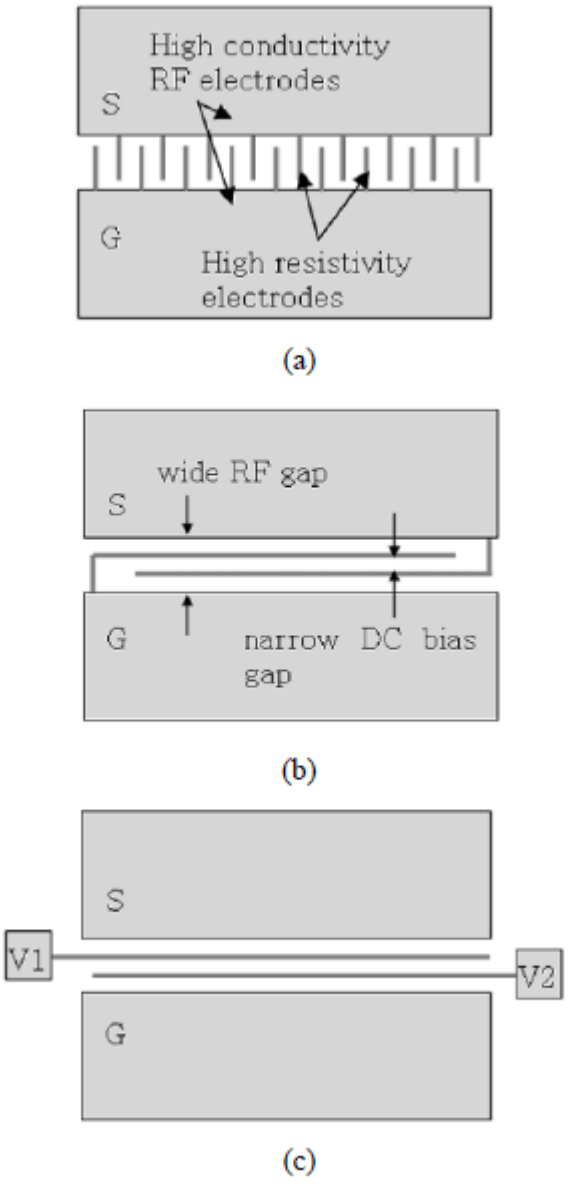

Figure 3.17: Gap capacitors with high-resistivity bias electrodes inside the gap. (a) Short ABE capacitor. (b) Long ABE capacitor (c) Long IBE capacitor [20].

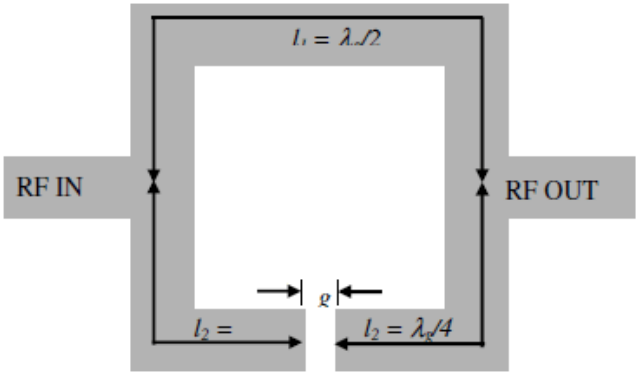

Figure 3.18: Schematic of UWB bandstop filter section [22].

3.1.4 PIN Diodes

A PIN diode is an un-doped intrinsic semiconductor sandwiched between a highly doped p-type semiconductor on one side, and a highly doped n-type semiconductor on the other. It is manufactured using epitaxial deposition. PIN diodes have a number of applications at high frequencies such as attenuators, photo-detectors or switches [21]. At low frequencies PIN diodes obey the standard diode equations. At high frequencies however, they act as near-linear resistors where the resistance is inversely proportional to the DC bias current through the diode. Under normal operation, the depletion region is contained entirely within the intrinsic semiconductor. Charge is stored in this region which discharges at a given rate. When the frequency of a signal sent to the diode is high enough that the intrinsic region cannot fully discharge, the junction acts as a resistive block. At lower frequencies, the junction acts as a small capacitor.

A considerable amount of research has been done regarding PIN diodes. Under reverse bias they can be used as photo-detectors [23]. When used as an RF switch however, PIN diodes can be used for electronically reconfigurable circuits where a diode can be used to switch in, or isolate sections of a circuit for a desired effect. There are many papers that have been written about the use of PIN diodes in reconfigurable antennas [24, 25, 26, 27].

Research has also been done using PIN diodes for reconfigurable filter designs. Karim et al. [22] present a filter that is reconfigurable between *ultra-wideband* (UWB) bandpass and bandstop states but also has the ability to switch the bandpass state to a *wireless local area network* (WLAN) band at 2.4 GHz using PIN diodes. The authors propose a bandstop filter using two, $\lambda/4$, open-ended stubs (l_2) with 90 ° bends separated by a gap, g and a $\lambda/2$ (l_1) connecting line with two 90° bends as shown in Figure 3.18.

In order to transform the response of the filter from bandstop to bandpass, two PIN diodes, D_1 and D_2, are placed at the ends of the $\lambda/4$ stubs to short them to ground (Figure 3.19). When D_1 and D_2 are in the ON state, the l_2 lines effectively become

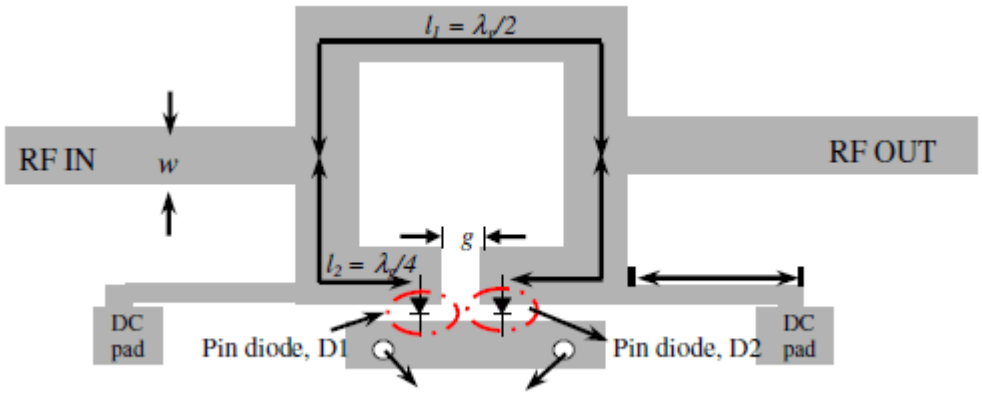

Figure 3.19: Schematic of UWB bandpass to bandstop reconfigurable filter [22].

short-circuited quarter-wave stubs and the network now acts as an UWB bandpass filter.

A second $\lambda/2$ section is connected to l_1 via another two PIN diodes, D_3 and D_4, as shown in Figure 3.20. When D_3 and D_4 are activated, the UWB bandpass filters response is switched down to a WLAN band with a bandwidth of 400 MHz.

The authors results show the filters in the three separate states (UWB-bandstop, UWB-bandpass and WLAN-bandpass) providing similar S-parameter measurements to their simulated tests.

With all diodes in the OFF state, the filter shows a bandstop response of 20 dB rejection with a 2.2 GHz bandwidth. When D_1 and D_2 are switched ON the filter gives a UWB bandpass response with a 3 dB bandwidth of 7 GHz and insertion loss of 2.1 dB. Finally, when all diodes are in the ON state the response centres on 2.4 GHz with a bandwidth of 400 MHz. The authors however do not provide any evidence of the filters ability to reject IMD. It can therefore be assumed that the filter presented in this paper may only be suitable for small signal levels and not those beyond the order of milliwatts.

In a 2012 paper from Brito-Brito et al. [28] a two-pole switchable bandpass filter is presented, with precise frequency and bandwidth switching between two states. The first state has a centre frequency of 1.955 GHz with a passband bandwidth of 140 MHz and the second, a centre frequency of 2.440 GHz with a bandwidth of 80 MHz. PIN diodes are used to switch in resonator extensions to control the centre frequency. Precise bandwidth control is achieved by managing the external-Q from the feed-lines and the coupling coefficient between the resonators respectively to determine the microstrip dimensions. The dimensions are then optimised using ADS/MOMENTUM in order to achieve the design specifications.

The filter was fabricated and tested for centre-frequency, bandwidth, power saturation and IP3. The results are shown in Figure 3.2. The filter exhibited behaviour very close to the specification. The variation in centre frequency to the simulations was within

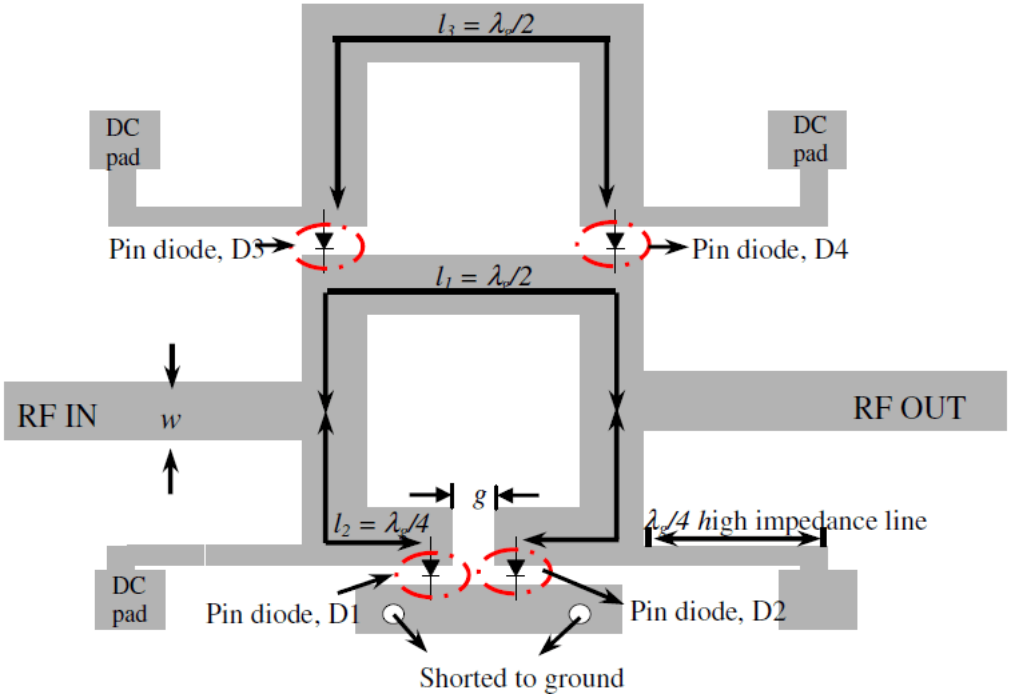

Figure 3.20: Schematic of reconfigurable (UWB bandstop-to-bandpass filter) and switchable (UWB to WLAN) filter [22].

1% for both states and the bandwidth variation was 9 MHz and 4 MHz for WiFi and UMTS respectively. The third-order intercept was measured to be 32.5 dBm for WiFi and 32 dBm for UMTS.

Table 3.2: Simulated and measured results of the WiFi and UMTS transmit standards [28].

	Centre frequency		Bandwidth		Power saturation point		IIP3	
	WiFi, GHz	UMTS, GHz	WiFi, MHz	UMTS, MHz	WiFi, dBm	UMTS, dBm	WiFi, dBm	UMTS, dBm
simulated	2.440	1.955	80	140	—	—	—	—
measured	2.428	1.939	71	144	16	19	32.5	32

Lugo and Papapolymerou [29] present a filter that exploits the direct effect inter-resonator coupling has on the bandwidth of a filter. They design a two-pole bandpass that uses PIN diodes to switch the bandwidth between two different states while maintaining a constant centre-frequency. Weak coupling between resonators produces narrow bandwidths while strong coupling produces wider bandwidths. This effect can be exploited by adding tuning stubs above and below the resonator ends in order produce the desired passband ratio by varying the coupling strength.

The filter, shown in Figure 3.21, requires eight PIN diodes to achieve the required coupling. When the inner four diodes are activated strong coupling between the resonators is attained, resulting in a wider bandwidth. For the narrowband state to be triggered, the inner diodes are deactivated, providing weaker inter-resonator coupling. However, this also reduces the effective length of the resonators. Therefore the outer

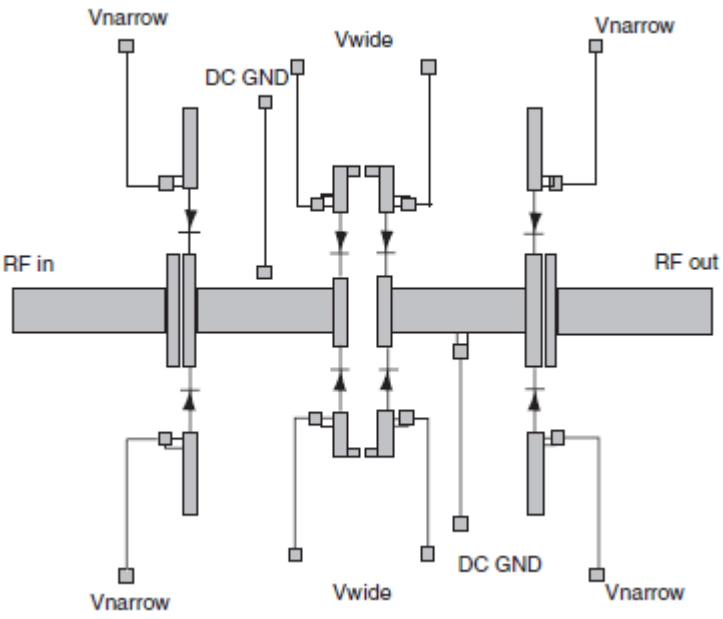

Figure 3.21: Bandwidth switching filter with bias lines [29].

stubs are introduced by switching the remaining diodes on in order to maintain the resonator length and keep the centre-frequency constant.

Measurements were taken to compare the physical filter with the simulated responses, which showed the filter performing much as the authors simulations had expected. There was a slight discrepancy found in the centre frequency which had shifted down from the predicted 5.8 GHz to 5.6 GHz in both states.

This was attributed to the geometric length of the diode leads as well as the conductive epoxy used in connecting them to the filter. which were previously unaccounted for The average additional length per diode was calculated to be 635 µm The authors remodelled their simulations to account for this additional length, resulting in the comparison measurements shown in Figure 3.22. The fractional bandwidths produced by the wideband and narrowband states were 10.12% with an insertion loss of 3.95 dB and 5.43% with an insertion loss of 4.73 dB respectively.

IMD was also investigated in the filter. The intermodulation power was measured for three different input power levels. The IP3 points were calculated by extrapolating these values using tone separations of Δf = 50, 100, 200, 400, 600 and 1000 kHz around the centre-frequency of the filter, f_c = 5.6 GHz shown in Figure 3.23. IP3 measurements for $\Delta f = 1$ MHz and $\Delta f = 50$ kHz were given as 43 dBm and 25 dBm respectively.

In conclusion, based on the literature, PIN diodes can be used as a means of switching between discrete states in a system designed for very low RF signals and severely limited by cost. However for applications where extremely low intermodulation distortion levels and very high-Q constraints are in place, such as the front-end of a cellular basestation, PIN diodes would not be suitable. Therefore other means of achieving

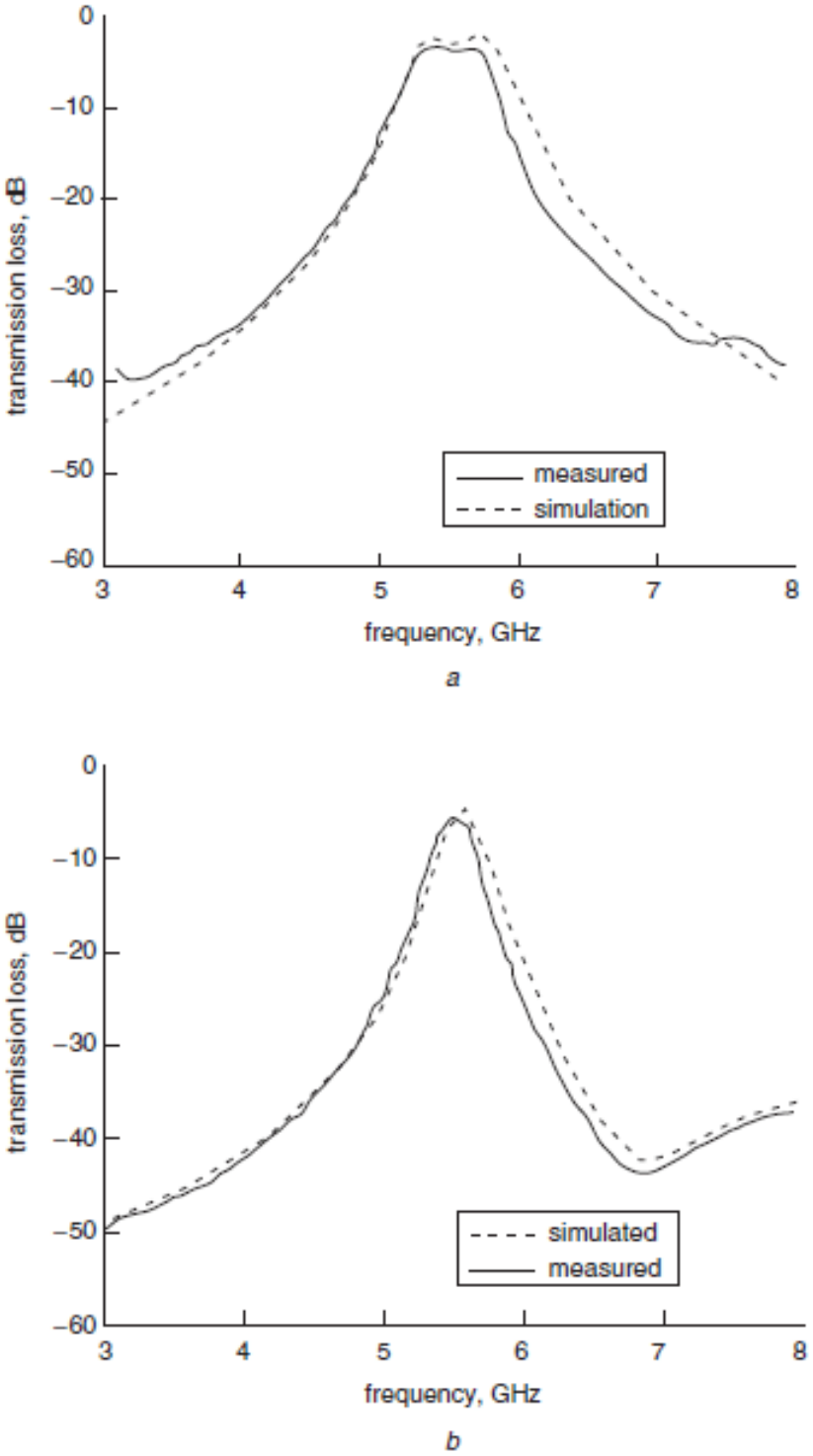

Figure 3.22: Measured and simulated transmission loss for bandwidth switching filter a) Wideband configuration b) Narrowband configuration [29].

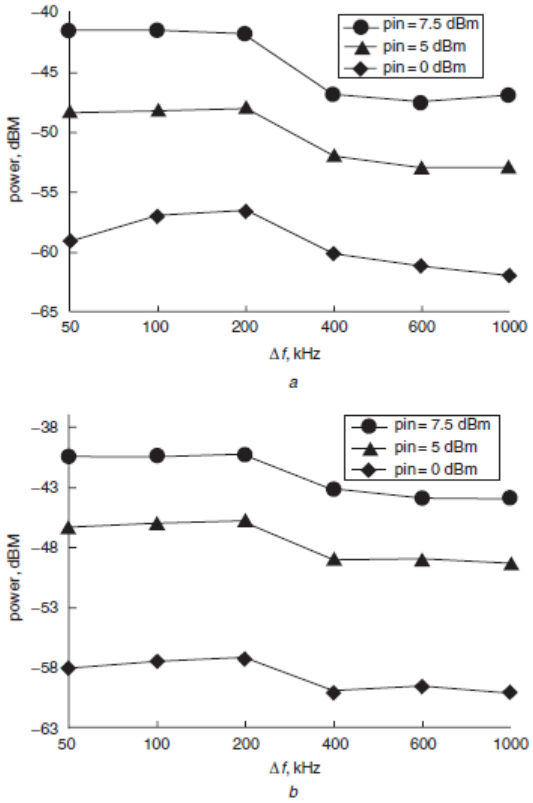

Figure 3.23: Intermodulation power against separation frequency, Δf [29].

high-linearity and low-loss should be sought.

3.1.5 Microelectromechanical Systems (MEMS)

As yet no devices have been covered that can provide tunability within the desired specifications. YIG filters have shown the ability to retain high Q-factors with tunability. On the down side however, they are sensitive to temperature, require large amounts of power (up to 5 W) and are physically vary large. Varactor diodes cannot handle high power signals and generate too much distortion. Similarly BST based varactors cannot handle high power signals and they suffer from low-Q. PIN diodes are better suited for higher power signals, however they have an effective series resistance in the order of 1 Ω which leads to Q-factors too small for practical applications. Therefore, what constitutes a good tuning element? There are a number of key features with which a tuning device must comply with in order to be considered. They must have very low series resistance (in turn leading to a high-Q factor), negligible power consumption, ability to handle large signals, very high linearity, fast switching speeds (μs/GHz) and they must be insensitive to temperature.

One such technology has been researched extensively in recent years for all of these properties and shows promising results. *Radio frequency* (RF) *microelectromechanical systems* (MEMS) devices have been developed for low-loss, tunable applications [30].

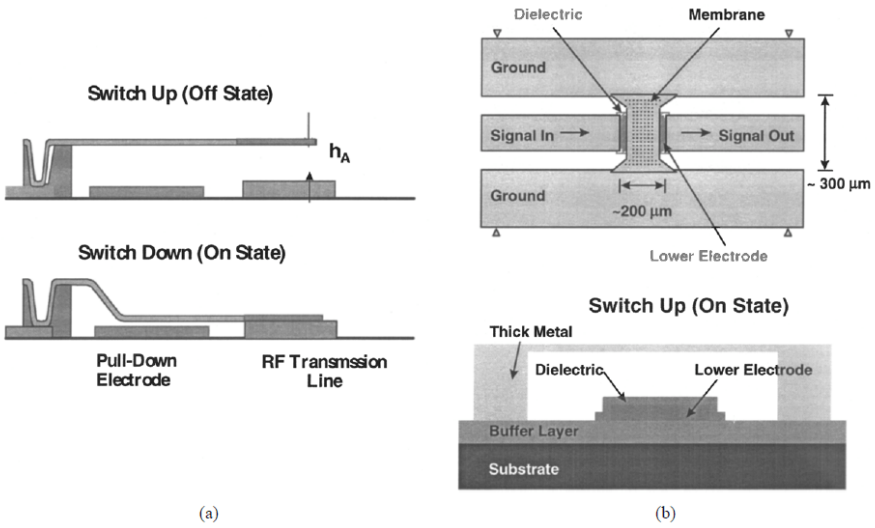

Figure 3.24: RF MEMS switches. (a) Cantilever type metal-to-metal contact switch. (b) Capacitive switch [31].

MEMS devices used for tuning purposes come in two separate varieties. Switches, designed for creating direct open- or short-circuit contacts in RF transmission lines; and analogue varactors, which are able to continuously tune between capacitance values.

RF MEMS switches are designed to operate at RF to millimetre wave frequencies of 0.1-100 GHz. They are grouped into two different types *Metal-to-metal contact switches* (Figure 3.24a) which use actuated cantilevers to form a direct connection between electrodes [31]; and *Capacitive switches* (Figure 3.24b) where high and low capacitance states are used to achieve RF switching [32]. The mechanical movement needed to achieve the required switching is provided by electrostatic forces generated via a high voltage bias.

RF MEMS switches have many advantages over semiconductor-switches such as PIN diodes and FET switches. Some of these are listed below [33]:

- *Near-zero power consumption*: Despite needing voltages of up to 80 V in order to induce electrostatic actuation, very little current is consumed. The energy required for a switching cycle is to the order of 0.1 µJ.
- *Very high isolation*: MEMS switches are designed with air gaps and have very small effective areas, resulting in very low off-state capacitances and therefore superb isolation.
- *Low insertion loss*: Series and shunt RF MEMS switches have been seen to have insertion losses of -0.1 dB at RF frequencies.
- *Intermodulation distortion products*: Compared to semiconductor switches, RF MEMs switches can have up to 30 dB better performance in terms of intermodulation products generated, showing them to be highly linear.

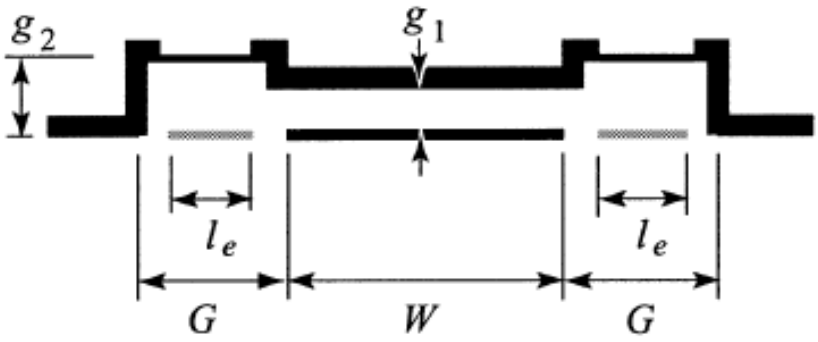

Figure 3.25: Bridge capacitor profile [34].

There are however some drawbacks to using MEMS switches which cannot be ignored:

- *Power handling*: Due to their inherently small size, power-handling is an issue with MEMS devices. Few devices can handle signal power levels larger than 0.1 W with any reliability.
- *Relatively low switching speed*: RF MEMS switches suffer from contact bounce upon switching which in effect reduces the speeds at which they can switch state. Typically semiconductor devices can do this in the order of nanoseconds, whereas MEMS devices have microsecond switching speeds.
- *High driving voltage*: As mentioned previously, electrostatic switches require actuation voltages of up to 80 V for reliable operation. Therefore voltage up-converter chips are often needed to be produced alongside the switches.
- *Packaging*: MEMS switches require hermetic seals which drive up the production costs.
- *Cost*: Despite the switches themselves being relatively cheap to manufacture on a large scale, the impact of requiring voltage driving chips as well as hermetically sealed packaging drives up the production costs, making it harder for MEMS switches to compete with semiconductors for price.

Abbaspour-Tamijani, Dussopt and Rebeiz [34] investigated the application MEMS bridge capacitors as the integrated tuning elements of a 3-pole tunable bandpass filter at 18-22 GHz. The filter used coplanar waveguide (CPW) transmission lines on a glass substrate. The MEMS bridge capacitors are similar in concept to those of Figure 3.24b, and are shown in Figure 3.25.

Capacitance is controlled by a dc voltage of between 0-80 V which affects the height, g_1, therefore enabling the capacitance of the device to be tunable. The filter was able to achieve a fractional bandwidth of $7.5 \pm 0.1\%$ across a tuning range of 7% from 18.6 GHz at 80 V to 21.44 GHz at 0 V. Figure 3.26 shows the response of the filter for the bands at either end of the tuning range. The midband insertion loss is around 4 dB across the tuning range. The glass substrate is believed to be a cause of some of the

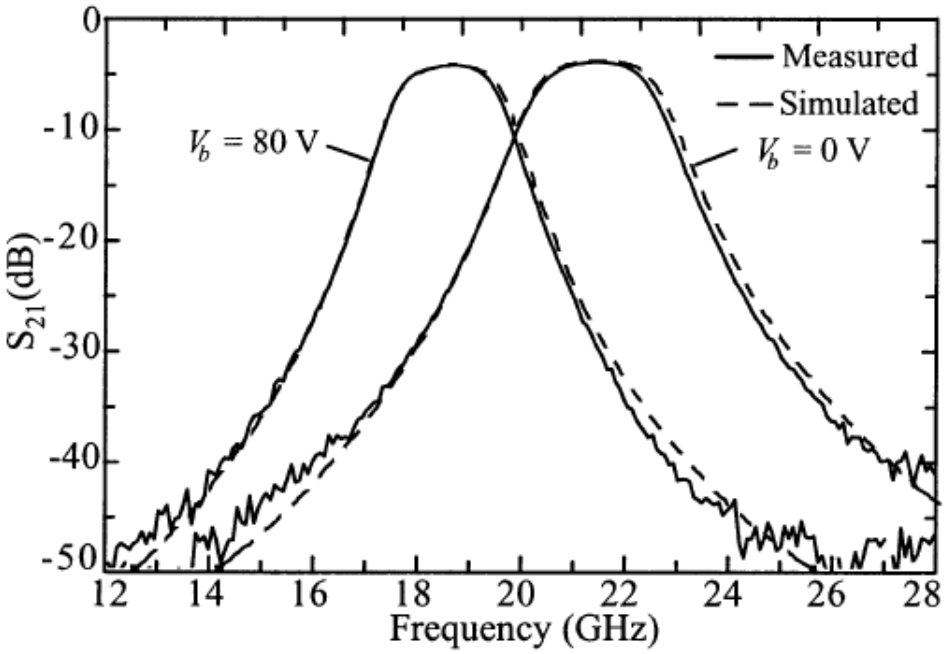

Figure 3.26: Three-pole MEMS tunable filter response [34].

insertion loss, and therefore could be reduced by replacing it with a quartz substrate instead. It should be noted that the MEMS devices were reported to have a Q greater than 350.

A two-tone characterisation test was performed on the filter. It was noted that third order intermodulation arises due to the force component of the beat frequency, $\Delta f = f_2 - f_1$, between the tones modifying the capacitance. The worst intermodulation performance was observed where the beat frequency was close to the natural frequency of the bridge. The third-order intercept points were measured as 32 dBm for $\Delta f =$ 50 kHz — close to the natural frequency of the bridge. This however rises to $>$ 50 dBm for $\Delta f >$ 150 kHz (Figure 3.27).

In terms of Q, the losses in this filter are dominated by the ohmic and dielectric losses of the CPW structure, showing that the MEMS bridge capacitor only has a minor impact on the insertion loss. However the natural resonant frequency of the MEMS structure increases the amount of intermodulation distortion present in the filter.

Lee and Kim [35] design a two tunable parallel plate MEMS capacitors, not using a bridge structure, but a piezoelectrically actuated cantilever structure illustrated in Figure 3.28. The first design is a simple structure where the cantilever beam is released by micromachining techniques using xenon-difluoride (XeF_2). A voltage is applied across the two Al electrodes causes a contraction (or expansion) in the ZnO film. This deflects the beam and subsequently narrows (or widens) the capacitor gap, increasing (or decreasing) the capacitance. The second design, Figure 3.28(b), works using a similar principle. It differs by its implementation of a thick silicon mass structure to form an air gap, and is driven by a rectangular thin beam (25 µm) composed of

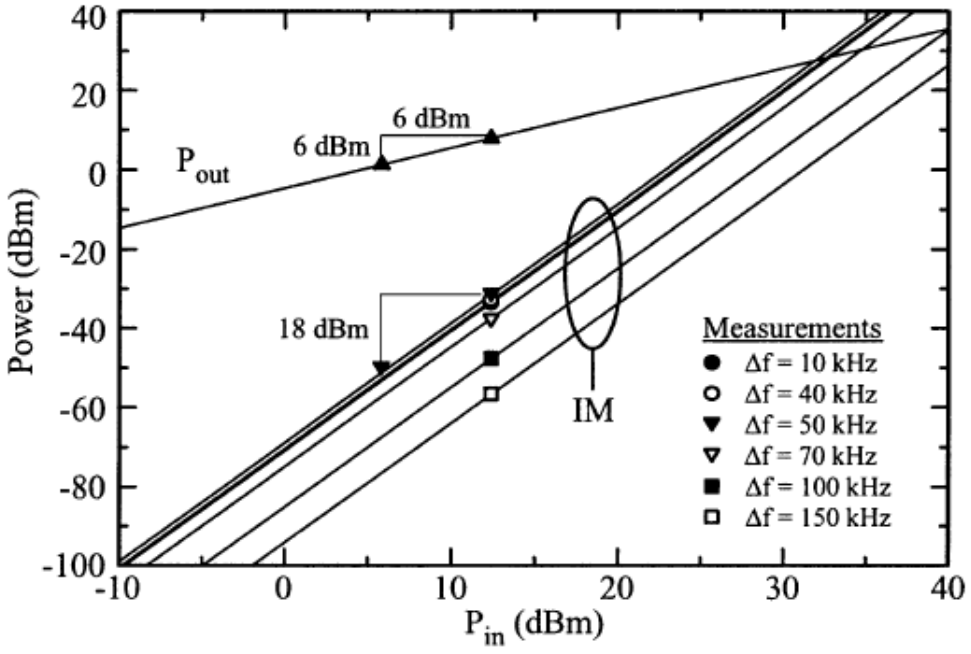

Figure 3.27: Third-order intermodulation product measured at $V_b = 0$ V [34].

Al-SiN-ZnO-Al-Si-Al layers. Additionally, since the *ZnO* film is above the neutral plane of the structure, a downward deflection will be seen with an increase in applied voltage.

The capacitors were both measured using a laser vibrometer to accurately determine the plate deflection position, and their capacitance recorded. The tests were performed using three different pulse shapes (sinusoidal, square and triangular) at 500 Hz. Each test showed that the deflection position corresponded to the signals shape and frequency, although the deflections were smaller than predicted. This could have been to do with the curvature of the structure in the, low capacitance states. The displacement of the capacitor top electrode against applied voltage measurements for both the micro-machined and bulk capacitors are shown in Figures 3.29 and 3.30 respectively.

Clearly the displacement of the bulk capacitor seems to show linearity and is reported to have a constant change in displacement of 0.086 $\mu m\,V^{-1}$, however, due to the curvature of the structure, this does not correspond to a linear change in capacitance. The authors claim a capacitor with a 21:1 tuning ratio, which is shown in Figure 3.31, however the linear region of this curve could reduce the usable tuning ratio down to about 1.5:1.

No two-tone characterisation tests were carried out on these devices and so it would be difficult, with the information contained, to determine if this type of tunable capacitance would meet the desired intermodulation requirements that this project demands.

A study of the intermodulation performance of RF MEMS variable capacitors was

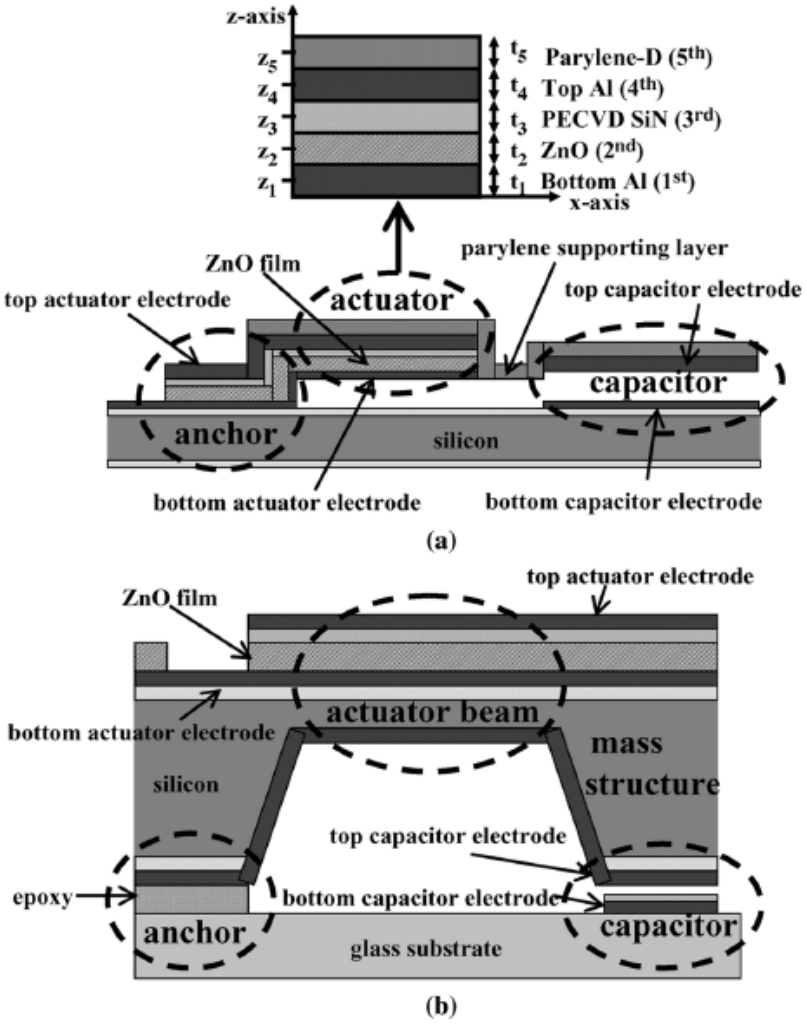

Figure 3.28: Schematic representation of the (a) surface micromachined and (b) bulk micromachined piezoelectric tunable capacitor [35].

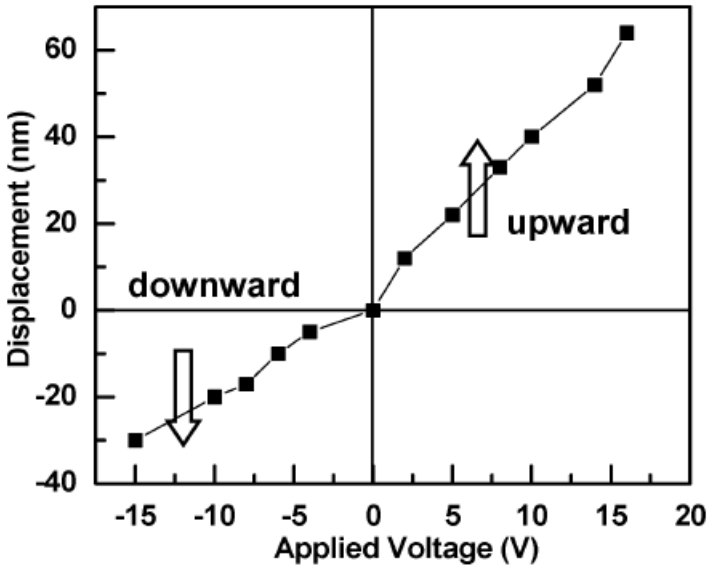

Figure 3.29: Measured piezoelectric displacement versus actuation voltage for the cantilever type tunable capacitor [35].

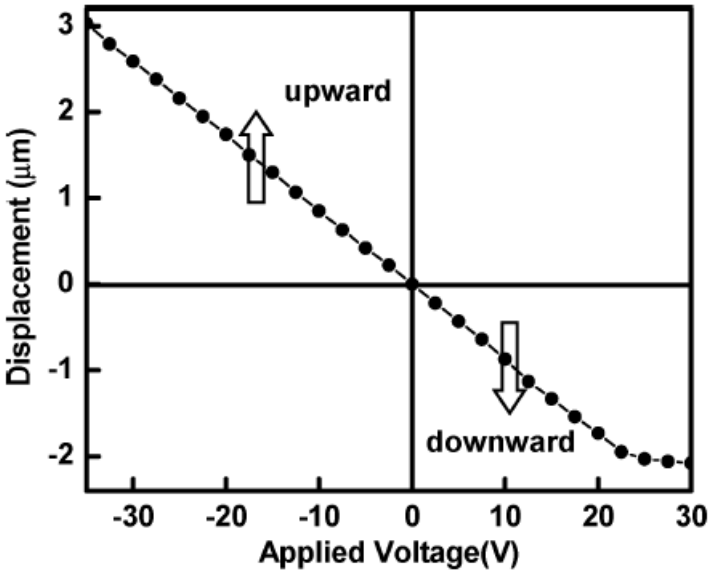

Figure 3.30: Measured piezoelectric displacement versus actuation voltage for the bulk micro-machined tunable capacitor [35].

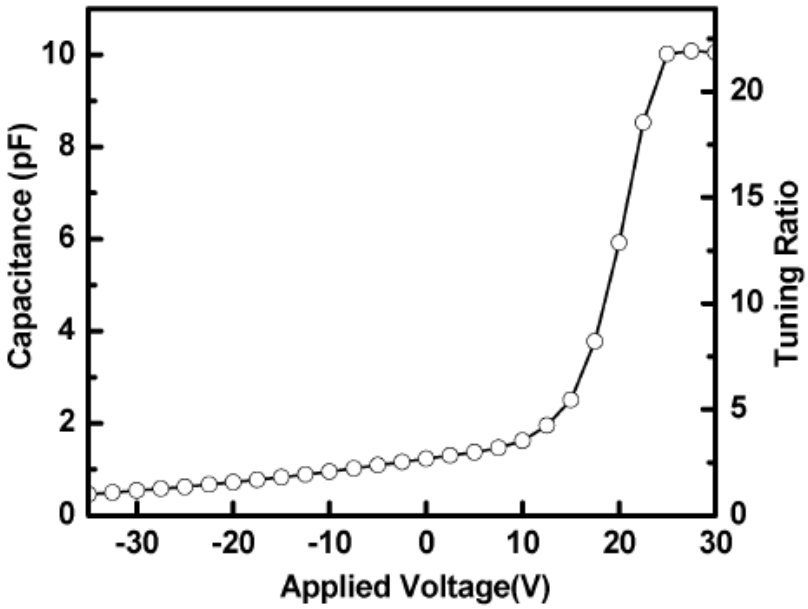

Figure 3.31: Capacitance and tuning ratio versus actuation voltage [35].

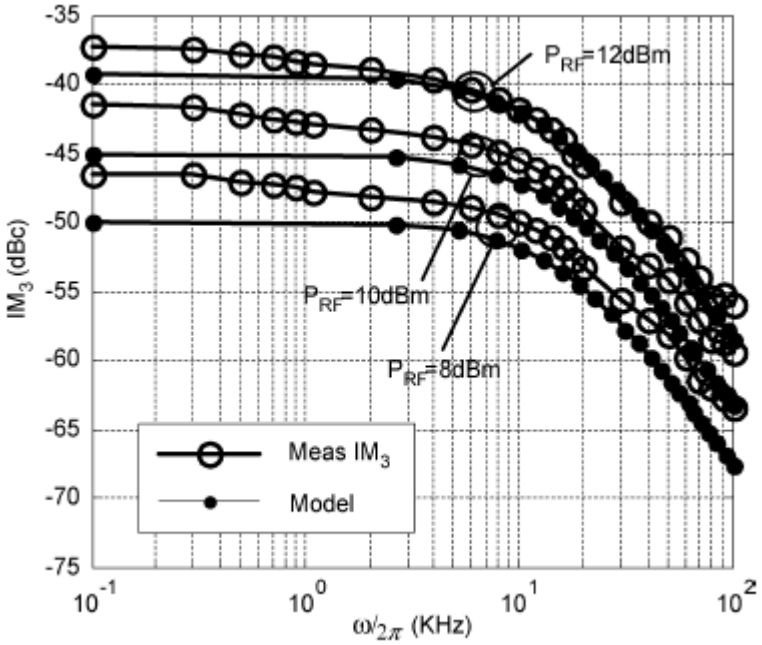

Figure 3.32: Comparison between the analytical model and measurements for RF powers of 8, 10 and 12 dBm in terms of IMD [36].

performed by Girbau et al. [36]. The authors propose a method for predicting the intermodulation performance of MEMS capacitors and compare their model with the measurements of an actual device. They analyse the displacement of parallel plates with tunable electrostatic actuation in the presence of two RF tones and a DC bias signal. It is shown that the displacement is controlled by the DC bias but produces displacement harmonics which in turn produce intermodulation products, illustrated in Table 3.3. The authors also show that there is a reduction in intermodulation products at frequencies higher than that of the mechanical resonant frequency, ω_0, of the device.

Table 3.3: Frequency components in displacement and intermodulation products

ω	Displacement harmonics (spectrum)	IMD products generation
$\omega < \omega_o/3$	1^{st}, 2^{nd}, 3^{rd}	3^{rd}, 5^{th}, 7^{th}
$\omega_o/2 > \omega > \omega_o/3$	1^{st}, 2^{nd} 3^{rd} attenuated	3^{rd}, 5^{th}
$\omega_o > \omega > \omega_o/2$	1^{st} 2^{nd}, 3^{rd}, attenuated	3^{rd} 5^{th} attenuated
$\omega > \omega_o$	1^{st} attenuated	3^{rd} attenuated
$\omega >> \omega_o$	- -	- -

Figure 3.32 shows the performance of the predicted third order intermodulation com-

ponents for frequencies up to 100 kHz. Their predictions closely match the measured third-order intermodulation relative to the carrier. It can also be seen that the intermodulation levels decrease with frequency. It was concluded that MEMS capacitors are expected to produce significantly higher IMD levels than capacitive switches.

It has been shown from the literature that the intermodulation seen in RF MEMS devices is dependent on the natural frequency of the fabricated devices. It has been seen that the third-order intermodulation powers are reduced at higher frequencies. The frequency separation of tones in a characterisation test also affects the distortion produced. Beat frequencies of much larger than the natural frequency of the MEMS structures provide the best performance in terms of linearity. For example, IP3 measurements have been reported as high as +80 dBm for a beat frequency of $\Delta f = 5$ MHz [37]. In addition, it has also been shown that although RF MEMS devices offer many benefits over their semiconductor equivalents in terms of tunable capacitors and RF switches, chiefly MEMS devices are shown to be highly linear in comparison to semiconductor varactors and PIN diodes. In addition, they consume negligible amounts of power on their bias lines and typically report a far higher Q. However, due to their small size, it is difficult for MEMS devices to pass high power signals (> 1 W).

3.1.6 Electromagnetic Bandgap (EBG)

Electromagnetic bandgap (EBG) structures are can be categorised as metamaterials designed with periodically arranged dielectric or magnetic materials. The utilisation of EBG can provide the capability for an RF structure to inhibit signal propagation in certain frequency bands. Most planar EBG structures have been fabricated in microstrip technologies [38]. Examples of EBG in microstrip technology can be found in spurious suppression of bandpass filters [39, 40], radiation pattern optimisation of patch antennas [41], and suppression of phase noise in oscillators [42].

Due to their inherent ability to reject certain frequency bands, with respect to bandpass filtering applications EBG devices tend to be used for the suppression of spurious pass bands. Spurious bands are inherent to the frequency response at harmonics of the centre-frequency [43]. They are well suited to ultra-wideband (UWB) bandpass filtering applications, where a wide upper stop band is required to suppress harmonic responses [44, 45].

Systems utilising EBG have been used in tunable and reconfigurable filter applications, however the tunability does not come from the EGB integrated components themselves. Rather the tunability comes from other devices such as varactors [46], PIN diodes [47], and MEMS [48, 49] technologies. More recent research has looked at the advantages of using EBG in the design of compact, reconfigurable planar filters [50, 51].

To summarise, EBG integrated devices can prove useful for the suppression of spurious bands as well as provide the affordability of compactness in planar applications. EBG

alone cannot provide tunability or reconfigurability to a system. Other devices such as varactor and MEMS technologies need to be integrated with EBG materials in order for tunability to be realised. Therefore with the scope of this project in mind, EBG integration can be put to one side in the context of tunable filtering. It is however useful to note that should the need for the suppression of spurious bands arise during the course of this project, EBG is one potential method that can be implemented.

3.2 Nonlinear Distortion and its Characterisation

When data is transmitted through a medium to a receiver, ideally only the transmitted data will be seen at the receiver. However, in practice this is not the case. Signal perturbation is defined being any component, other than the intended transmission data, that is detected at the receiver. Signal perturbation causes difficulties in the correct decoding of the received data meaning that mitigation techniques must be employed in order to reconstruct the original data. Broadly speaking, there are two types of signal perturbation:

- The addition of new components to the signal, such as *additive random noise* components as well as any *additive deterministic interferences*. Sources of additive noise are largely unavoidable and can be either internal or external to the system. Additive interference components can be originated from any other communication channel occupying the same system, or by another system sharing the same medium.
- Any form of *signal distortion*. Contrary to noise and interference, which are additive, signal distortion is a modification of the signal which cannot be disassociated from it. In other words, it cannot be detected after the termination of signal transmission.

Additive noise and interference components cannot be avoided, but there are well established methods of mitigation which fall outside of the scope of this study, therefore they need not be explored in any more detail. Instead, focus should turn to signal distortion which will be covered in more detail.

Consider an amplitude and phase modulated (QAM) baseband signal, $x(t)$, given by:

$$x(t) = A(t)cos[\omega_c(t) + \theta(t)] \tag{3.8}$$

Where A is the signal amplitude, ω_c represents the angular frequency of the carrier signal and θ represents the phase shift.

The output of the system $y(t)$ can be assumed to be some nonlinear operation of

$x(t)$:

$$y_{NonLin}(t) = S_{NonLin}[x(t)] \tag{3.9}$$

Where S_{NonLin} is a nonlinear signal operator.

It follows that for the output of the system when truncated to the third degree:

$$y(t) = a_1 x(t-\tau_1) + a_2 x(t-\tau_2)^2 + a_3 x(t-\tau_3)^3 \tag{3.10}$$

The output can be assumed to be linear when $x(t) \gg x(t)^2, x(t)^3$, giving:

$$y_{Lin}(t) = a_1 A(t-\tau)\cos[\omega_c t + \theta(t-\tau_1) - \phi_1] \tag{3.11}$$

Where $\phi_1 = \omega_c \tau_1$.

$$\begin{aligned} y_{NonLin}(t) = {} & a_1 A(t-\tau_1)\cos[\omega_c t + \theta(t-\tau_1) - \phi_1] \\ & + a_2 A(t-\tau_2)^2 \cos^2[\omega_c t + \theta(t-\tau_1) - \phi_1] \\ & + a_3 A(t-\tau_3)^3 \cos^3[\omega_c t + \theta(t-\tau_1) - \phi_1] \end{aligned} \tag{3.12}$$

And using the following identities:

$$\cos(A)cos(B) \equiv \frac{1}{2}\cos(A-B) + \frac{1}{2}\cos(A+B) \tag{3.13}$$

$$\cos^2(A) \equiv \frac{1}{2} + \frac{1}{2}\cos(2A) \tag{3.14}$$

$$\cos^3(A) \equiv \frac{3}{4}\cos(A) + \frac{1}{4}\cos(A) \tag{3.15}$$

Gives:

$$\begin{aligned} y_{NonLin} = {} & a_1 A(t-\tau_1)cos[\omega_c t + \theta(t-\tau_1) - \phi_1] \\ & + \frac{1}{2}[a_2 A(t-\tau_2)^2 + a_2 A(t-\tau_2)^2 cos(2\omega_c t + 2\theta(t-\tau_2) - 2\phi_2) \\ & + \frac{1}{4}[3a_3 A(t-\tau_3)^3 cos(\omega_c t + \theta(t-\tau_3) - \phi_3) \\ & \qquad + a_3 A(t-\tau_3)^3 cos(3\omega_c t + 3\theta(t-\tau_3) - 3\phi_3)] \end{aligned} \tag{3.16}$$

It can be seen from equation 3.11 that $y_{Lin}(t)$ is a modulated version of $x(t)$ where only the signal's amplitude and phase have been modified, therefore the spectral information remains intact. Whereas for y_{NonLin} it is shown that many frequency terms other than those at the input have been generated. This is referred to as *spectral regrowth.*
Signal distortion falls into two discreet categories [52]:

- *Co-channel distortion*, where the distortion spectral lines fall exactly over the

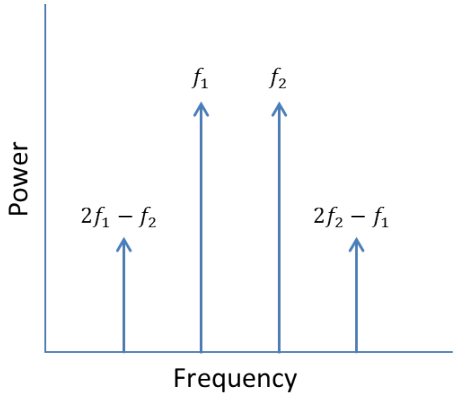

Figure 3.33: Intermodulation products generated by two fundamental tones, f_1 and f_2.

intended signal frequency, perturbing the desired channel.

- *Adjacent-channel distortion*, where the spectral lines lie around the original signal, perturbing the adjacent channel.

Intermodulation distortion (IMD) is a special case of nonlinear distortion. It is characterised by the appearance of spectral components in the output equal to the sums and differences of integer multiples of the two or more component frequencies. The order of an intermodulation product is determined by the sum of the absolute values of the coefficients. For a bandpass system, the odd-order intermodulation components pose a particular threat since they can often fall within the passband providing co-channel distortion.

Take for example a nonlinear system with two signals, $f_1 = 104$ MHz and $f_2 = 106$ MHz, at the input. Third-order intermodulation, $IM3$, products would fall at frequencies given by the following equations and illustrated in Figure 3.33:

$$IM3 = 2f_1 - f_2 \tag{3.17}$$

$$IM3 = 2f_2 - f_1 \tag{3.18}$$

Meaning that third order distortion products would be found at 102 MHz and 108 MHz. For a bandpass filter operating in the $100 - 110$ MHz band, these spectral components can become large enough to distort the information contained in the original signal potentially negating the benefit of including the filter in the first place. Incidentally, the fifth-order IM products would be found at 100 MHz ($3f_1 - 2f_2$) and 110 MHz ($3f_2 - 2f_1$). Typically though more power is found in the lower order products and therefore if the third-order IM products are deemed small enough to not disrupt the system, all other odd-order IM products can also be deemed negligible. To characterise a system in terms of its intermodulation performance, a two-tone characterisation test can be carried out. This is where a system input is driven by a two-tone sinusoid stimulus. A spectrum analyser is then used in order to measure the output signal spectrum for any

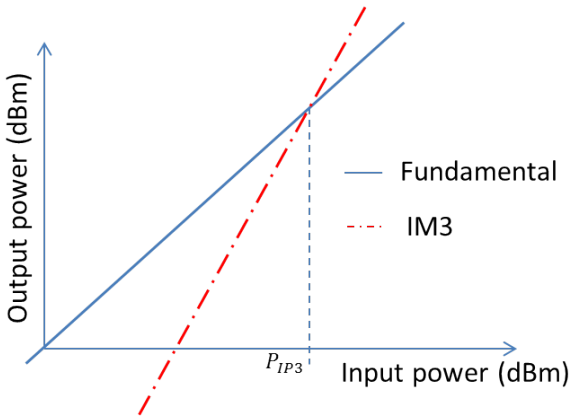

Figure 3.34: A linear extrapolation of the fundamental and third order intermodulation (IM3) used in finding the third-order intercept point (IP3).

generation of frequency components outside of the fundamental frequencies.

When the output power of the fundamental and IM3 components is plotted on a logarithmic scale against the input power for two equal power sinusoids at small power levels (within the linear region of a system), it can be observed that the fundamental power rises at a rate of 1 dB/dB and the IM3 products by 3 dB/dB. Although at larger power levels, the fundamental and IMD components compress and tend toward constants, the linear regions of each can be extrapolated to a fictitious intersection point, known as the *third-order intercept point* (IP3), shown in Figure 3.34. This fictitious point can be used to estimate the power levels of IM3 components for a given input power.
Assuming a lossless System at the fundamental frequency:

$$P_{out} = P_{in} \tag{3.19}$$

Expressing the input and output power levels are in logarithmic format (dB) ensures that third-order products in the output increase at triple the rate of the input power, due to their cubic nature. The third-order intermodulation power is given by the following formula:

$$P_{IM3} = 3P_{in} - P_0 \tag{3.20}$$

Where P_0 is the output power when the input is 0 dB.
The third-order intercept point (P_{IP3}) is the input power at which P_{out} and P_{IM3} are equal, therefore:

$$P_{IP3} = P_{in} = P_0/2 \tag{3.21}$$

Rearranging equation 3.21 and substituting back into 3.20 provides a method of estimating the intermodulation power levels:

$$P_{IM3} = 3P_{in} - 2P_{IP3} \tag{3.22}$$

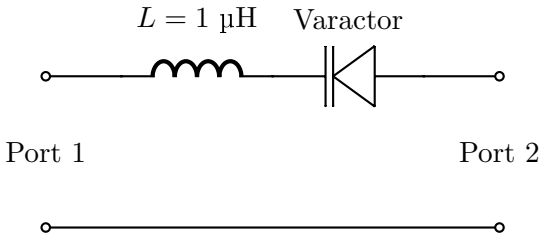

Figure 3.35: Schematic of a series LC resonant circuit with a lumped inductor and a varactor diode.

Rearranging for P_{IP3} gives:

$$P_{IP3} = \frac{3P_{in} - P_{IM3}}{2} \tag{3.23}$$

It is generally assumed that intermodulation products should be suppressed to less than 0.1 % of the smallest information signal power required in the system. From this, an estimation can be made about the required P_{IP3} point of an electronically tunable filter in a base station diplexer. For the purposes of this work, it will be assumed that the signal power in receiver circuitry is typically around -30 dBm. In this case, intermodulation products would need to be kept below -60 dBm to avoid distorting the signal. Additionally, the maximum input power is given by the power of a transmitted signal, typically of the range 40 dBm.
Substituting these values into equation 3.23 gives an estimate of the minimum required IP3 point: $P_{IP3} \geq 90$ dBm. This value will be used as a benchmark throughout the project to determine whether a device is acceptable for use in a front-end filter.

3.3 Reconfigurable Filter Design

3.3.1 Varactor Diode Experiments

Varactor diodes are semiconductor devices which exhibit a capacitance as a function of reverse-bias voltage. It was shown in the literature review that a varactor diode can be used to electronically tune a filter by exploiting the change in capacitance in order to alter the frequency response of a filter. The distortion generated by the device however, proves to be the downside of varactor diodes. Most varactors provide signal-perturbing intermodulation products at relatively low signal powers. In order to show this to be true, simulation software will be used to perform a two-tone characterisation test on a two-pole, varactor-tuned bandpass filter using harmonic balance. The filter was designed using lossless lumped elements from the specifications laid out in chapter 4.5 of [4] for a capacitively-coupled Chebyshev bandpass filter.

The simulation uses a model of the Motorola MV 1404 silicon tuning diode [53] in Agilent ADS which is able to tune between about 1 nF and 50 pF for reverse bias

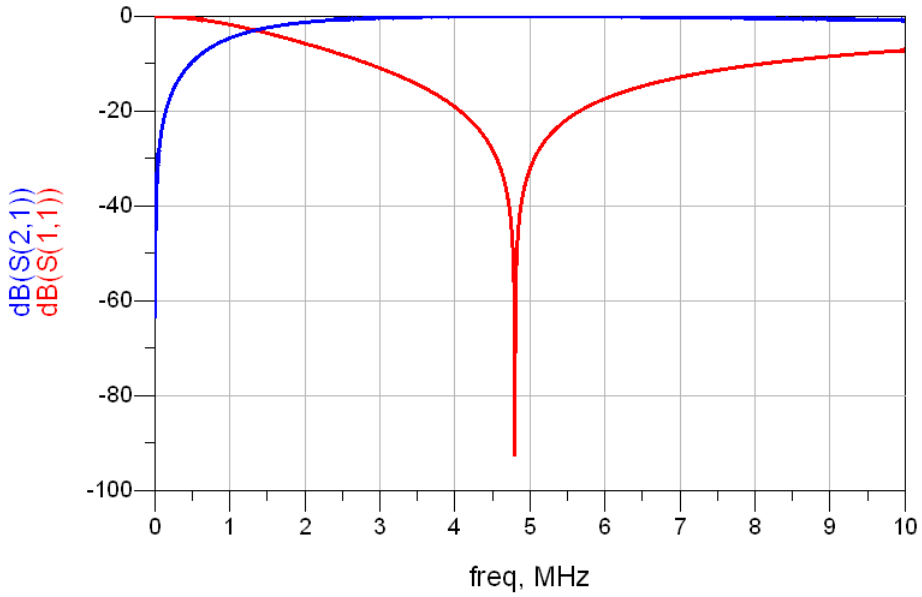

Figure 3.36: S-parameter measurements to determine the resonant frequency of the circuit.

voltages of 0 volt to 5 volt respectively.

The zero-bias capacitance of the varactor was measured by forming an LC resonant circuit with a series inductor (Figure 3.35) and measuring the frequency as which resonance occurs, which is given by the formula:

$$f_r = \frac{1}{2\pi\sqrt{LC}} \tag{3.24}$$

When rearranged to find the capacitance gives:

$$C = \frac{1}{L(2\pi f_r)^2} \tag{3.25}$$

Therefore the capacitance can be calculated by measuring the resonant frequency of the circuit, given by a zero in S_{11} (as shown in Figure 3.36). It can be seen that the circuit resonates at about 4.8 MHz, therefore substituting this into equation 3.25 and knowing that $L = 1$ µH we get a capacitance of 1.1 nF.

A Chebyshev bandpass filter was designed on the assumption that the capacitance of the shunt LC resonators is 1.1 nF with the schematic shown in Figure 3.37.

The bias network includes a large series inductor and a shunt capacitor as an RF choke, effectively allowing the DC bias signal to be connected to the varactors while at the same time decoupling the RF signal from the bias line. The S-parameters of the filter for three bias conditions from $V_b = 0 - 2$ V, are given in Figures 3.38-3.40.

It can be seen that under no bias conditions the filter centres at about 3.1 MHz, with

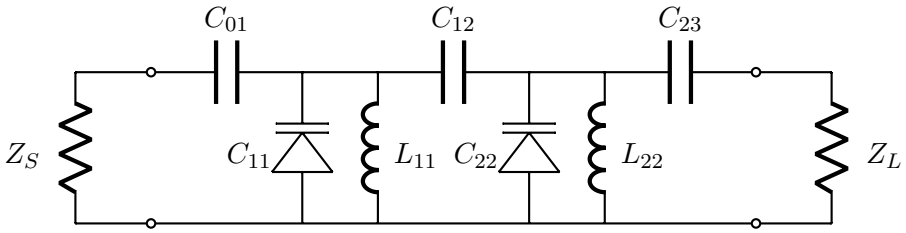

Figure 3.37: A schematic of the lumped element Chebyshev bandpass filter design using varactors for resonator tuning.

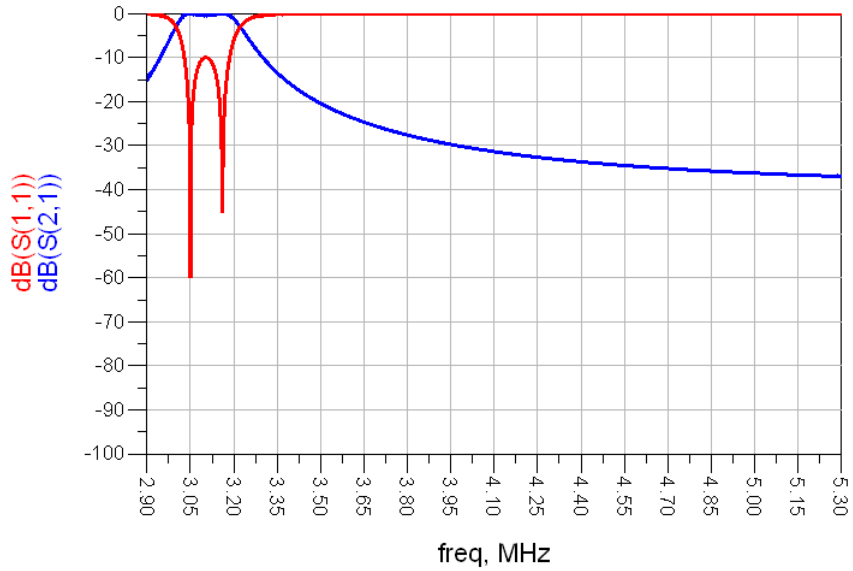

Figure 3.38: S-parameter response of a capacitively-coupled Chebyshev tunable filter using a varactor with bias condition $V_b = 0$ V.

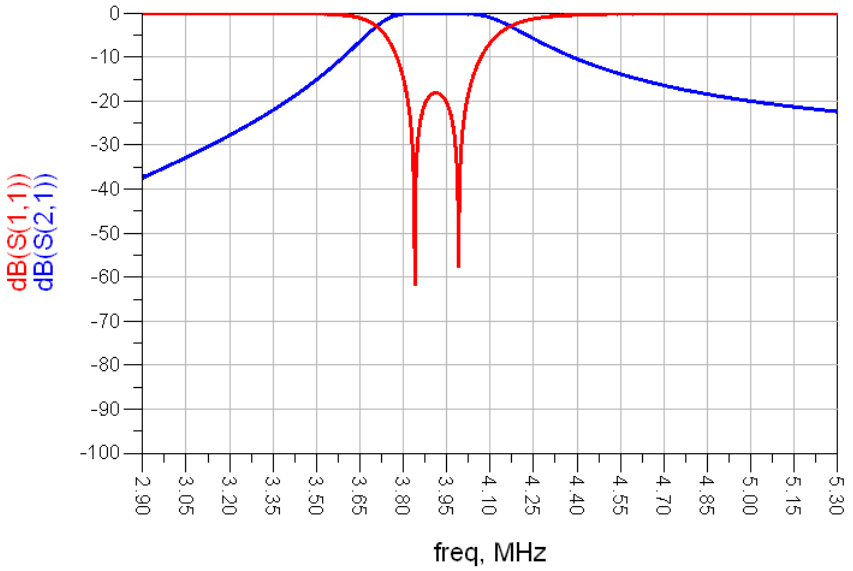

Figure 3.39: S-parameter response of a capacitively-coupled Chebyshev tunable filter using a varactor with bias condition $V_b = 1$ V.

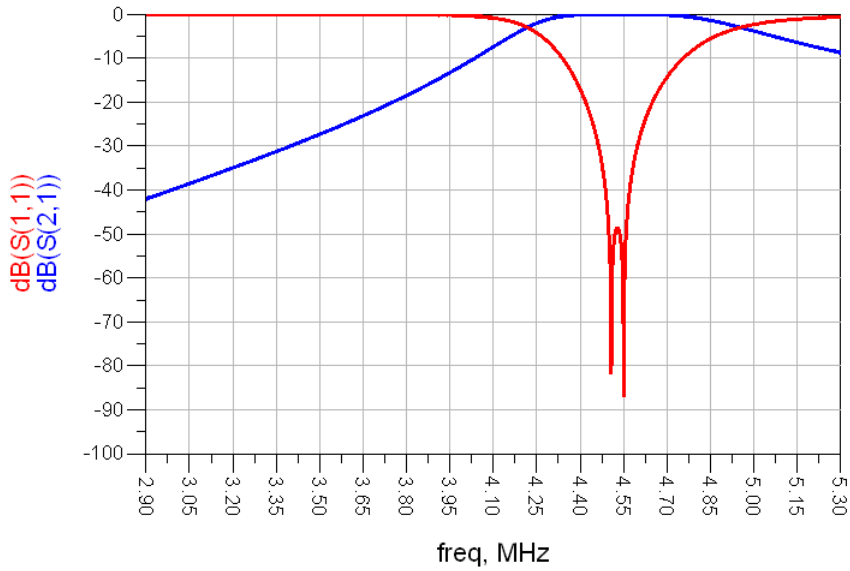

Figure 3.40: S-parameter response of a capacitively-coupled Chebyshev tunable filter using a varactor with bias condition $V_b = 2$ V.

a typical lossless two-pole response. As the reverse bias voltage is raised from 0 V to 2 V, the varactor capacitance is reduced and so the centre-frequency increases to 4.5 GHz at $V_b = 2$ volt. A side effect sees the bandwidth of the filter decreasing as the coupling becomes stronger. This shows the frequency dependent nature of inter-resonator couplings which will be looked at more closely in subsequent chapters.

Each bias state is shown to have a passband of low loss and therefore two-tone characterisation tests can be carried out in order to determine the amount of third-order intermodulation distortion generated by the varactors in the filter.

The passbands of each state were observed in order to determine the frequency of the tones to be used in the IM3 measurements. Tone spacings of 20 kHz were to be used with the lower frequency tone for each varactor state at 3.09, 3.89, and 4.52 MHz.

Plots of the IM3 measurements can be found in Figure 3.41. The input third-order intercept points (IP3) were measured to be -9 dBm, -3dBm , and 1 dBm for bias voltages of $V_b = 0$, 1, and 2 volt respectively.

These IP3 measurements fall far short of the specifications needed for a tunable front-end filter, however with hindsight, a few alterations to the testing procedure could yield larger third-order intercept measurements. For example, the varactor used in for testing was modelled on a hyper-abrupt junction diode which boasts a 10:1 tunability ratio. If a less abrupt junction varactor were to be used, the intermodulation products generated would be smaller at the expense of a lesser tuning range. Additionally, the tests performed here used small bias voltages this is the worst case scenario for a varactor in terms of IMD. If the filter were to be designed for tuning ranges where the bias-to-signal voltage ratio is large, the RF signal would have less impact on the

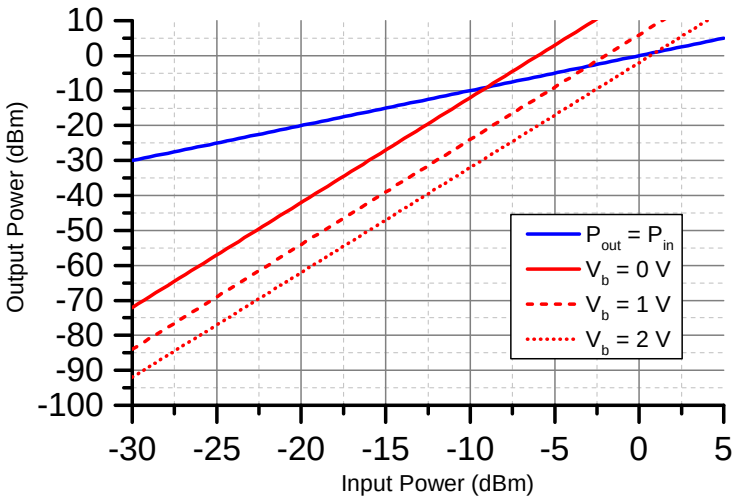

Figure 3.41: A plot of the simulated third-order intermodulation for a varactor.

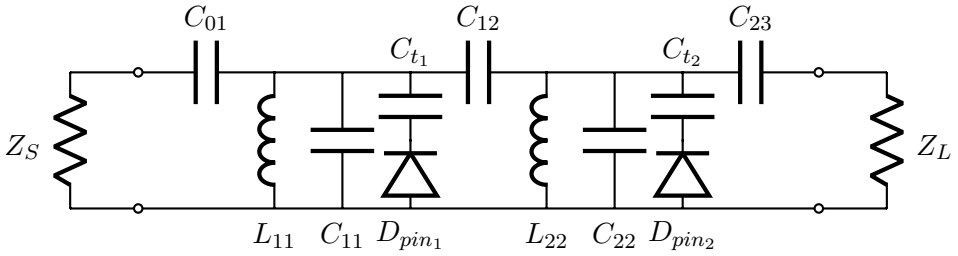

Figure 3.42: Schematic of a PIN diode tunable bandpass filter.

immediate capacitance of the varactor and as a result, the IMD products would be smaller. Looking at it in this way, it becomes obvious that a varactor is only in its linear range for very small input signals.

Despite a number of alterations that could be made to the design, altogether they would not have a remarkable impact on the third-order products generated as is backed up by the literature on varactor diodes. Therefore varactors do not warrant any further investigation in the context of this work.

3.3.2 PIN Diode Experiments

PIN diodes can be used in a variety of reconfigurable network applications, from reconfigurable antennas to bandpass-bandstop filter transformations. PIN diodes act as RF switches, meaning that sections of an RF circuit can be electronically switched in or blocked out at will. In the context of a microwave filter, a PIN diode (or indeed a network of PIN diodes) can be used to discretely modify a capacitance. The assumption is that a tuning capacitor in series with a PIN diode could be placed in parallel with the fixed capacitance of a shunt resonator allowing for an electronically controlled addition of capacitance. Figure 3.42 shows a schematic of a lumped element Chebyshev bandpass filter. The shunt resonators have parallel tuning capacitors, C_{t_1}

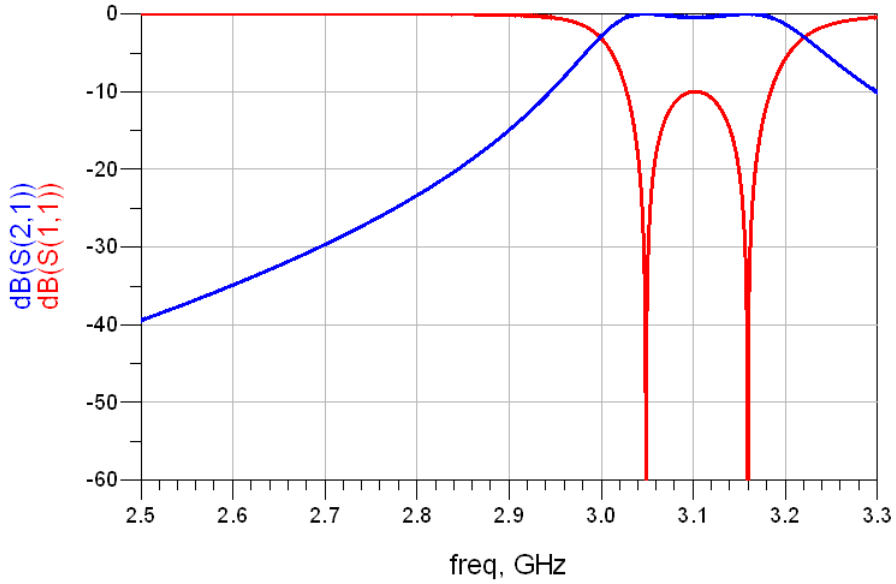

Figure 3.43: Simulated response of the filter in the OFF state.

and C_{t_2} which can be switched in or out using PIN diode (D_{pin_1} and D_{pin_2}). When the diodes are in their *OFF* state, they are effectively open switches and so the tuning capacitors would have no effect on the response of the filter. In the *ON* state however, the effective capacitance of the resonator would be increased, by the value of the tuning capacitor. The first resonator for example, would become a parallel combination of inductance L_{11} and capacitance $C_{11} + C_{t_1}$, causing the centre frequency to reduce. It is worth noting that the bias structure of the PIN diode relies on a current through the junction in order to be switched on. The *OFF* state is modelled by a voltage bias, since no current flows through the diode in its high resistivity state.

The response of the filter is shown in Figure 3.43 for the *OFF* state and Figure 3.44 for the *ON* state.

Simulations for intermodulation distortion characterisation were performed for both the voltage and current bias states. The plots shown in Figure 3.45 display the linear extrapolations of the fundamental, and third-order intermodulation components present at the output.

The third-order intercept point was seen to be 67 dBm for the *OFF* state and slightly under 110 dBm for the *ON* state. This is much higher than what was expected based on the literature. Therefore it was decided that a switchable filter using commercially available PIN diodes should be fabricated in order to check the simulation results.

3.3.3 Fabrication and Testing

A two-pole filter was designed for a combline structure so that the bandwidth is maintained as best as possible between states. In addition, the filter requires an RF choke

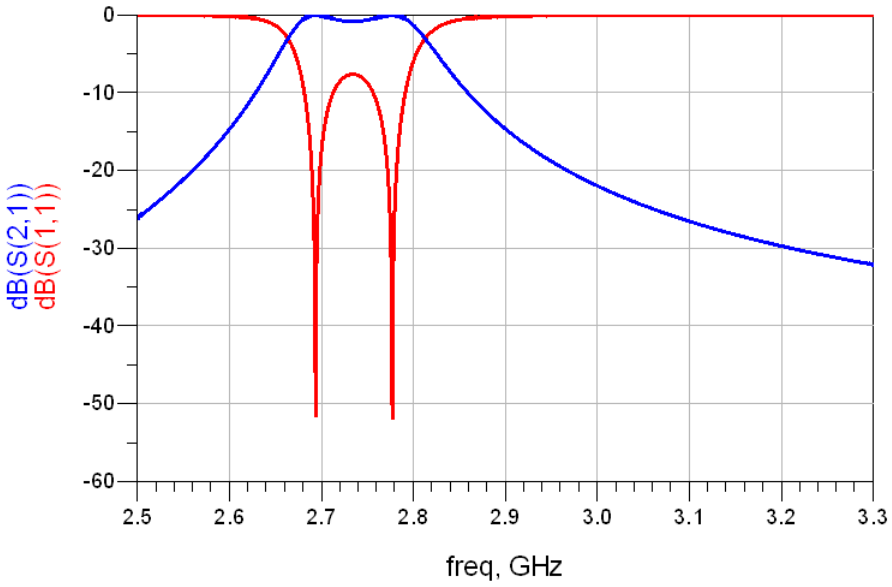

Figure 3.44: Simulated response of the filter in the ON state.

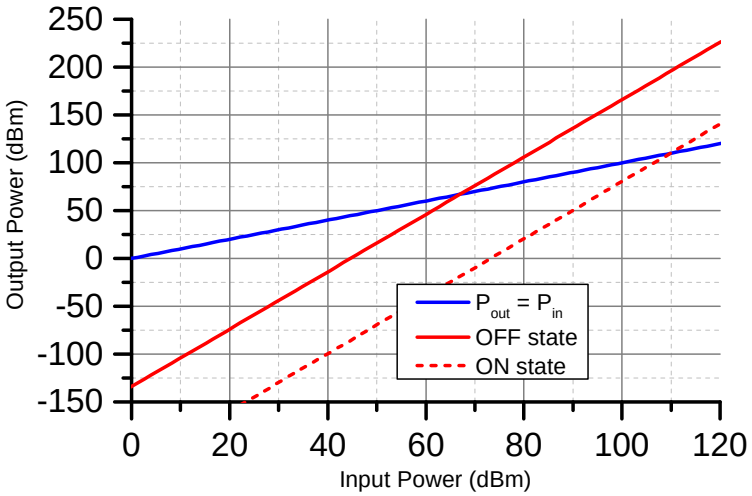

Figure 3.45: Third-order intercept point of the PIN diode circuit simulation in the OFF state.

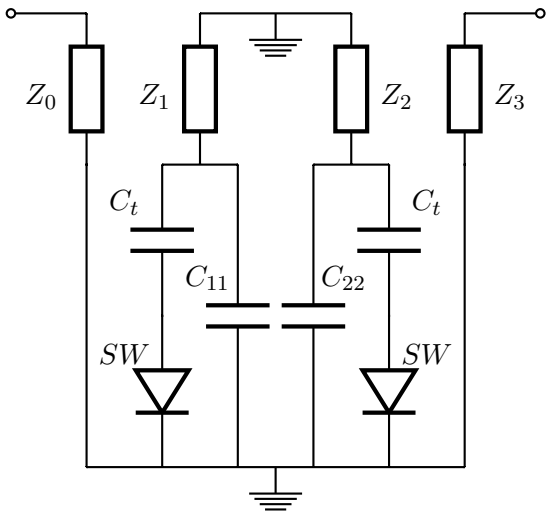

Figure 3.46: Schematic of the reconfigurable coupled transmission line filter using PIN diodes as RF switches.

to limit the possibility of any RF signals in the filter escaping to ground via the biasing circuitry. Lumped element chip-capacitors and -inductors were used for the choke. Lumped components can limit the Q of the filter due to their effective series resistance (ESR); additionally the self-resonance inherent in chip components limits the frequency at which the design should be. Consequently the filter was redesigned to have a centre frequency of $f_c = 600$ MHz for the *OFF* state.

Due to the bulkiness of a suspended-substrate-stripline design, it was decided that the filter be fabricated on microstrip owing to the simpler design procedure and lower fabrication costs. In addition, opposite-sided transformer coupling [54] is used on the input and outputs of the filter since this allows for simple input/output connections to be made.

The spacings between microstrip lines are determined by the external-Q and the coupling coefficients required. Approximate solutions were found through interpolating graphical data laid out in [55]. The optimisation tool on AWR Microwave Office was used to fine-tune the dimensions.

A combline filter is comprised of a number of resonators (two in this case), that are all short-circuited at one end, and loaded with shunt capacitors at the other end, where all resonators share the same orientation. Short-circuits and ground connections were realised by drilling through the substrate and connecting a bonding wire between the ground plane and the microstrip sections as specified in [56]. Effectively this places a small inductance to every ground connection, and therefore partly compromises the response of the filter, adding to losses.

Figure 3.46 shows the schematic design of a combline filter with PIN diodes used to toggle between two capacitive loads. Starting at port one, the input signal is connected to the first of four coupled microstrip lines. The two resonators, in the middle of the four coupled lines, are grounded at one end and the opposite ends connect to the

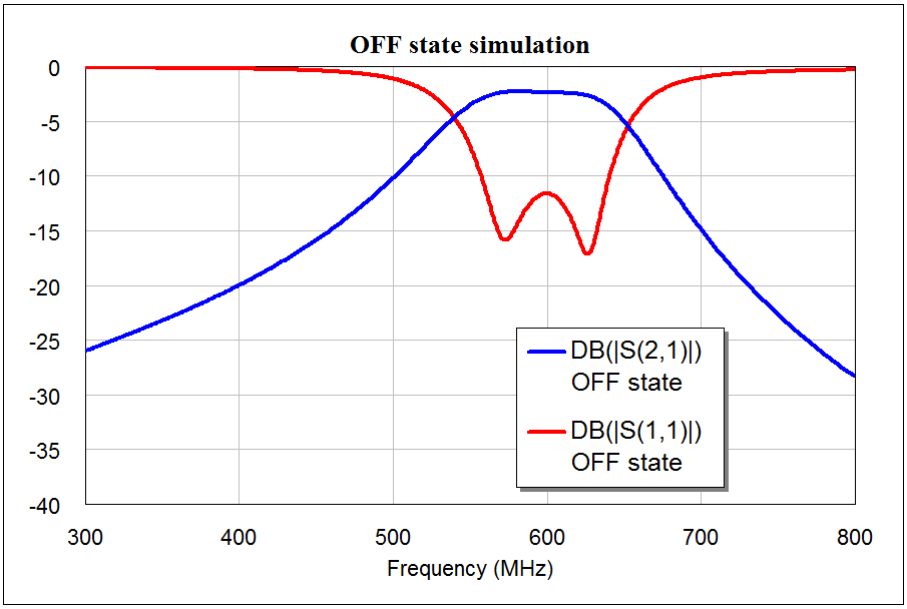

Figure 3.47: Simulated response of the PIN design in the OFF state.

loading capacitors. In the final design short circuits will be realised by attaching a through wire between the circuit and the ground plane. These are taken into account in the simulations (Figures 3.47 and 3.48) with the addition of series stubs at each ground connection. Furthermore, the Q-factors of the chip capacitors have also been taken into account in the simulation.

According to the simulations, the filter is shown to be have losses of about 3 dB in both states and is able to switch from $f_0 = 600$ MHz in the *OFF* state, to just below $f_0 = 500$ MHz in the *ON* state. For the ON state, no 3 dB passband could be measured since the insertion loss is more than 3 dB throughout the frequency sweep. However, a passband of sorts is clearly visible, appearance-wise it shows a close resemblance to the 80 MHz bandwidth of the *OFF* state.

The final design specifications for fabrication were generated by Microwave Office. Additional pads were added manually in order to connect the loading capacitors and diode bias sections. A picture of the fabricated design is shown in Figure 3.49. As it can be seen a resistor was retrofitted instead of a connector for the bias line. The reason being that the current flowing through the diode in the *ON* state can be more closely measured and controlled.

The *OFF* and *ON* state responses of the fabricated prototype are shown in Figures 3.50 and 3.51 respectively. What is apparent at first glance is that the filter is shown to have more loss than was predicted by the simulations. Additionally in the *ON* state, there is a significant change in insertion loss across the pass band. Two possible explanations for these phenomena could be that the loss of the input and output SMA connectors was not taken into account in the simulations. Furthermore, the bounce seen in the passband for the *ON* state and not in the *OFF* state appears to suggest that the bias network is affecting the system impedance, resulting in an impedance

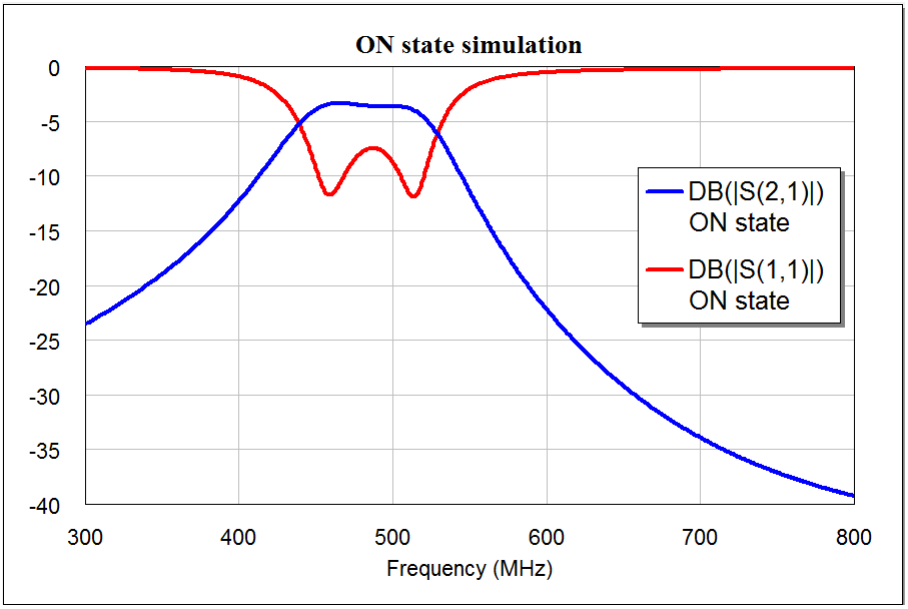

Figure 3.48: Simulated response of the PIN design in the ON state.

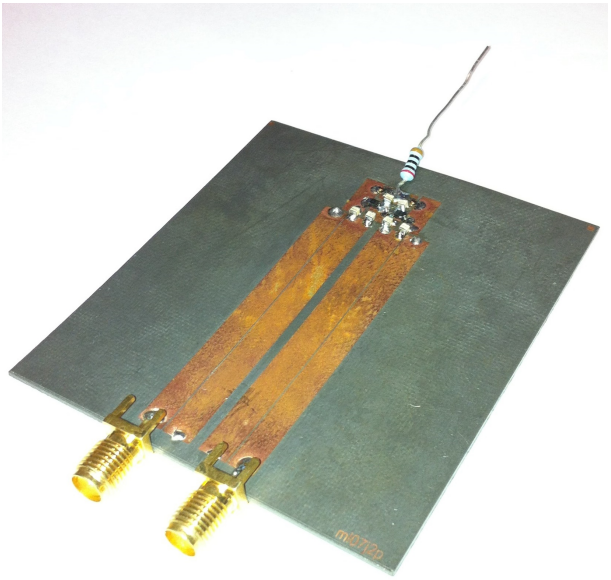

Figure 3.49: A picture of the fabricated bandpass switchable filter design.

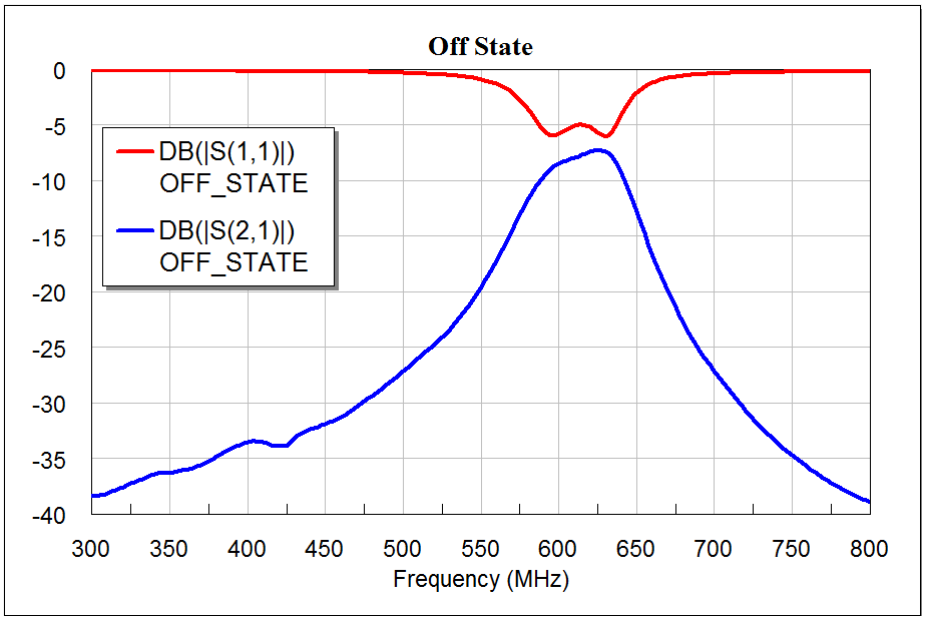

Figure 3.50: Fabricated design S-parameter response for the OFF state.

mismatch when the PIN diodes are switched on. Matching the bias network to 50 Ω at the midpoint frequency would help to alleviate this issue.

The choice to implement opposite-sided transformer coupling at the input and output of the design could have limited the tunability performance of the filter. According to [4] a combline structure implementing same-sided transformer coupling can achieve an approximately constant bandwidth over a broad tuning range.

Intermodulation distortion measurements were recorded for the fabricated design using two-tone characterisation testing. The tones were internally generated using the Agilent E4438C vector signal generator, which connected directly to the input of the filter. Thereby ruling out the need for a Wilkinson combiner between the signal generator and the filter's input. The output spectrum was measured using the Agilent E4407B spectrum analyser, which connected directly to the output of the device under test. Therefore no intermediary components were needed in between the device and testing equipment, simplifying the overall procedure.

Tests were carried out on four different bias settings, two for each state. Firstly the *OFF* state measurements were carried out with a voltage bias across each diode of $V_b = -10$ V and -20 V. Both tests returned the same third-order intercept values (Figure 3.52) of 34.05 dBm, showing that the difference in isolation between the two bias voltages in the *OFF* state is negligible.

This was reflected in the results for the *ON* state, which was recorded at 33.7 dBm for forward currents of 25 and 50 mA.

What can be deduced from the results gathered is that when compared to the original simulation (Figure 3.45) for the intermodulation distortion predicted IP3 values far higher than what was achieved in practice. The diode model used in the simulations

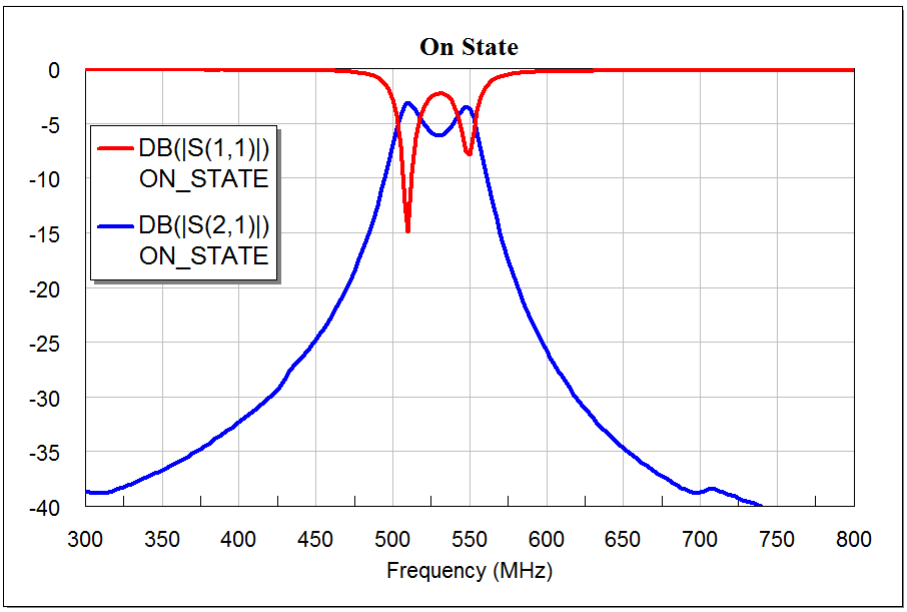

Figure 3.51: Fabricated design S-parameter response for the ON state.

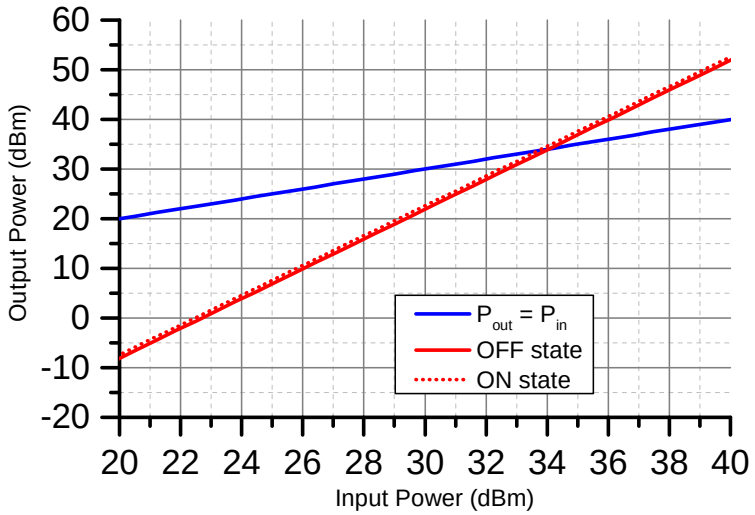

Figure 3.52: Two-tone characterisation measurement results for a PIN diode reconfigurable filter.

comes into question. The varactor model used for simulations in section 3.3.1 was based on a commercially available product and so modelled using real data gathered from the device. The PIN diode used in the simulations however was based upon ideal equations, not taking into account the real-world discrepancies seen in commercial devices. A model consisting of data gathered from a commercial device could have produced more accurate results.

3.4 Review

Existing technologies have been compared via the literature. YIG spheres tune resonance as a function of an applied DC magnetic field. They can produce large tuning ranges and Q factors, but suffer from bulkiness. BST varactors, PIN and varactor diodes offer size reduction advantages at the expense of Q, however they are limited by power handling and non-linearities.

Varactor and PIN diode tuned filters are then tested via simulation software for effectiveness in tunability. Harmonic balance was used to test the linearity of filters implementing such devices. A varactor diode was shown to have poor intermodulation performance for three different bias voltages. Concurrent with the literature. Simulations for a PIN diode frequency switching filter yielded surprising third-order intercept points. A Combline filter was then fabricated in microstrip using chip capacitors that can be switched in and out of the circuit using commercially available PIN diodes. The filters were shown to switch the operating frequency by about 75 MHz despite exhibiting large losses. The measured third order intercept point was far less than was predicted in simulations.

Chapter 4

Methods of Performing Bandwidth Tunability

4.1 Capacitive Coupling Mechanism

Bandwidth tunability is achieved by controlling the coupling between resonators. This relies on perturbation of the EM fields in the coupling region, by either reducing or increasing the energy transferred via either of the electric or magnetic fields. This can be achieved in numerous ways.

Figure 4.1 shows a circuit model for the coupling between two resonators (r and $r+1$) with a tunable capacitance, C_t added in parallel. For reference, the complete combline equivalent circuit is shown in figure 2.14. Coupling impedance between the rth and $(r+1)$th resonators in a combline circuit model can be calculated for a given electrical length of the resonators (θ_0) using the design equations in [4]:

$$Z_{r,r+1} = \frac{n_r n_{r+1}}{K_{r,r+1} \tan(\theta_0)} \tag{4.1}$$

Where $K_{r,r+1}$ is given by the inverter-coupled low pass prototype. n_r (and subse-

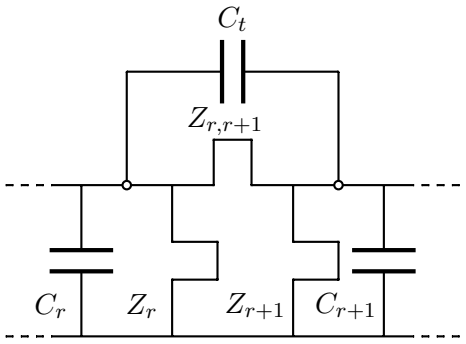

Figure 4.1: Tunable coupling between the rth and (r+1)th resonators in a Combline filter (see figure 2.14) provided by the introduction of a parallel capacitance, C_t.

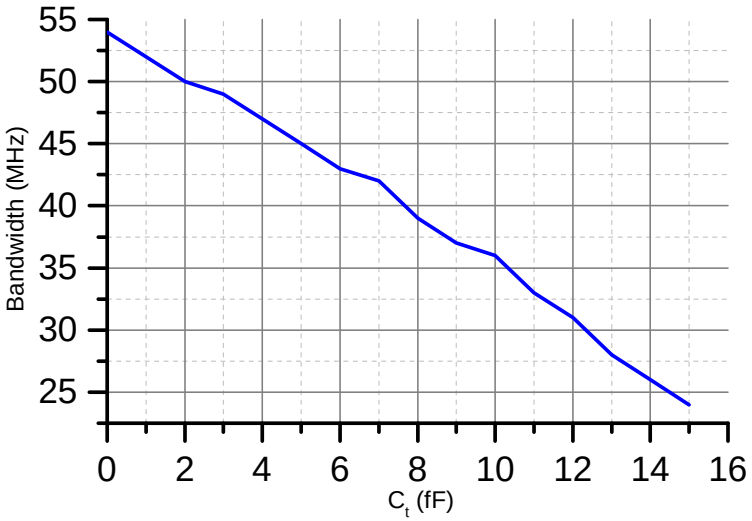

Figure 4.2: Simulated 15 dB bandwidth for a second-order combline circuit model with parallel coupling capacitance.

quently n_{r+1}) are also calculated from terms in the prototype, in this case the shunt capacitance, C_{L_r}:

$$n_r = \sqrt{\frac{\alpha C_{L_r} \tan(\theta_0)}{Y_{rr}}} \tag{4.2}$$

Here α is the bandwidth scaling factor, and Y_{rr} can be chosen to be 1 for simplicity.

The combline circuit model for coupling between the r and $r+1$ resonators is shown in figure 4.1. A capacitance, C_t has been added in parallel to the coupling. Due to the parallel orientation of C_t and $Z_{r,r+1}$, it becomes easier to continue this discussion in terms of admittance since the total admittance of a network of parallel admittances is the sum of each admittance in the network.

The admittance of a capacitor is given by the equation:

$$Y_C = j\omega C \tag{4.3}$$

From equation 4.3, it can be seen that as C increases, so does its admittance, and therefore so does the total overall coupling admittance, $Y_{coupling}$, in this case given by:

$$Y_{coupling} = Y_{r,r+1} + Y_{c_t} \tag{4.4}$$

Since $Y_{coupling}$ increases with C_t, the coupling between resonator r and $r+1$ is said to become stronger, and therefore the coupling bandwidth between even and odd modes will reduce — resulting in a smaller bandwidth.

The effect of a parallel tuning capacitance on the 15 dB bandwidth of a simple two-pole circuit model equivalent filter designed with at a centre frequency of 2 GHz is shown in figure 4.2. Here, the correlation between C_t and bandwidth is clearly shown to be

negative — as expected. For completeness the short-circuit stub impedances, electrical length (θ_0), and loading capacitance to ground used to generate the graph in figure 4.2 were as follows:

$$\begin{aligned} f_0 &= 2 \text{ GHz} \\ \theta_0 &= 60^\circ \\ Z_0 = Z_3 &= 70.9287\ \Omega \\ Z_1 = Z_2 &= 79.5167\ \Omega \\ Z_{01} = Z_{23} &= 145.2992\ \Omega \\ Z_{12} &= 882.025\ \Omega \\ C &= 0.9189 \text{ pF} \end{aligned}$$

Having determined the effect of capacitance on inter-resonator coupling, it becomes necessary to employ a method for its realisation. The capacitance between two terminals (for example two parallel plates separated by air) is defined as the constant of proportionality between the current flow and the time derivative of potential difference across the terminals [10].

$$I(t) = C\frac{dV}{dt} \tag{4.5}$$

It can also be calculated as a function of the properties of two parallel plates separated by a known homogeneous insulator:

$$C = \frac{\varepsilon A}{d} \tag{4.6}$$

Where ε is the absolute permittivity of the insulating medium (calculated as a multiplication of its relative permittivity, ε_r and the permittivity of free space, ε_0). A and d refer to the area of a single plate and the separation distance between the two plates respectively.

Suspension of a single metallic plate between two rectangular resonators provides a capacitance between them (see figure 4.13 for reference). In this case, technically it would be two similar capacitances (first-resonator to plate, and plate to second-resonator) in series across the coupling, however basic circuit theory allows us to combine these into one capacitance of roughly half the individual capacitance values.
Imagine the plate is now rotated about its vertical centreline, the effective area of the plate seen by the resonators now reduces. Therefore knowing that capacitance is proportional to area (from equation 4.6), it can be inferred that a tunable capacitance, such as C_t from figure 4.1 can be achieved through the introduction of a rotating plate placed between resonators.

The effective plate area, A_{eff} seen by the resonators as a function of rotation angle ϕ° can be calculated as follows:

$$A_{eff}(\phi) = h[w\sin(90-\phi) + t\cos(90-\phi)] \tag{4.7}$$

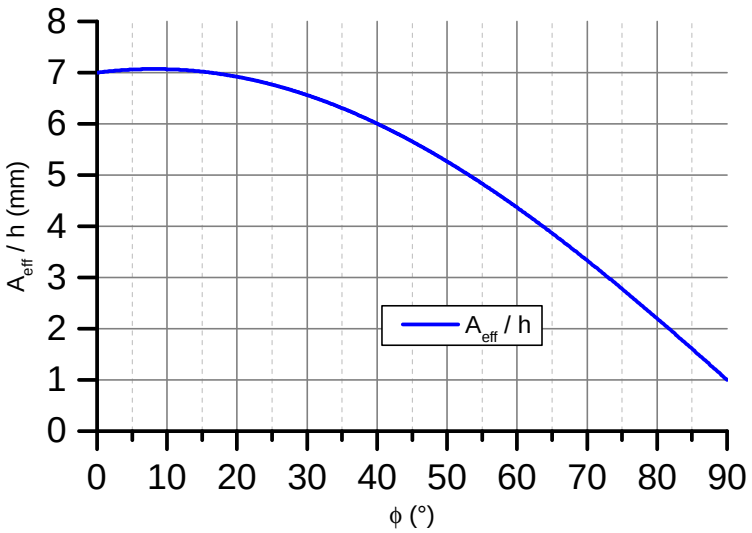

Figure 4.3: Normalised effective plate area as seen by the resonators for rotation angles of $\phi = 0°$ to 90°.

Which can be simplified and normalised by h, giving:

$$\frac{A_{eff}(\phi)}{h} = w\cos(\phi) + t\sin(\phi) \tag{4.8}$$

Where w, h and t refer to the width, height and thickness of the plate respectively.

Figure 4.3 shows a graph of how A_{eff} changes as ϕ increases from 0° to 90°. Scrutiny of the graph shows that from roughly 30° to 90° the effective area seen by the resonators changes in a linear-like fashion. For clarity's sake, it is important to note that this is strictly not a linear relationship but for all intents and purposes given the context, the graph approximates a straight line in this range, hence the usage of the term linear-like. It follows that, with reference to equation 4.6, utilisation of a rotating plate as a means to provide capacitance across inter-resonator coupling, one can expect the capacitance to also change in a linear-like fashion from about 30° to 90°.

Remembering equation 4.6, the capacitance of the single plate coupling mechanism described above can also be increased by reducing the distance between itself and the resonators. This would prove to be difficult to achieve with a single plate, since moving it close to one resonator consequently moves it away from the second resonator — negating the desired increase in capacitance. Instead, if the mechanism were to consist of two plates electrically connected via a wire (illustrated in figure 4.4), the distance between the mechanism and the resonators would reduce and the new capacitance would become larger. Therefore a larger tuning range would potentially be possible. The wire connection between the two plates is required in this case to avoid a self-capacitance being generated by the mechanism. This would be equivalent to three capacitors in series across the coupling gap, thereby reducing the overall value of C_t.

Figure 4.5 shows a closer view of the wire-connected two-plate mechanism. Parameter

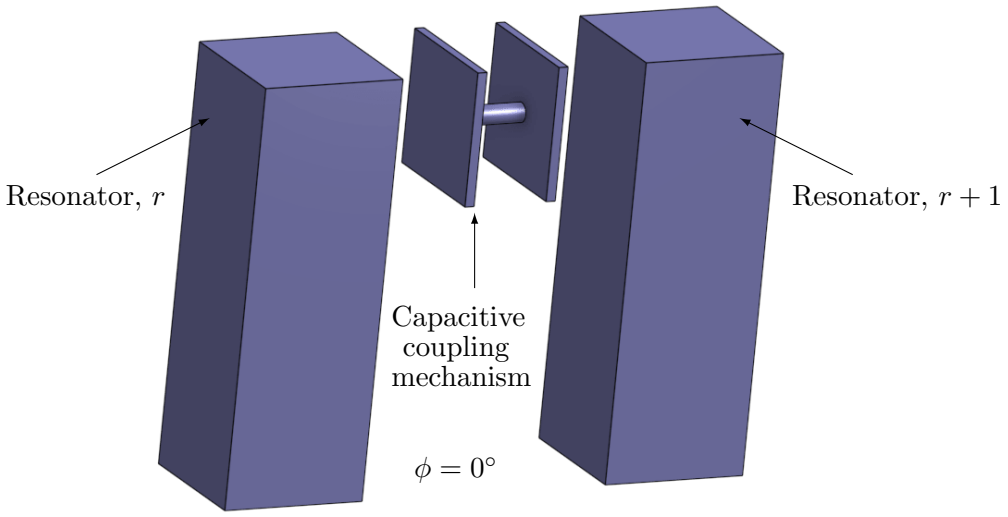

Figure 4.4: Configuration for introduction of tuning capacitance across inter-resonator coupling.

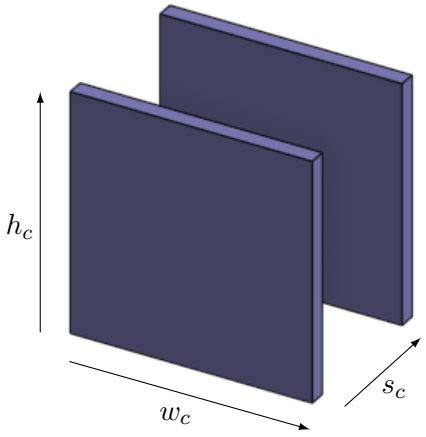

Figure 4.5: Bandwidth tuning mechanism from figure 4.4 — parallel plates connected by a wire.

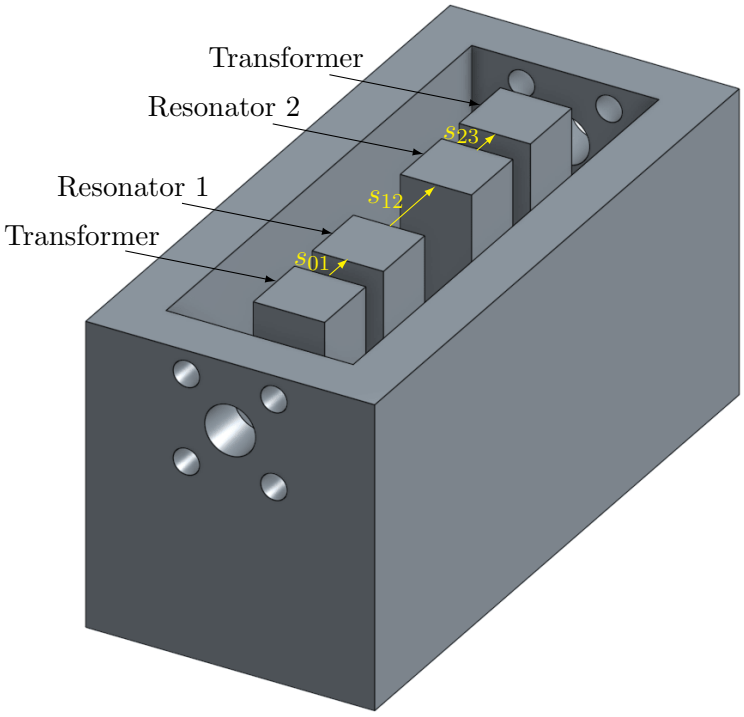

Figure 4.6: A basic three-dimensional two-pole rectangular bar filter structure layout.

values, with a subscript denotation for capacitance, w_c, h_c, and s_c are assigned to the mechanism, representing the width, height and plate-spacing. Knowing the inter-resonator spacing (s_{12}), the distance from a resonator the capacitive mechanism can be calculated as follows:

$$d = \frac{s_{12} - s_c}{2} \tag{4.9}$$

And knowing that the plate area is

$$A = h_c w_c \tag{4.10}$$

Substitution of (4.9 & 4.10) into (4.6) and remembering from circuit theory that two identical capacitors in series are the equivalent of a single capacitor of half the capacitance, an estimation can be made as to the overall coupling capacitance, C_t introduced to the filter using the following formula:

$$C_t = \frac{\varepsilon_0 \varepsilon_r h_c w_c}{(s_{12} - s_c)} \tag{4.11}$$

A three-dimensional Combline cavity second-order filter with rectangular bars (figure 4.6) was designed following design procedures laid out in [4] and [6]. The filter was

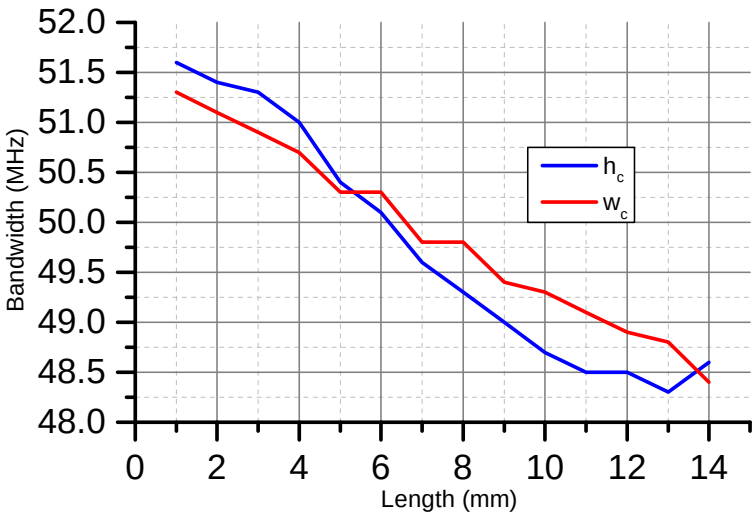

Figure 4.7: The variation of bandwidth with plate height (h_c) and width (w_c). Note that at 2 GHz, $\lambda = 150$ mm — significantly more than the dimensions of the plate. Therefore any resonance of the plate will occur sufficiently out of band to not affect filtering performance.

designed to meet the following specifications:

$$f_0 = 2 \text{ GHz}$$
$$\theta_0 = 60^\circ$$
$$\Delta f = 50 \text{ MHz}$$
$$RL_{passband} \geq 15 \text{ dB}$$

The filter was then constructed in HFSS and a model of the capacitive coupling mechanism from figure 4.5 was inserted equidistantly from resonators 1 and 2. The mechanism height was arbitrarily chosen so that the tops of the mechanism can the resonators lined up. This is because for a combline cavity structure, it is well known that the electric field is at its strongest towards the open-end of the resonator.

Due to the addition of the new mechanism, the response of the filter deteriorated somewhat. Therefore the input- and resonator-spacings (s_{01} and s_{12} respectively) were modified accordingly to bring the response back to the desired specification with the tuning mechanism in place.

To begin with, parametric sweep analysis was performed on h_c, and w_c. This was for two reasons — firstly, to check that the mechanism itself was indeed exploiting the electric field between the resonators resulting in the generation of capacitance, C_t. Secondly, to see whether the capacitance can be optimised for the maximum tuning effect.

It has been shown that for a larger C_t the bandwidth is expected to reduce. In addition, it was also shown that as the plate area is increased, C_t also increases. Therefore the expectation would be that the bandwidth should decrease with rising h_c and w_c. Figure

4.7 confirms this for both the width and the height of the mechanism as is shown by the general negative gradient in both plots. One curious point to note is that h_c has a larger effect on the change in bandwidth than the w_c. It would be foolish to jump to any conclusions based purely on this graph alone since there is only a small change in bandwidth across the entire sweep, and the deviation between results are plausibly within the error bounds of the simulation engine. It could however be argued that one would expect h_c to have a slightly greater effect of the bandwidth than w_c, at least for lengths of less than 10 mm.

The E-field coupling is strongest in the region between the top halves of the resonators. As the mechanism width (w_c) is increased, the mechanism is spreading its plate area where the E-field strength remains relatively constant, thus the bandwidth is shown to change at a relatively constant rate. As h_c is increased however, a rapid change in bandwidth is seen from around $h_c = 4\,\text{mm}$ to $10\,\text{mm}$. For lengths above 10 mm, the rate of change of bandwidth starts to level out. Based upon this phenomenon it would indicate that the strongest E-field in the coupling region is not exactly at the top of the resonators, but in fact somewhere around 4 mm to 10 mm from the open-circuited ends. Given that the electrical length of the resonators $\theta_0 = 60^\circ$ at $f_0 = 2$ GHz, the physical length of the resonators (L_{res}) (assuming a velocity factor of 1) is given by the following formula:

$$L_{res} = \frac{\theta_0 c}{360 f_0} \tag{4.12}$$

Where c is the speed of light in a vacuum. $L_{res} = 25$ mm, therefore the strongest E-field in the coupling region is at a height between 60% and 84% of the resonator length.

As h_c is extended beyond 10 mm, the mechanism is no longer expanding in the strong E-field region and therefore the rate of change in bandwidth for h_c begins to slow down. This is because the E-field diminishes with proximity to the base of the resonators, where they are electrically grounded. This region is where the H-field strength is strongest.

For the design of a bandwidth tunable filter using a capacitive element in the coupling, knowledge of where the electric coupling is strongest can be invaluable as it allows the designer to know exactly where the coupling mechanism needs to be placed to produce the maximum effect in tuning the coupling bandwidth. Figure 4.8 shows a plot of the simulated data gathered when the height of the mechanism upper edge is parametrically swept from 10 % to 120 % of the resonator length when measured from the short-circuited end. Three different plate areas were used so that three different values of coupling capacitance were tested. The capacitance for each plot was estimated using the formula in equation 4.11.

The plots in figure 4.8 agree with the conclusions from figure 4.7. Recalling from the discussion above, the electric field strength in the coupling region was estimated to be at its strongest between 60% and 84%. Here it can be definitively seen that the

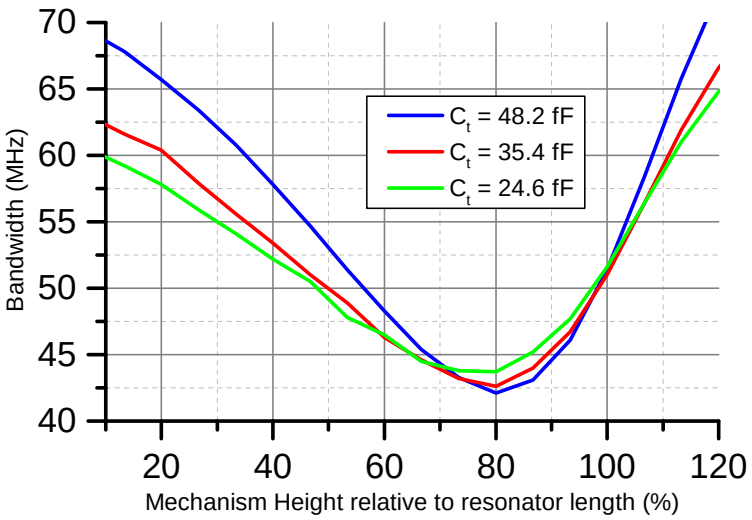

Figure 4.8: Comparison of three mechanisms of differing capacitance and how the bandwidth changes with respect to their height as a percentage of resonator length.

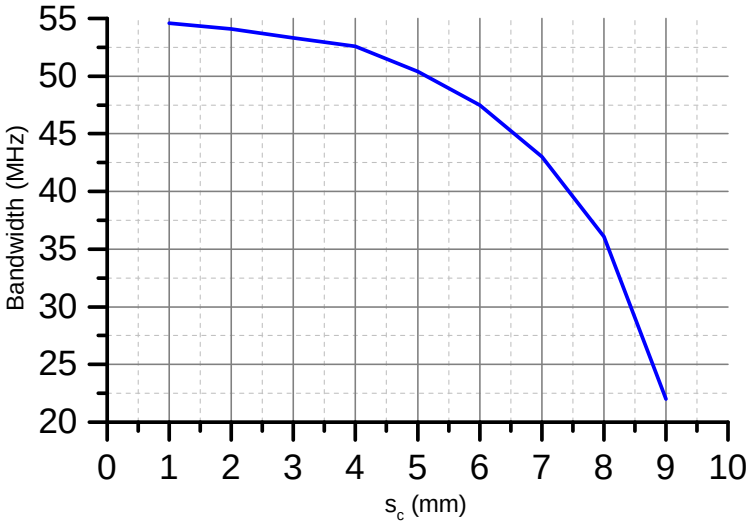

Figure 4.9: A graph of the effect of plate spacing on bandwidth.

bandwidth for three different values of C_t is narrowest when the mechanism is placed at a height of 80% of the resonator length. Since the narrowest bandwidth is indicative of capacitive element being placed in the strongest electric field region, it can now be said that the optimum height for the placement of a capacitive coupling mechanism is 80% of the resonator.

Figure 4.9 visually represents how the bandwidth changes as the plate spacing, s_c increases from 1 mm to 9 mm. Here the bandwidth decreases at an increasing rate. This is because as s_c changes, it directly alters the separation distance between the resonator and coupling mechanism. Again referring back to equation 4.6, it is known that capacitance is inversely proportional to separation distance. As d decreases, C_t increases at an increasing rate. Therefore it would be expected that the bandwidth would reduce at an increasing rate. Which is confirmed in Figure 4.9 showing that the

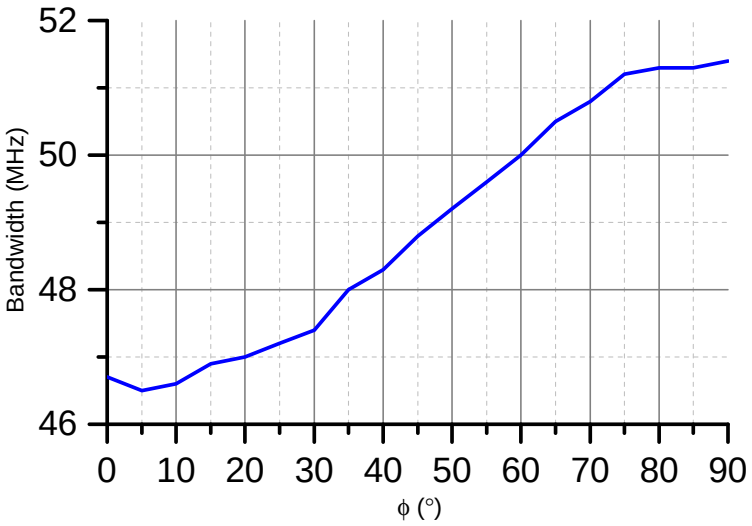

Figure 4.10: Simulated bandwidth response for varying mechanism rotation angles (ϕ).

mechanism proposed in figure 4.4 is indeed exploiting the electric field between the resonators.

Naturally it follows that a simulation showing how the bandwidth of the filter changes as the mechanism is rotated should be tested. For a rotation from $\phi = 0°$, where the mechanism plates face the resonators (the same as in figure 4.4), to $\phi = 90°$. It would be expected that the bandwidth is at its smallest value for $\phi = 0°$, steadily rising until $\phi = 90°$ where the maximum bandwidth would be seen. Figure 4.10 shows the results of this simulation and agrees with the hypothesis. The bandwidth is shown by the simulation to be tunable in this method from about 46.5 MHz to 51.5 MHz — giving a total bandwidth tunability of 5 MHz or about 10.7%.

It should be noted that coupling tunability does not have to be limited to tuning the size of a passband at a static centre-frequency. Since couplings are known to be frequency dependent, the bandwidth will naturally change with centre-frequency. Therefore tuning of the couplings can be implemented for scenarios where a constant bandwidth is required over a frequency range. Figure 4.11 shows plots of the maximum and minimum bandwidths achieved for the coupling mechanism hitherto discussed. In this case the filter was designed to have a bandwidth of 55 MHz at a centre-frequency of 2 GHz somewhere close to the centre of the bandwidth tuning range. Sweeps of the bandwidth tuning range were then performed at discrete centre-frequency points in steps of approximately 60 MHz.

What this graph shows is that even with a relatively small bandwidth tuning range (of about 10% in this case), a relatively wide range of bandwidth stability is achievable. For example here, a constant bandwidth of 55 MHz is specified over a range of centre-frequencies, it is shown to be achievable in this case from 1.85 GHz to 2.57 GHz. It stands to reason that a bandwidth tuning mechanism able to provide larger coupling tunability would be able to produce a constant bandwidth filter over a larger range of

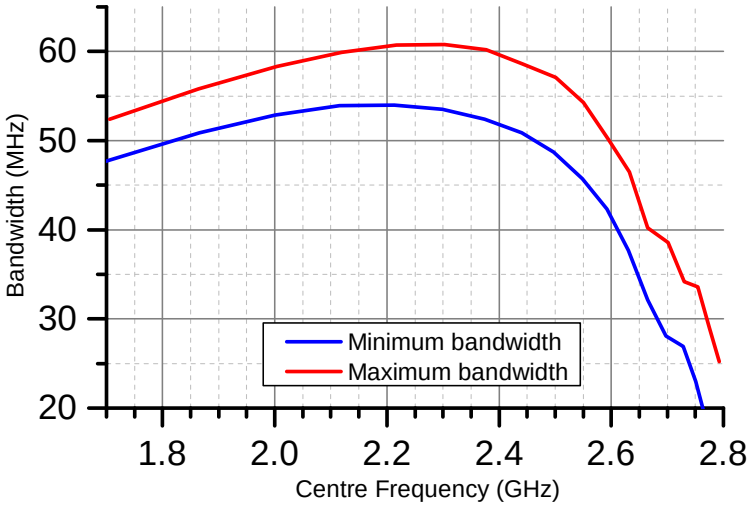

Figure 4.11: Comparison of maximum to minimum bandwidth states across a frequency range.

centre-frequencies. The key for optimising this type of filter would be to predict the frequency and bandwidth at which the bandwidth turning point occurs for the minimum bandwidth state. If the turning point of the minimum bandwidth were able to be designed from first principles to peak ever so slightly lower than the desired constant bandwidth, an optimised constant bandwidth filter over a maximum centre-frequency range would be achievable. This would be an interesting avenue for exploration in future research projects.

Methods for achieving the maximum bandwidth tuning range with the capacitive mechanism proposed in figure 4.10 have heretofore been designed through exploitation of the parallel plate capacitance equation (4.6). If there are further techniques for optimisation in this manner, they are beginning to appear scarce. There is however, at least one more design method that can be utilised for this mechanism.

Simulations until now have helped build a picture of how the E-fields between rectangular bar resonators interact. It has been assumed that the larger the capacitance at $\phi = 0°$, the larger tuning range will be achieved. It has also been shown that the largest capacitance is achieved when the E-fields are at their strongest. Therefore the next technique proposes a method for optimising the E-field coupling. This can be achieved by placing a wall in between resonators which limits the magnetic coupling as much as possible. An iris (figure 4.13), or cut-out section of the wall, is placed where strong electric coupling between resonators is desired. The mechanism can then be placed in this iris. The effect of using an iris allows for the resonator spacing (s_{12}) to be reduced. The amount of reduction can be controlled by the size of the iris. Therefore resonators can be theoretically placed at any desired spacing.

Figure 4.12 compares how the bandwidth changes with rotation of the mechanism when an iris is utilised to when it is not. Clearly a significant improvement on the bandwidth tunability of the filter is seen with the introduction of the iris. In addition, inclusion

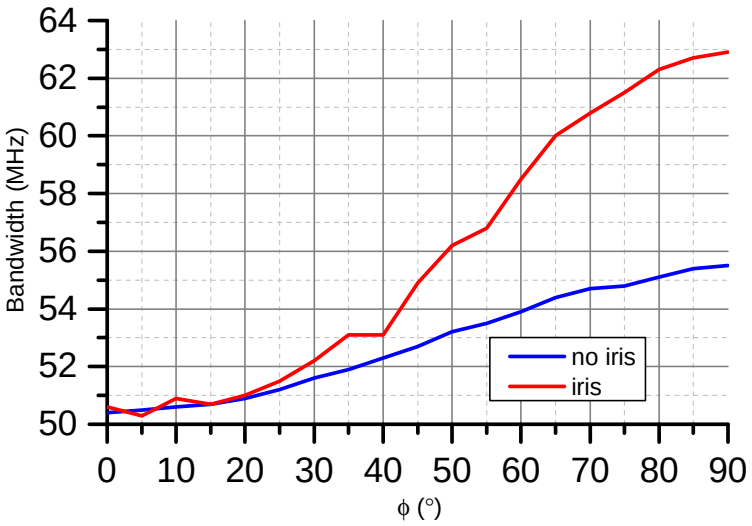

Figure 4.12: A comparison how the bandwidth changes with ϕ when an iris is for a two-plate mechanism.

of an iris in the design provides a convenient side effect. Not only is the tunability increased, but the resonator spacing is reduced and therefore so is the overall volume of the filter. This saves on the cost of fabrication and manufacturing should this design go on to be realised.

Analysis of figure 4.12 shows that for this setup, when the iris is included, a tunability from 50.6 MHz to 62.9 MHz (24%) is observed. This is more than double the tunability achieved when no iris is present (10%) — confirming that the E-field can be exploited to a larger extent when an iris is used.

Thus far, simulation tests have been performed using a single type of capacitive mechanism. The interaction of the introduced element with the E-fields in the coupling have been explored and based on the results, the optimum setup for bandwidth tunability has been designed. What remains to be explored are different implementations of the mechanism.

The current setup consists of a mechanism made from two electrically connected parallel plates. It would be interesting to see how well a single rotating plate tunes the bandwidth. This single plate mechanism, along with the coupling iris is shown in figure 4.13. The dimensions of the single plate used here were kept consistent with the two-plate mechanism previously tested, where $h_c = w_c = 5$ mm. In order to be consistent with previous simulation tests, the filter was designed at $\phi = 0°$ (where the maximum plate area is exposed to the resonators), to have a bandwidth of 50 MHz. On first inspection of figure 4.14 one important point of note immediately stands out — the bandwidth decreases with increasing ϕ. This would point to the capacitance increasing with ϕ, the opposite of what is predicted by figure 4.3. How can this be? The area seen by the resonators is getting smaller, therefore the capacitance should reduce as well should it not?

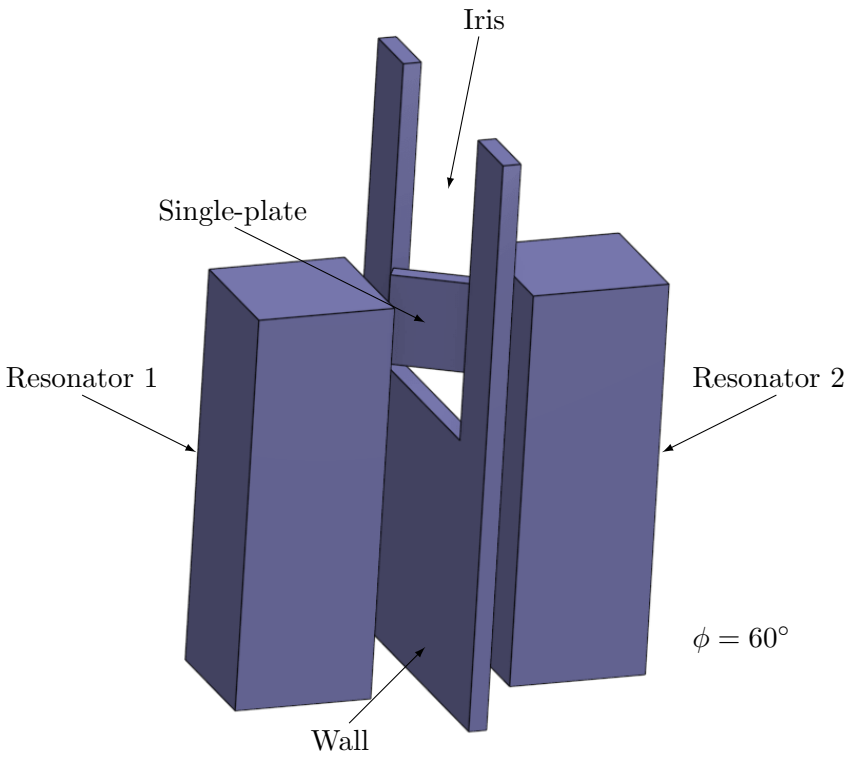

Figure 4.13: Three-dimensional configuration of the single plate mechanism between two resonators with a coupling iris.

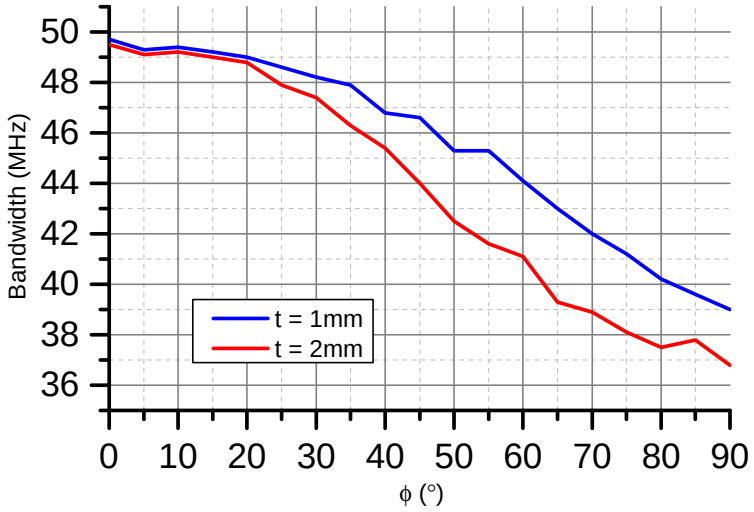

Figure 4.14: Bandwidth plotted against rotation angle for a single plate mechanism of two different plate thicknesses, t.

The solution to this conundrum originates from the assumptions made from figure 4.3. It was originally shown that capacitance is proportional to plate area in equation 4.6. Therefore C_t would be expected to decrease with plate area as the mechanism rotates from 0° to 90°. This is true only when assuming d is large enough to not dominate the equation.

When a single plate is used, the inter-resonator spacing required (iris included) to achieve a bandwidth of 50 MHz is little more than the width of the plate. Therefore as the plate angle increases, its side-edges approach close to the resonator and d becomes the dominant term in the capacitance equation. At $\phi = 90°$, despite the effective plate area being so small, if the edges of the plate are close enough to the resonators, the capacitance can be larger than when $\phi = 0°$. This is what is being observed in figure 4.14. Confirmation of this is provided by plotting the bandwidth for two different plate thicknesses (t). When $\phi = 0°$ and for the first few plotted points, the bandwidths observed for each plate thickness are almost identical. As the angle is increased however, it becomes clear that the thicker plate produces a smaller bandwidth. Thereby showing that the maximum capacitance state for this mechanism is actually at $\phi = 90°$ and not at 0° as originally thought.

Scrutinising figure 4.14 a single plate mechanism of thickness, $t = 1$mm is shown to achieve a bandwidth range from 49.7 MHz to 39.0 MHz (-22%). Likewise for $t = 2$mm bandwidth tunability of 49.5 MHz to 36.8 MHz (-26%) is seen — both cases showing better absolute tunability than the original mechanism from figure 4.12.

Understanding now that both the A and d can be exploited for the purposes of bandwidth tunability, it opens the door to other implementations of mechanism for testing. Components that force A to be the dominant term in the capacitance equation, bandwidth increases as the angle of rotation (ϕ) is increased from 0° to 90°. Conversely, for mechanisms exploiting d, the bandwidth decreases with angle.

When proposing the first mechanism (parallel plates connected by wire), it was hypothesised that the wire was required so that a larger coupling capacitance, C_t would be realised — owing to the fact that two capacitors in series provides a larger combined capacitance than when a third series capacitor is added. Which is correct when exploiting the plate area. With the knowledge now that when exploiting d, the largest capacitance state is actually provided by plate thickness at $\phi = 90°$. Therefore when designing a mechanism to exploit d, minimal capacitance at $\phi = 0°$ now becomes the goal for optimising bandwidth tunability.

When three capacitors are connected in series, the combined capacitance will be dominated by the smallest value capacitor of the three. In fact the combined capacitance will be less than the smallest value capacitor of the series network. Proposing a mechanism where two separate parallel plates are not connected together by a wire, so long as the capacitance generated between the two plates is smaller than the two capacitances generated from resonator to plate, a mechanism for exploiting d can be realised.

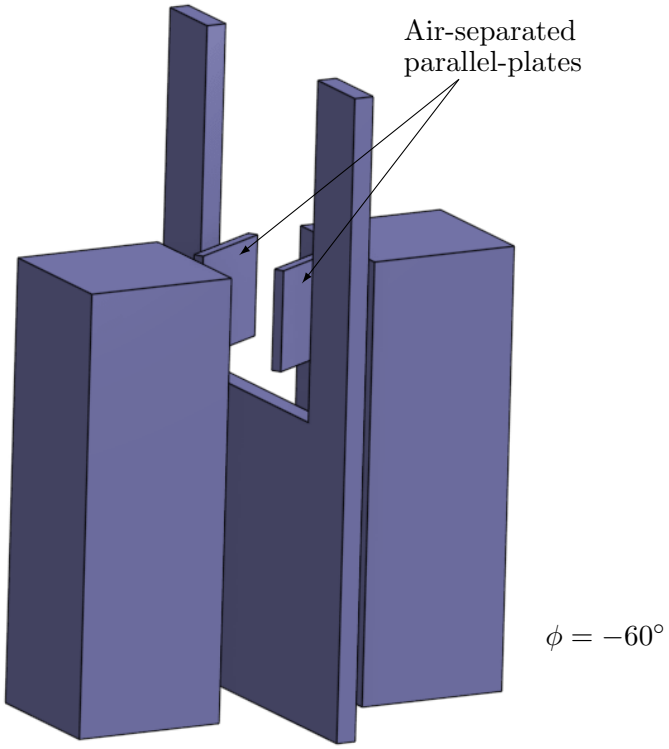

Figure 4.15: Three dimensional representation of the parallel plate mechanism between two resonators.

There is a definite trade-off required when designing this type of mechanism (figure 4.15). Assuming the inter-resonator spacing is kept the same as with the wire-connected parallel plate mechanism from figure 4.4, in order for a d-dominant tuning range to be established, the capacitance between the parallel plates of the mechanism needs to be smaller than the capacitance from the resonators to the respective plates. Therefore the distance separating the plates, s_c, is required to be larger than before. Unfortunately increasing s_c means the plates are closer to the resonators for small ϕ — meaning that capacitance in this range is larger. Compensation for this is provided by increasing the resonator spacing, s_{12}. In turn this causes the capacitance at $\phi = 90°$ to reduce. Therefore optimisation of s_c for a given inter-resonator, s_{12} spacing is required to achieve the best tuning range.

Figure 4.16 shows the optimised two-parallel plates mechanism for forcing d dominance in the capacitance term. It shows bandwidth tunability from 35.6 MHz to 50.3 MHz (41%). This is a larger bandwidth tuning range from before, at the expense however of a larger overall filter volume required due to the increase in s_{12}. The majority of the bandwidth tuning here takes place from $\phi = 0°$ to $60°$. This is because s_c is relatively wide and therefore A and d are competing with each other at this point to be the dominant capacitive term — effectively cancelling each other out.

For the parallel plates mechanism, there are two drawbacks. The first is the increased

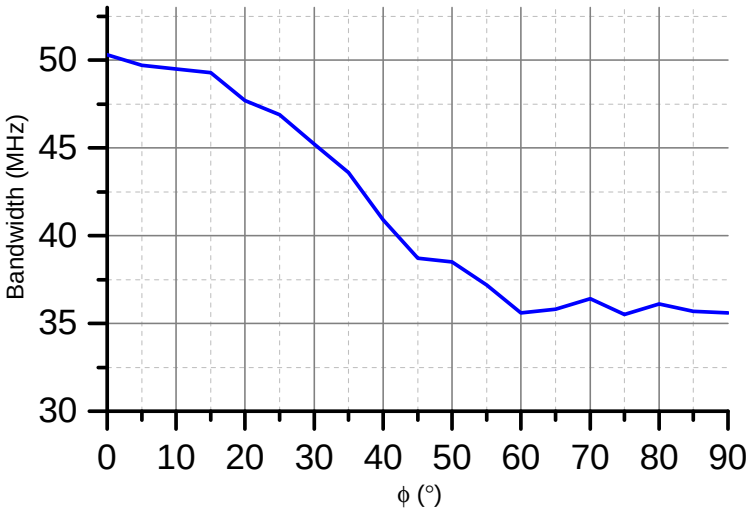

Figure 4.16: Bandwidth against rotation angle for a two-plate mechanism with no connecting wire.

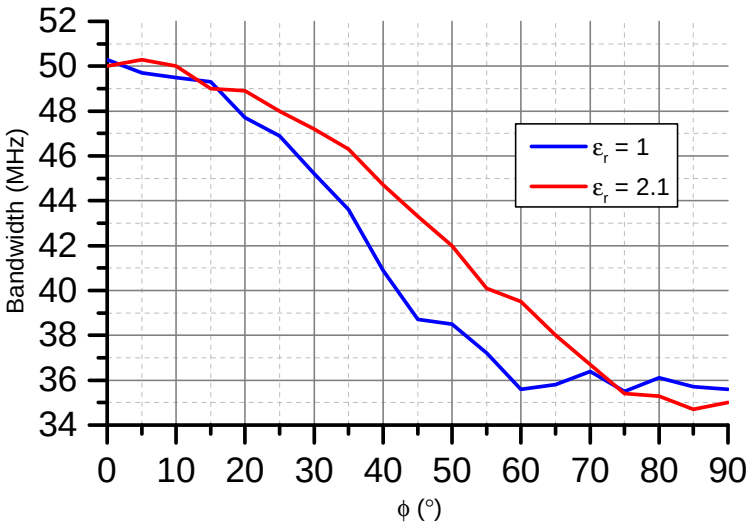

Figure 4.17: A plot comparing the effect of rotation angle on bandwidth for a two-plate mechanism with and without a PTFE block.

inter-resonator spacing resulting in the larger filter volume — consequently larger associated production costs. The second is that almost half of the tuning range is rendered redundant because of the wide plate separation distance. Remembering equation 4.6, the capacitance between two parallel plates is proportional to the relative dielectric permittivity of the insulating medium separating them. Thus far, tests have simulated a separating medium of air, for which the dielectric permittivity, $\varepsilon_r = 1$. Using a material with a larger dielectric constant means that s_c would be able to be reduced proportionally for the same C_t.

Figure 4.16 shows a comparison of bandwidth tunability with rotation for a parallel plate mechanism with and without a polytetrafluoroethylene (PTFE, or as it is more commonly known — Teflon) insulator. PTFE has a relative dielectric permittivity of $\varepsilon_r = 2.1$ therefore the plate spacing was able to be reduced by a half.

The result of reducing the plate spacing has very little effect on the overall tuning range with ϕ, 35 MHz to 50 MHz (42.8%). It does however eliminate the issue of competing A and d dominance in the $\phi = 60°$ to 90° range. Thereby removing redundancy in the tuning range. The downside of the introduction of the dielectric material is the lowering of the filter Q due to losses in the dielectric given by the loss tangent.

4.2 Inductive Coupling Mechanism

The previous section looks at how the E-field inter-resonator coupling can be exploited by efficiently optimising the relative change C_t as a component rotates through 90°. Rectangular bar resonators operate in the TEM mode. Therefore the electric- and magnetic-field vectors in the coupling space operate perpendicularly to each other. Where the E-fields essentially propagate directly from one resonator to another, the H-fields circulate around the resonators. A mechanism that can tune bandwidth via exploitation of the H-field would have to couple into the magnetic-fields around one resonator before coupling into the next. This in effect amounts to an inductance between the resonators. In a similar vein to the mechanisms from the previous section, if a mechanism providing coupling inductance were to be designed in such a way that the H-field coupling is maximised in one state, and minimised in another, optimal bandwidth tunability in the H-field would be achieved.

The inductance in micro-Henries of a single round wire of arbitrary conducting material is given by the following formula [57]:

$$L = 0.002l \left[\ln \frac{4l}{d} - 1 + \frac{d}{2l} + \frac{\mu_0 \mu_r r T(x)}{4} \right] \tag{4.13}$$

Where $T(x)$ originates from Grover [58] and is approximated by:

$$T(x) \approx \sqrt{\frac{0.873011 + 0.00186128x}{1 - 0.278381x + 0.127964x^2}} \tag{4.14}$$

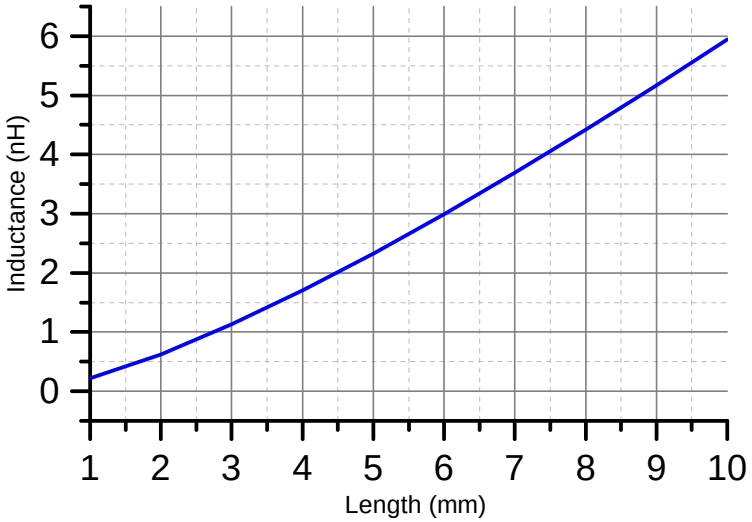

Figure 4.18: Inductance against length for a copper wire with a diameter of 1 mm.

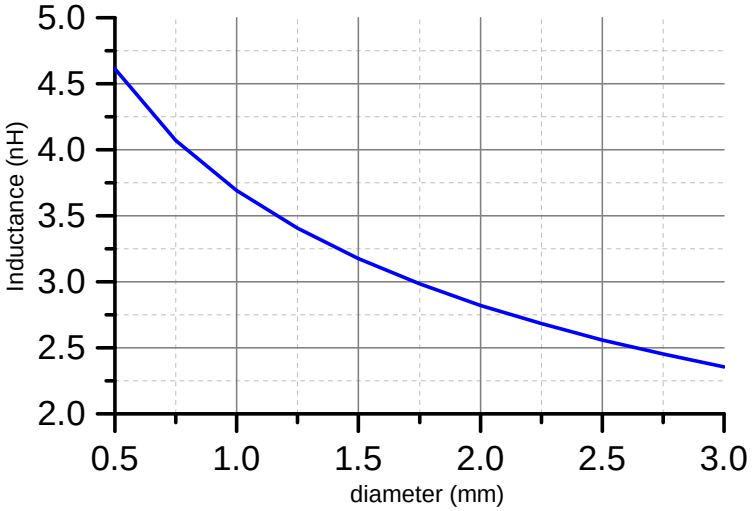

Figure 4.19: Inductance against diameter for a copper wire with a length 7 mm.

And

$$x = 2\pi r\sqrt{\frac{2\mu_0\mu_r f}{\sigma}} \tag{4.15}$$

d is the wires diameter in centimetres, l is the length in centimetres, f is the operating frequency in hertz, r is the radius of the conductor measured in centimetres, finally μ_0 and μ_r represent the magnetic permeability of free space and the relative permeability of the material in question.

Figures 4.18 and 4.19 show how the inductance of a copper wire changes with length and diameter respectively at 2 GHz. The length and diameter ranges observed here are limited to the dimensions by the filter and therefore any prospective mechanism will be unlikely to exceed the parameter values shown in these graphs.

It is shown that there is clear linear positive correlation between wire length and inductance for copper at 2 GHz, therefore designing a mechanism where the length is

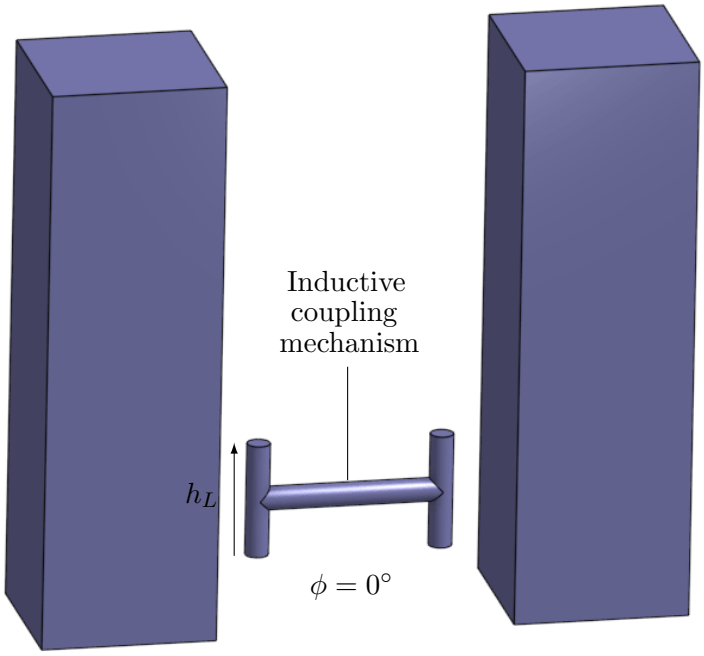

Figure 4.20: Configuration of a proposed wire mechanism for inductively coupling between resonators.

as long as possible will allow for the largest inductance in its high inductance state. In terms of diameter, the inductance will be larger, the thinner the wire becomes.

The first inductive tuning mechanism proposed is shown in figure 4.20. It consists of two vertical wires connected by a horizontal wire. The idea being that one of vertical wire lines up perpendicularly to the H-field around the first resonator. The H-field then induces a current in the mechanism due to Ampres circuital law. This in turn generates a magnetic field around the second vertical wire to couple into the second resonator. Since magnetic fields are generated when a current flows, the strongest magnetic fields will be near regions where the current density is the strongest. For a TEM resonator, this at the bottom of the resonator, close to ground. Therefore the strongest H-fields are found near the base of the resonators. Hence the mechanism is placed low down relative to the resonator height in order to maximise the captured H-field. Since an iris cannot be used in this instance, the inter-resonator spacing will be larger than for th previously tested capacitive mechanisms.

Figure 4.21 shows how the bandwidth of the vertical wire mechanism changes with a rotation angle of $\phi = 0°to90°$. Starting from 0° at 50.1 MHz the bandwidth rises to a maximum of 62.7 MHz as the mechanism revolves. This equates to a tunability of 24.7%. At first glance this appears to be a good start for the testing of inductive mechanisms. The tuning range here is comparable to some of the better performing capacitive mechanisms. It is however, difficult to tell from this plot alone whether it is the H-field which is being exploited, or not. It would be entirely plausible to suggest that the mechanism proposed in figure 4.20 is actually coupling via the electric fields in

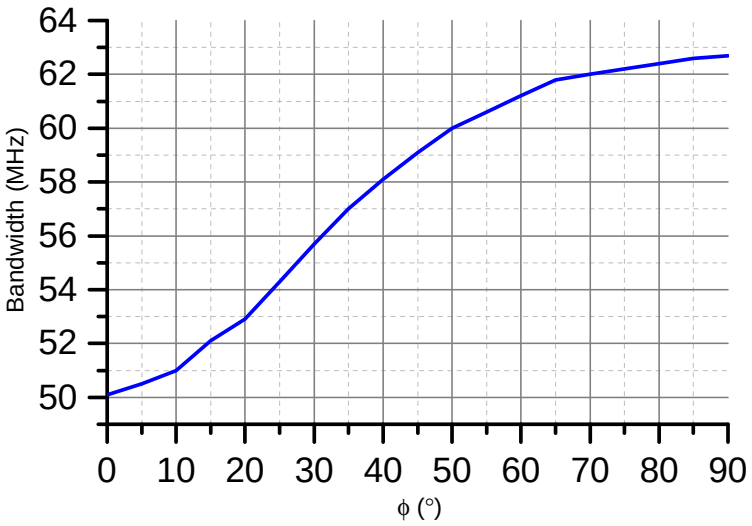

Figure 4.21: A graph of the bandwidth for the rotation angle of a filter utilising the mechanism in figure 4.20.

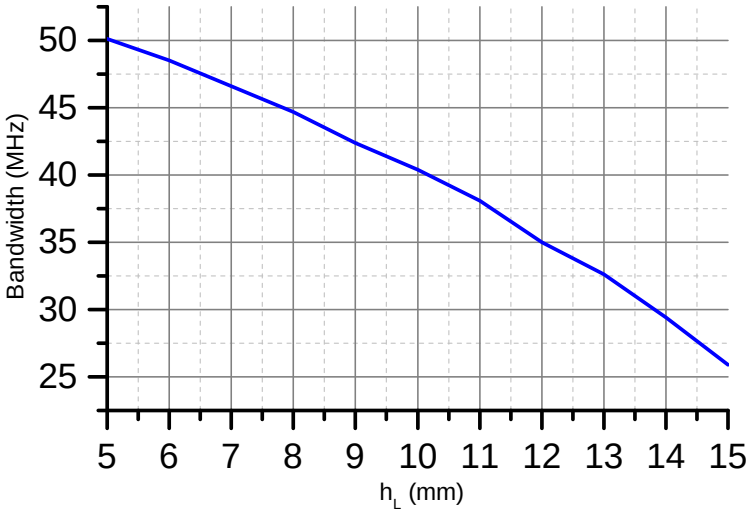

Figure 4.22: A depiction of the change in bandwidth with H_L, for a filter of the type in 4.20.

the filter. It would be a relatively straight forward procedure in order to test whether the mechanism is coupling capacitively or not.

Since capacitance in the coupling is known to reduce the bandwidth and is proportional to the area exposed to the resonators, an increase in the vertical wire length, h_L, would result in a smaller bandwidth being observed. Figure 4.22 shows a plot of the bandwidth as h_L is increased from 5 mm to 15 mm. The bandwidth is clearly shown to diminishes with increasing h_L. Therefore concurring with the original suspicions that the mechanism is utilising the E-field and not the H-field as intended.

Another test that will show conclusively whether the mechanism is coupling inductively or not would be a sweep of the relative height of the mechanism to the resonator length. Recalling figure 4.8, it was shown that the maximum capacitance between resonators

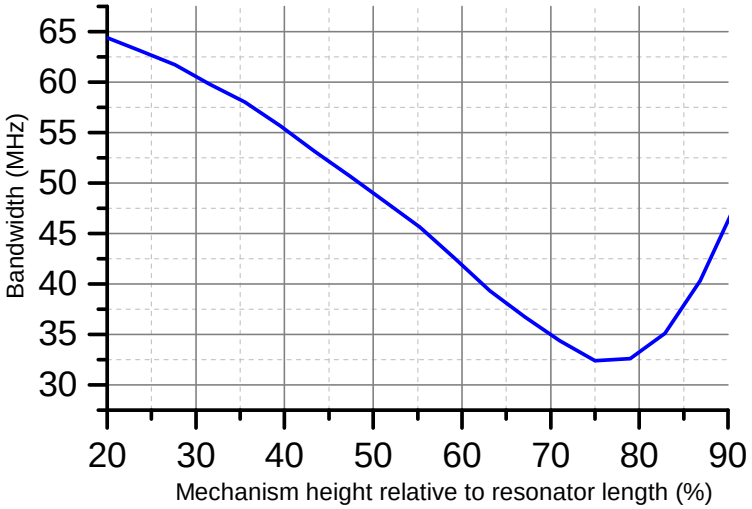

Figure 4.23: A measure of bandwidth against mechanism height as a % of resonator length for the mechanism in figure 4.20.

is achieved at close to 80%.

Figure 4.23 shows how the bandwidth changes as the wire mechanism height rises. A minimum in bandwidth is observed to occur between 75% and 80%. Further evidence that this element is in fact a capacitive mechanism and not inductive.

On reflection it is understandable to think that the mechanism proposed in figure 4.20 acts capacitively. Since a magnetic field is generated by the flow of a current in a wire, a mechanism that allows for the smoothest flow of current from one side to the other will generate the strongest H-field. The supposed inductive mechanism currently proposed is configured to have an H shape. Looking at the connections between the horizontal and vertical wires, it is clear to see there are multiple paths down which the current can flow. This impedes the overall current. A different mechanism is proposed in figure 4.24. This mechanism is, in principle, similar to the last in the way that a current is desired to be induced by the magnetic fields around the resonator, in turn generating an electric field at the other end to couple into the next resonator. The difference with this mechanism is that it is designed to allow for unimpeded current flow between one side and the other by creating a current loop. Therefore it can be expected that whatever the current is on one side of the element, the same (although technically opposite sign) current should be seen at the other.

Figure 4.25 is a graph of the bandwidth with rotation for the mechanism illustrated in figure 4.24. A bandwidth tuning range of 49.8 MHz to 32.6 MHz (−34.5%) is shown.

Contrary to the previous mechanism which was eventually proven to be exploiting the electric- instead of magnetic-fields, this mechanism is exhibits a narrower bandwidth with increasing rotation angle — the opposite to before. An early indication that the rectangular mechanism used here is actually utilising the H-fields to provide coupling tunability. Naturally, as previously shown, it would be expected that capacitive cou-

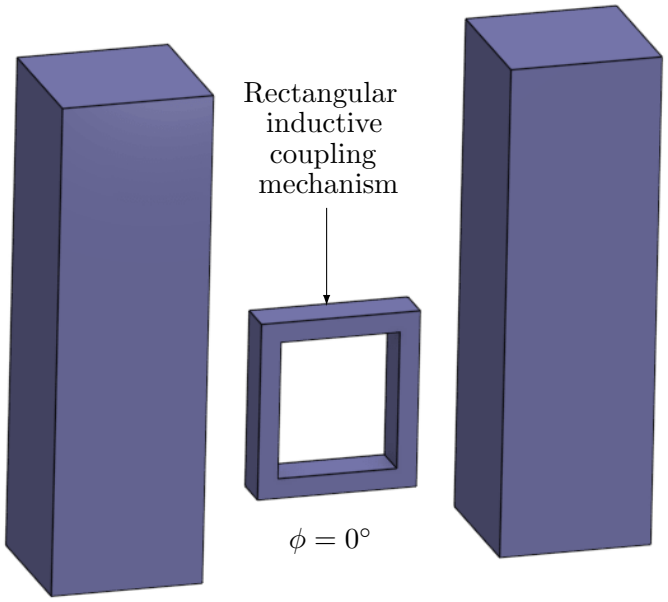

Figure 4.24: A picture of the rectangular inductive coupling mechanism.

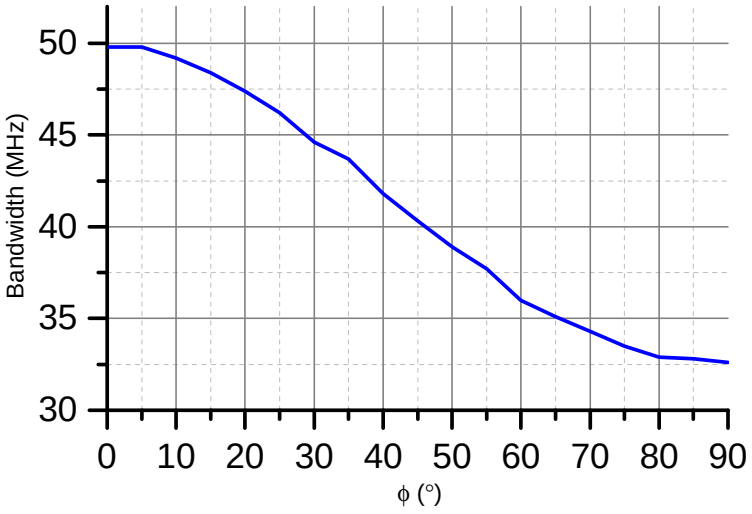

Figure 4.25: Bandwidth for rotation of rectangular inductive coupling mechanism.

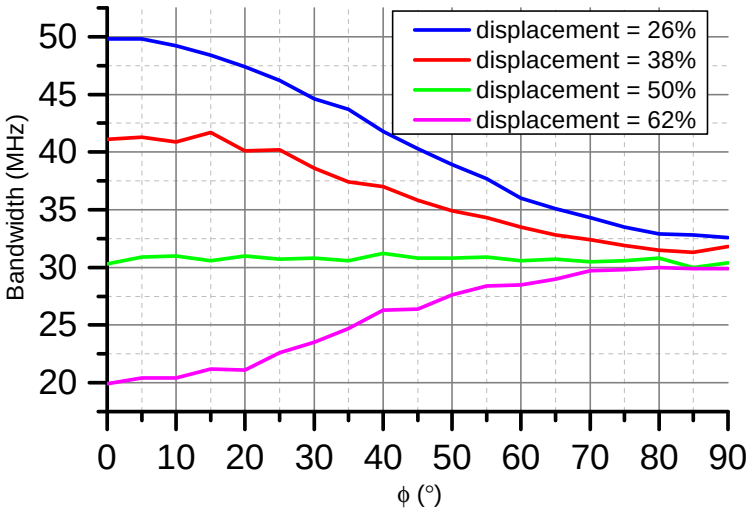

Figure 4.26: Comparison of rectangular coupling mechanisms for different vertical displacements relative to resonator height.

pling is unavoidable in the high E-field region. Therefore this mechanism could be utilised in the same way to exploit different fields depending upon its relative height up the resonator.

Figure 4.26 shows a graph plotting rotation of the rectangular mechanism in four different field configurations through variation of the mechanisms vertical displacement relative to resonator length in increments of 3 mm. Looking in particular at the bandwidths observed at 90degree it can be said that regardless of the height of the mechanism, when the mechanism is at maximum angle, the bandwidth variation is very minor. For all intents and purposes it can be called negligible. It can therefore be inferred that the mechanism at 90° has a negligible impact on the coupling. Following this logic, the bandwidth observed at $\phi = 0$degree when compared to 90° is indicative of the type of coupling being exploited by the mechanism. If the bandwidth at the minimum angle is larger than at maximum angle, then the mechanism is exploiting the H-field and vice-versa for the E-field when the bandwidth is narrower.

When the mechanism is level with half way up the resonators, there is no bandwidth tunability seen. This would indicate that the E- and H-fields are cancelling each other out at this point as would be expected since this is the height which separates the electric- and magnetic-dominant field regions — the neutral region. Displacements below 50% are said to be in the magnetic-dominant region. The two plots on the graph showing the mechanism in the magnetic region both show bandwidths at $\phi = 0°$ larger than for a mechanism in the neutral region. Therefore it can be said that these are inductively tuning the coupling. Whereas for the mechanism at a displacement of 62%, in the electric field region, the starting bandwidth is less than what is seen in the neutral region. Indicative of capacitive tunability.

An interesting side note to point out here is that despite originally setting out to find a mechanism to tune coupling with rotation, a more efficient method has been

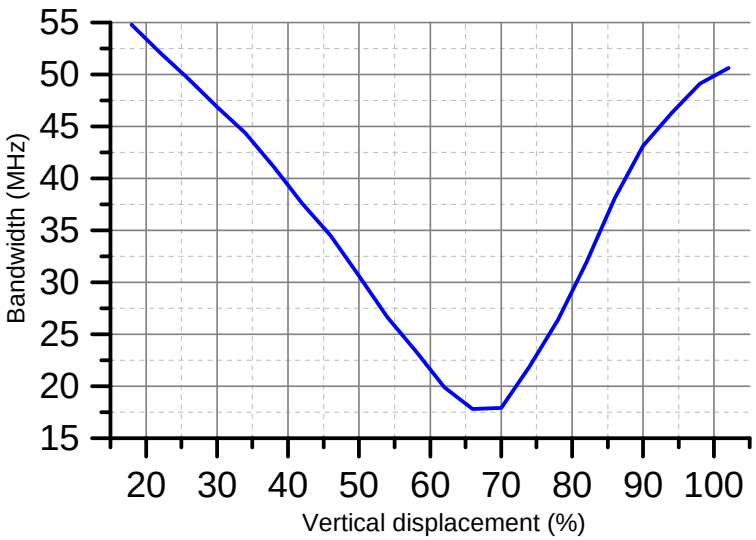

Figure 4.27: Illustration of how bandwidth changes with mechanism displacement height relative to resonator length.

found in the vertical actuation of the mechanism instead. Scrutiny of figure 4.26. A deviation in the bandwidth at $\phi = 0°$ is seen from 20 MHz to 50 MHz (60%). Figure 4.27 shows how the bandwidth changes with relative height displacement from 20 % to 100 %. What is interesting to see is the relatively linear change in bandwidth as the height of the mechanism is swept from 20 % to 60 %. Presumably this is because the mechanism is able to exploit both the electric and magnetic fields equally well and as such is able to smoothly transition between the two dominant regions. It should be noted that the minimum bandwidth here occurs between 65% and 70%, compared to the 80% minimum seen in other plots. This is not an electromagnetic effect of this design compared to others, it is purely a difference in how the mechanism height was measured. In previous relative height displacement plots, the percentage was calculated using the top of the mechanism. Here (and also for figure 4.26) the vertical centre of the mechanism was used, thereby truly reflecting when the mechanism is occupying the neutral region. In fact, if the height was measured using the top of the mechanism, the turning point would again be at 80% as in previous similar tests.

4.3 Review

A thorough understanding of the interaction of electric and magnetic fields between resonators in a combline cavity filter is developed through the testing of various implementations of rotationally asymmetrical components suspended in the coupling gap. Their effect on ripple bandwidth with rotational actuation is observed through the use of three dimensional simulation software. The first group of mechanisms are designed from the viewpoint of exploitation of the electric coupling, ie. capacitive coupling. The second group of mechanisms are designed with the intention to exploit the magnetic coupling fields. It is shown that the inductive mechansims proposed also happened to

Mechanism name	**Acheivable bandwidths** (MHz)	**Tunability** (%)
Wire-separated plates (no iris)	46.5 - 51.5	10%
Wire separated plates (iris)	50.6 - 62.9	24%
Single plate	49.7 - 39.0	-22%
Air separated plates	50.3 - 35.6	-29%
PTFE-separated plates	50.0 - 35.0	-30%
Connected vertical wires	50.1 - 62.7	25%
Rectangular mechanism	49.8 - 32.6	-34%

Table 4.1: A comparison of each rotatable mechanism for bandwidth tunability.

exploit the electric coupling as well. The mechanisms are compared in the table 4.1.

Chapter 5

The Design of Fully Tunable Filters

As was shown in chapter 3, a resonator can be modelled as a shunt LC tank. For a combline filter, this is represented as a length of transmission line which is grounded at one end and loaded with a shunt capacitance at the other. For non-planar filters operating in a cavity, the physical implementation of this given by a circular or rectangular extrusion of a conductor within a cavity as shown in figures 5.1 and 5.2. Of course when dealing with high frequency EM signals, any medium within which they propagate can produce a resonance. Eigenmode simulation can be used to estimate the modes generated within a structure. Table 5.1 shows the resonance of modes 1 to 5 in both cylindrical and rectangular structures depicted in figures 5.1 and 5.2. The dimensions used for the eigenmode simulation are as follows:

$$h_{cav} = 25 \text{ mm}$$
$$r_{cav} = 22.5 \text{ mm}$$
$$w_{cav} = 22.5 \text{ mm}$$
$$t_{cav} = 22.5 \text{ mm}$$
$$h_{res} = 22.5 \text{ mm}$$
$$r_{res} = 4.5 \text{ mm}$$
$$w_{res} = 10 \text{ mm}$$
$$t_{res} = 10 \text{ mm}$$

As table 5.1 shows, the fundamental resonance for both cylindrical and rectangular resonators occurs in the range of 2300 MHz. This is to be expected for a resonator with a physical length of 22.5 mm at an electrical length of 62 °. The first spurious mode, and all subsequent modes, are above 7 GHz. This shows that all evanescent modes generated by the cavity itself are sufficiently out of band for filters designed at around 2 GHz.

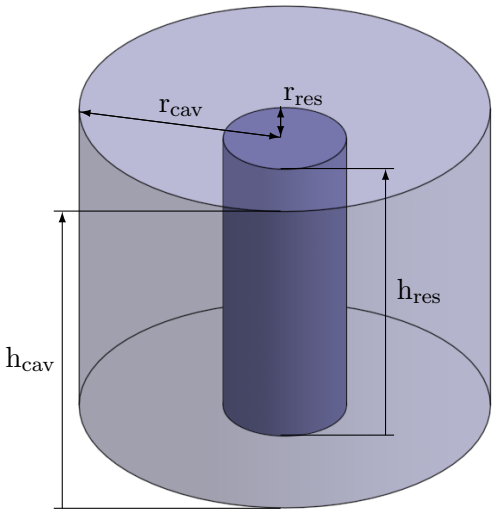

Figure 5.1: A cylindrical resonator and cavity.

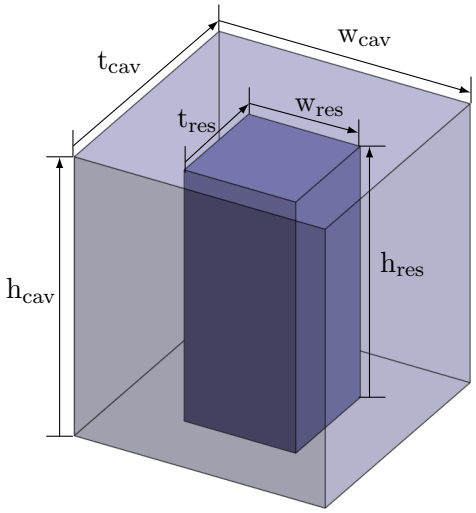

Figure 5.2: A rectangular resonator and cavity.

Mode number	Resonant Frequency (MHz)	
	Cylindrical	Rectangular
1	2244	2325
2	7119	7104
3	7602	7162
4	7610	7252
5	11247	10716

Table 5.1: Frequencies of modes generated in cylindrical and rectangular cavity resonators.

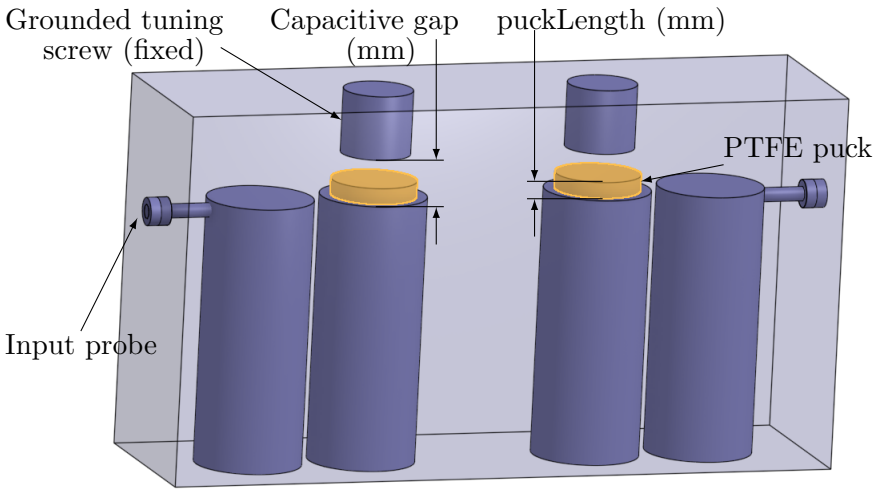

Figure 5.3: Three-dimensional representation of the internals of a second-order filter cavity using a PTFE puck to tune capacitance to ground from the resonators.

5.1 Centre-frequency tunability

5.1.1 Utilisation of Insulators for Resonance Tuning

The principle of operation for a Combline filter utilises loading capacitance to ground at open-circuited ends of transmission lines. These capacitors force the shunt lines to behave as inductive elements causing resonance to occur below the quarter-wavelength frequency. Synchronous tuning of all loading capacitances in a combline filter allows for control of the centre-frequency. Increasing capacitance reduces centre-frequency and since the frequency dependence of the inverters is relatively small over large bandwidths the return loss and bandwidth of a frequency tunable combline will remain relatively constant over a broad tuning range.

Remembering from the previous chapter that capacitance (equation 4.6) is proportional to the dielectric medium between conductors as well as the exposed area of those conductors. Additionally capacitance is inversely proportional to separation distance.

If one was to take a simple two-pole filter, such as the one in figure 5.3, and place dielectric material in the capacitive gap between the each resonator and its fixed grounding screw, one would expect the capacitance to ground to increase by a factor equivalent to the relative dielectric constant of the insulator. In turn this would have a causal effect on the resonance of the individual lines where the frequency at which it occurs would reduce. Furthermore, if the proportion of the gap that the insulator occupies were able to be controlled, by mechanical movement into and out from the capacitive gap for example, specific control of the centre-frequency would be achievable between the two frequencies entirely with and without the insulator present.

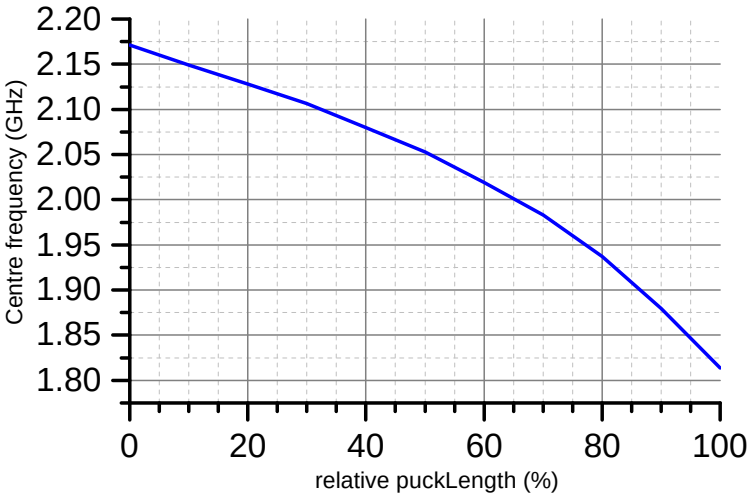

Figure 5.4: A graph showing how the relative length of a PTFE puck from a resonator open end to ground tunes the centre-frequency of a two-pole filter.

Simulation tests were performed on the three-dimensional model illustrated in figure 5.3 for puckLengths up to the size of the capacitive gap. The filter in question was designed (without the dielectric puck) to have a centre frequency above 2.1 GHz and a bandwidth of 50 MHz with a return loss ripple greater than or equal to 15 dB.

Figure 5.4 shows how the operating frequency of a filter is controlled by a PTFE puck occupying a relative proportion of the capacitive gap to ground. PTFE has a relative dielectric constant of $\epsilon_r = 2.1$, therefore, assuming no fringing fields are present, it can be expected that the capacitance would be roughly double compared to when air ($\epsilon_r = 1$) is the sole separating medium. Tunability is shown to be acheived from 2.171 GHz when no dielectric is present, to 1.813 GHz when the gap is entirely filled with PTFE — giving a total tuning range of approximately 360 MHz. The rate of change of centre frequency is approximately between the maximum and minimum points which makes for easy tunability prediction. Despite this, a slightly higher sensitivity is observed as the relative puckLength approaches 100%. It can be assumed that the E-fields from resonator to grounding screw are not uniform straight-line E-fields propagating directly from one to the other since fringing fields will inevitably be present. Therefore a strictly linear change in capacitance with the dielectric puckLength should not be expected.

Improvements in tunability for the design in figure 5.3 would not be difficult to achieve in practice since the tuning range is able to be extended simply through the choice of insulator used. Simulations in this section use PTFE as the dielectric, however materials with a larger constant would yield a proportionally larger tuning range.

Instead, how about applying modifications to the structure of the resonators to see what effect it has on the acheivable tunability? Figure 5.5 shows a filter where the front sections of the resonators have been removed to show the insides. Here the resonators have been designed as hollow cylinders within which a solid cylindrical

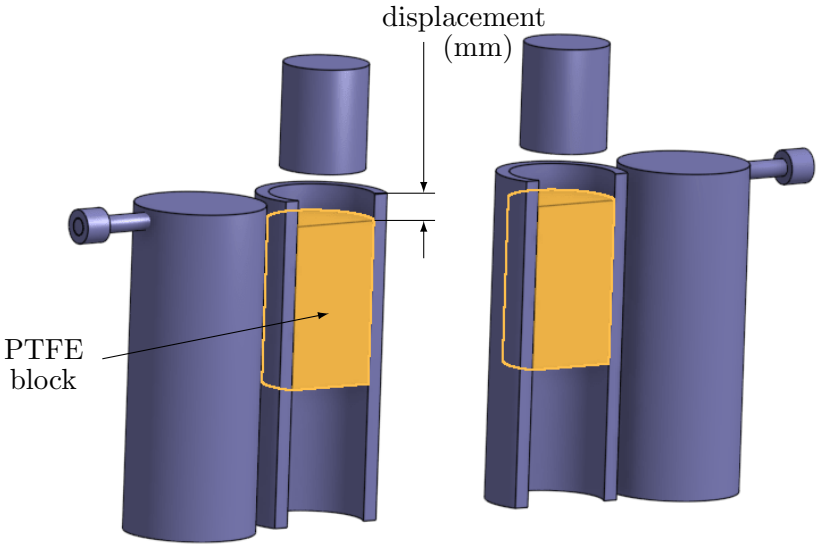

Figure 5.5: A two-pole filter utilising the hollow resonator design with vertically actuated PTFE blocks contained within hollow resonators for frequency tunability.

block of PTFE is contained. The dimensions of the metallic parts in the filter have been kept consistent with the previous design, where the capacitive gap is 1 mm. The dielectric block has the same diameter as before, but now has a fixed length of 12.5 mm.

The principle of operation for this design proceeds as follows. When the block is contained deep within the resonator, it has no effect on its resonance since it is not affecting the electric fields to ground. Linear actuation in a vertical direction causes the block to begin having an effect on the E-fields between the resonator and ground, therefore allowing for resonance tunability to be achieved. Where it improves on the previous design is in the practicality of realisation. The previous design is impossible to replicate exactly without physically changing the dielectric puck with another differing in length. Instead it would have to be approximated by moving a single puck of length 100% into the capacitive gap from the side of the filter — a mechanically laborious, and bulky process that can potentially perturb the operation of other parts in the filter when implemented. With the hollow resonator design, realisation becomes far easier since any mechanical alterations or drivers needed can be housed within the resonator and therefore not affect the operation of the filter.

A simulation test was performed for the hollow resonator design as the insulating block is actuated from deep within the resonator, until the faces of the grounding screw and dielectric meet. The results of this test are shown in figure 5.6. The vertical position of the block is represented as the displacement between the top edges of the block and resonator. Negative values of displacement refer to when the block is below the top of the resonator.

Displacements of less than -1 mm are not shown because when the block is in this position or lower, very little deviation in centre frequency is observed. The vast majority of tuning happens between ± 0.5 mm suggesting that the E-fields to ground are highly

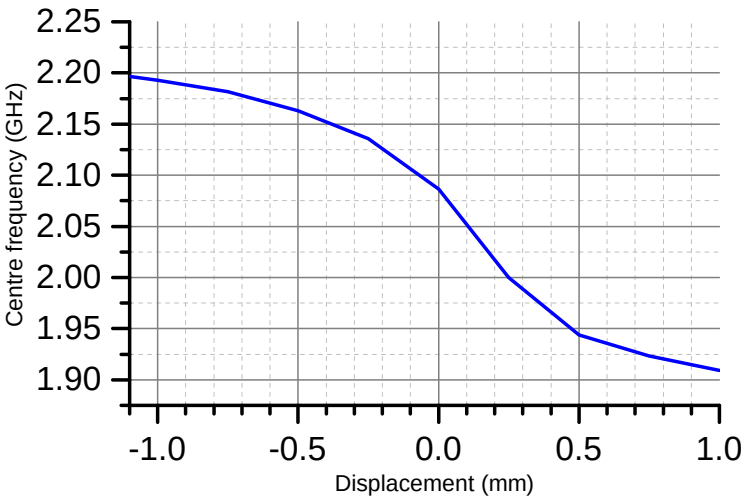

Figure 5.6: The simulated centre-frequency for displacement of a PTFE block from the top of a resonator.

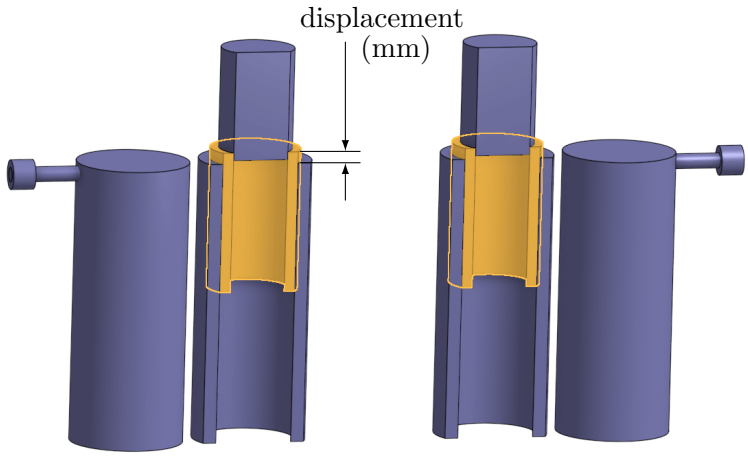

Figure 5.7: The hollow dielectric design — Hollow resonators with hollow PTFE cylinders for frequency tunability.

concentrated at the very tip of the resonators. The previous design is based on the assumption that the fields to ground are uniform. This design is an extension from the previous one in the sense that it overcomes difficulties in realisation. What it has not attempted to improve upon is the non-uniform fringing fields from the outer-sides of the resonator to ground, which can potentially be exploited to exhibit a larger tuning range.

Looking back at the first design in figure 5.3, it would be expected that simply increasing the diameter of the puck would eventually capture most of the E-fields to ground, however this would be extremely impractical. Not to mention providing diminishing returns in limited space once the diameter becomes significantly larger than that of the resonator. Instead, if the PTFE cylinder were to be designed as a hollow cylinder, such that it could both fit inside the hollow resonator and fit around the grounding screw (figure 5.7), the maximum amount of E-fields would be 'captured and therefore allowing for the maximum amount of capacitance to ground and therefore frequency

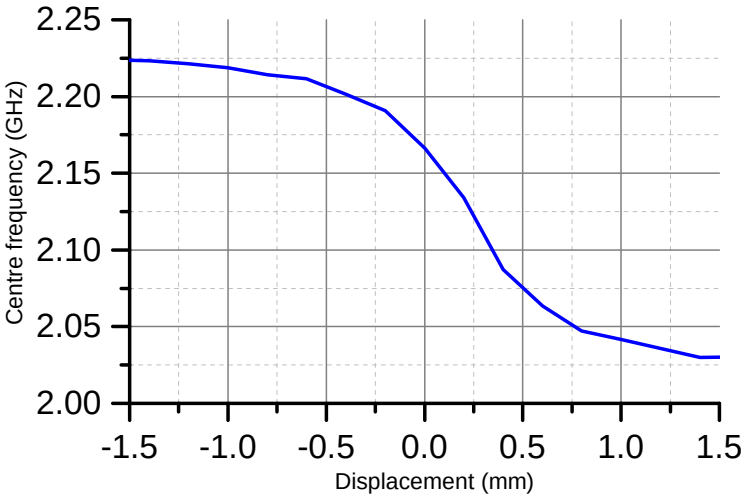

Figure 5.8: A graph of centre frequency for hollow dielectric cylinder displacement from the structure shown in figure 5.7.

tunability to be acheived.

The hollow dielectric design just described is not limited by the grounding screw and therefore has a much larger range of movement than that of previous designs. The results for simulations of centre frequency against displacement are shown in figure 5.8 for displacements between ± 1.5 mm. The general shape of the graph is congruent with figure 5.6. Upon closer inspection it is evident that the rate of change in frequency with displacement is greatest at roughly 0.25 mm. In the previous design this was closer to 0 mm. Therefore the hollow dielectric is showing signs of utilising the fringing fields to ground. The drawback to this design however, is the thickness of the dielectric. Evidently the dielectric 'sleeve is catching the E-fields, however since it is relatively thin, the E-fields are still mostly in air and therefore the capacitance to ground caused by the dielectric is small. This is shown by the smaller tuning range observed. For the hollow resonator design, the tuning range was slightly more than 280 MHz from 1.909 GHz to 2.192 GHz. Here with the hollow dielectric design however, a tuning range of only 180 MHz from 2.041 GHz to 2.219 GHz. It should be noted that the tuning range measured in both cases was taken between ± 1.0 mm for a fair comparison. The hollow dielectric design shows a tunability performance of about two-thirds that of the hollow resonator design. One could be forgiven for dismissing the hollow dielectric design based upon this statistic, however when it is given in the context that the thickness of the 'sleeve' is only 0.75 mm, compared to a radius of 4 mm for the dielectric in the hollow resonator design, it becomes apparent that the additional capturing of the E-fields is having an effect on the centre-frequency. Therefore a hybrid of the two designs, as shown in figure 5.9, could combine the benefits of both and acheive greater tunability.

The combined effects of both the capturing of additional fringing fields and the thickness dielectric is shown clearly by the two distinct sections of the graph in figure 5.10. The change in centre frequency with displacement here shows two periods of acceler-

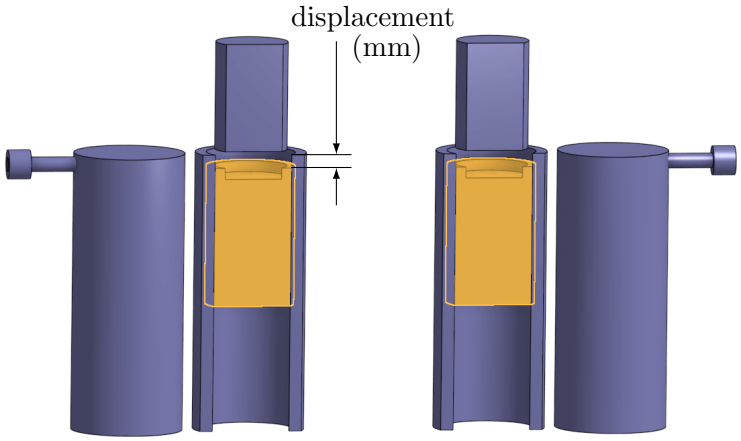

Figure 5.9: Three-dimensional representation of a frequency tunable filter using a PTFE block with a cut-out section.

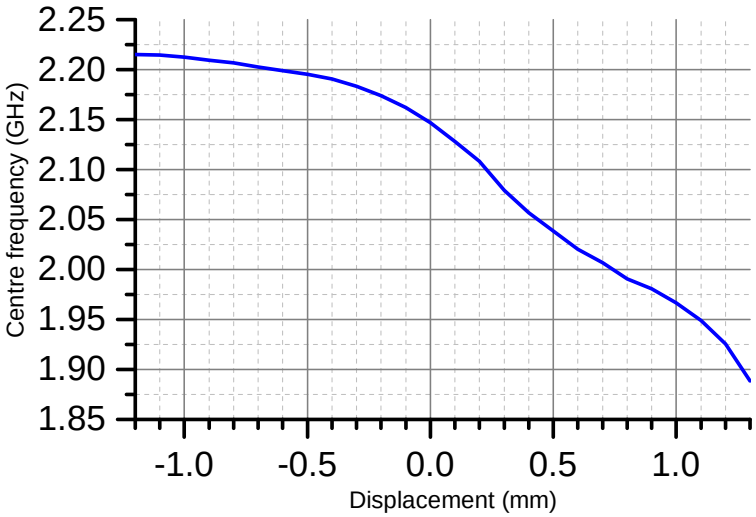

Figure 5.10: Centre-frequency for displacement of cut-out PTFE block.

ated tunability. The first from about −0.5 mm to 0.4 mm and the second from 0.7 mm to 1.3 mm. At 1.3 mm the dielectric lies flush against the grounding screw, and its 1 mm sleeves encapsulate the lower portion of the screw. The total tunability of this design implementation is 327 MHz from 1.888 GHz to 2.215 GHz — almost 50 MHz more tunability than was shown by the hollow resonator design.

5.1.2 Utilisation of Metal-Air-Metal Capacitance for Resonance Tuning

Thus far frequency tunability has been performed using the dielectric characteristics of insulating materials. One of the main benefits of using a dielectric over a conductor is that an insulator will show no ill effects when in close proximity to a conductor. For example, the dielectric centre-frequency tuning designs described in this work are able to sit flush against resonators and grounding screws since they do not directly allow current to flow through them. Conductors on the other hand would be prone to

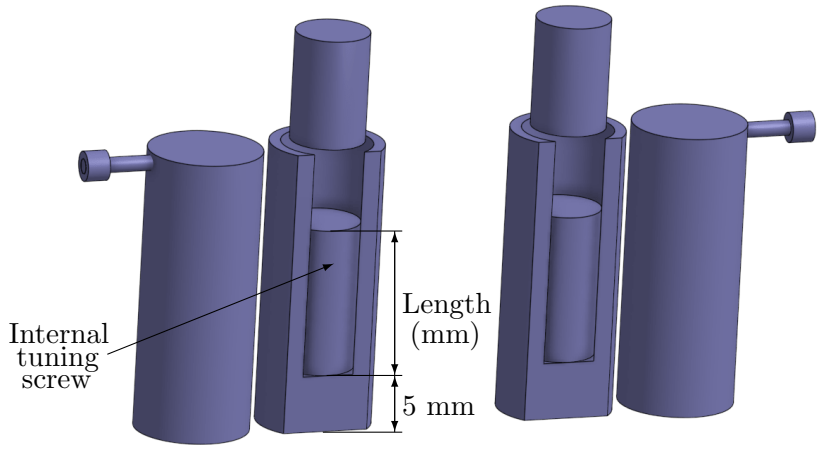

Figure 5.11: Illustration of hollow resonators with internal metallic tuning screws.

shorting or arcing for higher-power systems. Insulators are inadequate for frequency tunability however, in systems where a very high Q is required. This is due to the losses associated with the specific material used — usually through heat dissipation and dipole relaxation. Dielectric losses are typically defined for a given material using the dielectric loss tangent ($\tan\delta$) where δ is defined as the angle between the capacitors complex impedance vector and the negative reactive axis in the impedance plane. For situations where a high-Q is required, metal-air-metal capacitances are more desirable due to the near-zero loss tangent of air.

The designs proposed for dielectric tunability introduced a number of hollow resonator designs which afford the convenience of easy accessibility to the tuning mechanism when moving forward to the fabrication and realisation stages of the design. Expanding the previously hypothesised designs to accommodate metallic tuning presents a filter illustrated in figure 5.11. Here the resonators have a hollow cavity cut from the top until 5 mm from the bottom. From the remaining section at the base of the resonator, a cylindrical metallic screw of arbitrary length extends upwards. Connecting the internal screw to the base of the resonator ensures a path to ground. Similar to the hollow resonator design with the PTFE block, for small lengths of the internal tuning screw there is little-to-no effect on the resonant frequency. For lengths of the screw where its top face approaches a similar height to the top of the resonator, the internal tuning screw begins to act as a part of the resonator. Increasing the length further, the internal screw creates a capacitance to ground through the fixed grounding screw and as a consequence the resonant frequency reduces. This capacitance to ground is controlled via the proximity of the internal screw to the grounding screw i.e. an exploitation of d from equation 4.6.

The performance of the metal-air-metal tuning for an internal tuning screw is shown by the graph in figure 5.12. Given the length of a resonator is 25 mm, when the internal screw length is 20 mm its top face is level with that of the resonator. Also given that the fixed grounding screw is positioned 0.3 mm above the top of the resonator at the

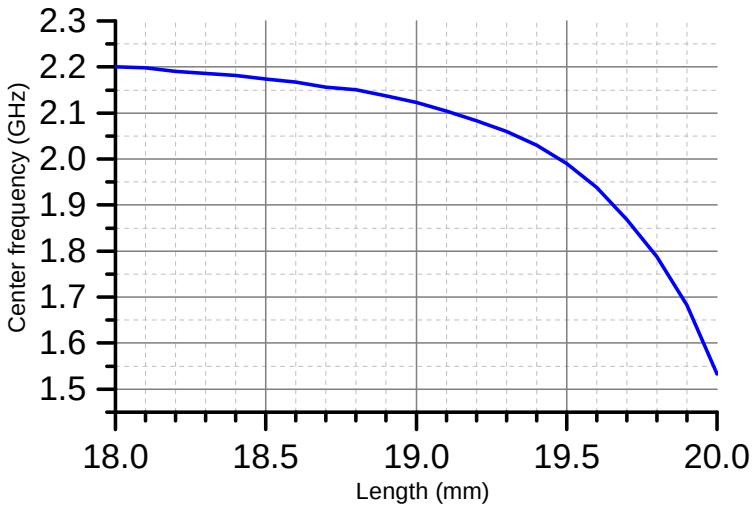

Figure 5.12: Centre-frequency for internal tuning screw length.

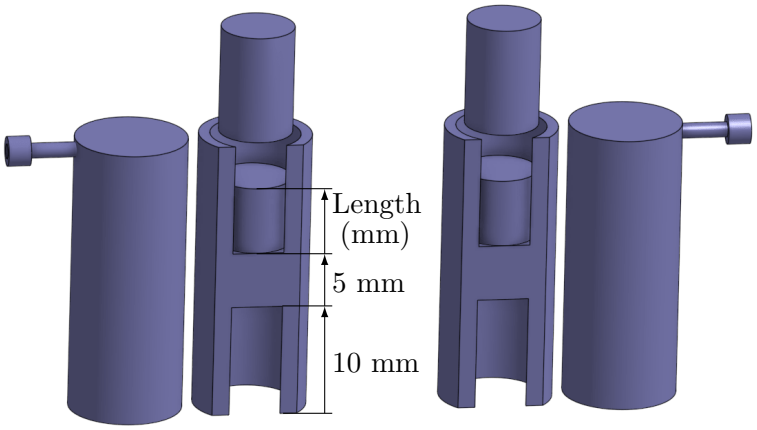

Figure 5.13: A filter implementing raised internal tuning screws.

maximum length displayed in the graph, the separation distance between the internal and grounding screws is 0.3 mm.

Starting from 2.2 GHz, as the length is increased beyond 18 mm, the centre frequency is shown to fall to below 1.6 mm, or a tuning range of over 500 MHz over 2 mm of actuation — nearly double the tunability achieved by the best insulator-tuned filter. Theoretically since the internal tuning screw can be treated as part of the resonator, the point at which it connects the connection is made could be placed almost anywhere along the line, so long as it is not in a region the capacitance to ground is affected. Figure 5.13 provides a visual representation of raising the connecting section 10 mm up the resonator. For this filter, if the section connecting the screw to the resonator is indeed not causing the capacitance to ground to be affected, then the centre frequency should change at the same rate over the same range of movement. Obviously a given length in this design should be equivalent to the same length +10 mm for the previous design. Figure 5.14 shows the simulation results for a screw connected internal to the resonator at a height of 10 mm. It is congruent, almost exactly with the graph in figure

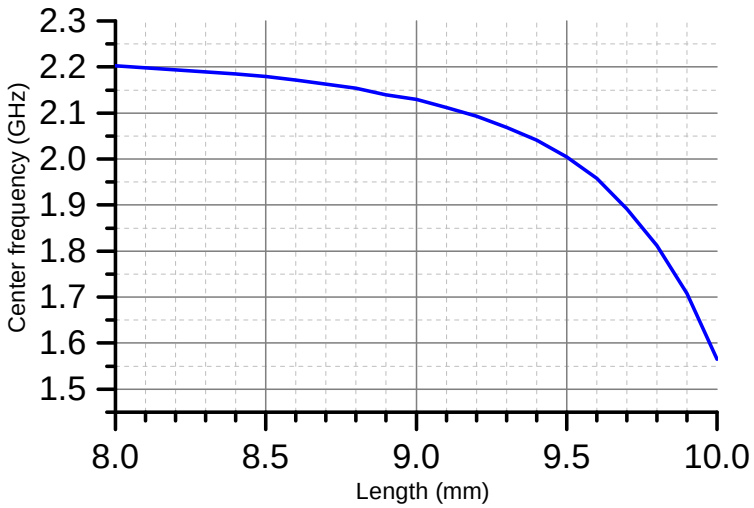

Figure 5.14: Centre-frequency tuning range for the raised internal screw.

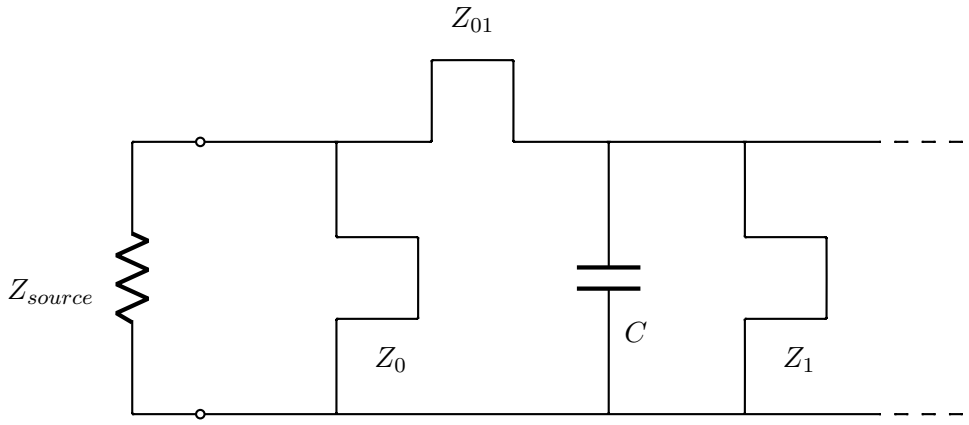

Figure 5.15: Equivalent circuit of Combline filter at the input.

5.12. Tunability from 2.2 GHz to 1.6 GHz is achieved, confirming that there is negligible difference as to where the connection of the screw to the resonator occurs.

5.2 External-coupling tunability

The equivalent circuit of the input transformer and first resonator of a Combline filter is shown in figure 5.15. This is what constitutes the external coupling, Q_e. This is what matches the filter to the network on the source and load. It can be reduced to three distinct stages. The first is the input connector and feed line, this is the point at which the physical connection to the external network occurs. The second stage is the impedance transforming elements at the input of the filter, represented here by the short-circuit stub, Z_0. The third stage is the coupling between the transformer and first resonator which is typically determined by the input spacing in a conventional cavity filter.

Figure 5.16 shows a representation of a typical Combline cavity filter. When optimis-

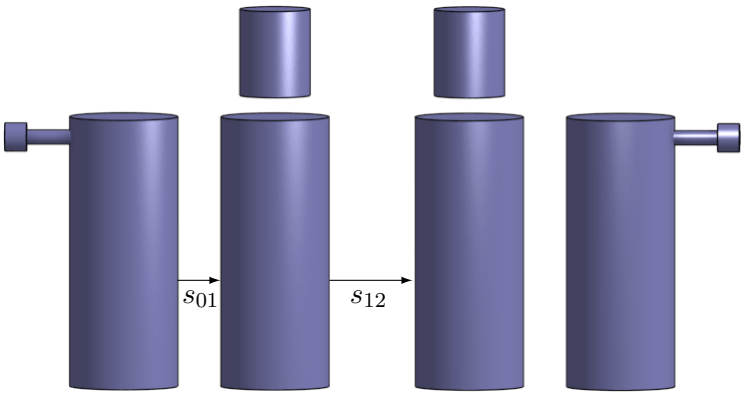

Figure 5.16: A side view of the internal elements of a typical two-pole cavity filter.

ing a design to meet specifications, the resonator spacing, s_{12}, is adjusted to set the bandwidth and the input spacing, s_{01}, is modified for the desired return loss performance. Due to the co-dependence of these couplings, this procedure usually requires a few iterations to exactly match the desired response. Inspection of figure 5.17 illustrates how the bandwidth changes with return loss ripple level in a two-pole filter when providing alterations to either of the couplings. For the experiment, a filter was set up in a simulation model to have a passband return loss of 15 dB and a bandwidth of 50 MHz as is shown by the intersection of the two graphs. Tuning of each spacing independently shows a similar range of return loss. This is convenient for comparing the relative effects that tuning of either the inter-resonator coupling or external coupling can provide. Their co-dependence is clearly shown here since both methods are able to adequately modify both the ripple level and bandwidth of the response. What is clear though is that the inter-resonator coupling has a greater effect on the bandwidth than the external coupling for a similar range of ripple levels.

Comparing the change in bandwidth from 10 dB to 32.5 dB, tuning of the resonator coupling shows a range of 30 MHz whereas the external coupling only affects the bandwidth by 15 MHz. Another point of note, which is not illustrated in this graph is that where the bandwidth increases with the resonator spacing, it decreases with input spacing — which suggests that any method of tunability would have the opposite effect on the bandwidth to a similar method of tunability applied to the inter-resonator coupling. For example where the addition of capacitance between resonators, explored in the previous chapter, is known to reduce the bandwidth. Should a similar process be applied between the transformer and first resonator, it would be expected to increase the bandwidth instead.

As was mentioned earlier, there are three stages to the external coupling — pre-transformer, post-transformer and the transformer itself. This section aims to explore methods of tunability for the external coupling in each of these stages to compare their effectiveness for implementation in a filter.

Figure 5.18 introduces the first design for the pre-transformer external coupling stage. Here a circular disk is utilised to provide capacitance between the input feed line

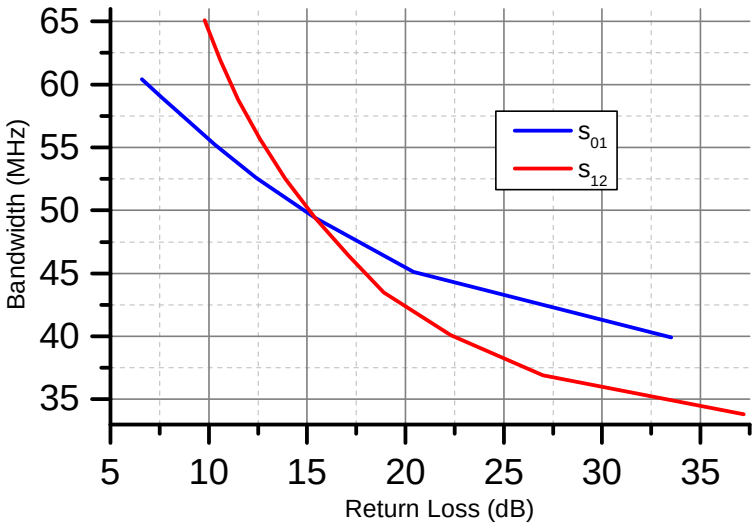

Figure 5.17: A comparison of return loss to bandwidth when tuning input- and inter-resonator-spacings.

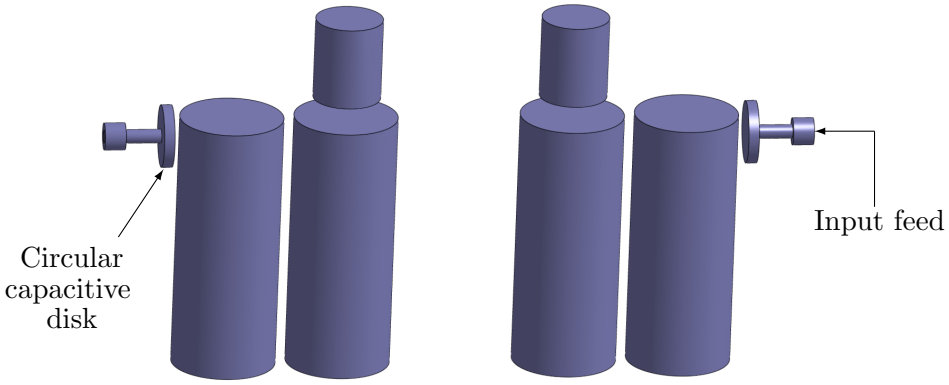

Figure 5.18: A two-pole filter with capacitive input coupling disks.

and the transformer. This creates a capacitance from the connector at the input to the impedance transforming element. As has been well established by now, the capacitance can be controlled by plate area, separation distance or permittivity of separating medium.

Figure 5.19 shows how the bandwidth and return loss ripple change with the radius of the capacitive disk. The return loss is shown to have a range from close to zero up to 35 dB which results in a total bandwidth variation from 35 MHz to 58 MHz. Already this is comparable to the amount of tunability seen for the changing input spacing. It is worth remembering that the area of the disk is proportional to the square of the radius. Therefore doubling the radius from 1.6 mm to 3.2 mm will quadruple the capacitance.

This design has two drawbacks preventing it from being a viable option for external coupling tunability. The first is the difficulty of realisability. It is very challenging to come up with a realisable design that would allow for the radius of a disk at the end of a connector to be selectively controlled. Shape-memory alloys (SMA, also

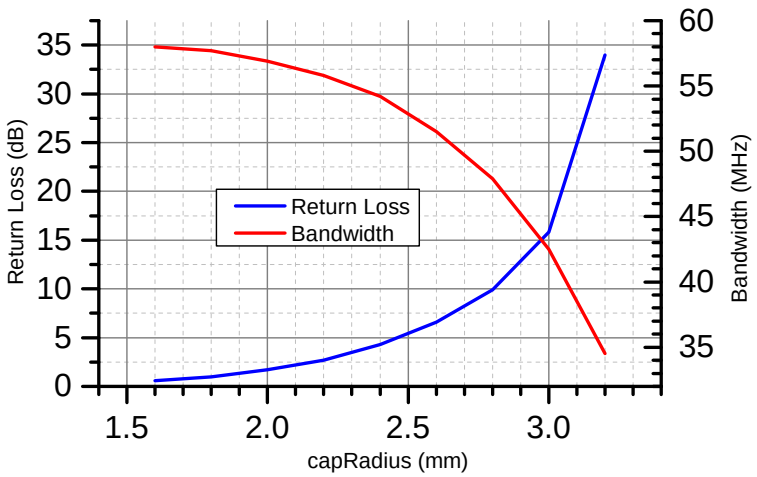

Figure 5.19: Simulated return loss (L) and bandwidth (R) for a given radius of the capacitive input disk.

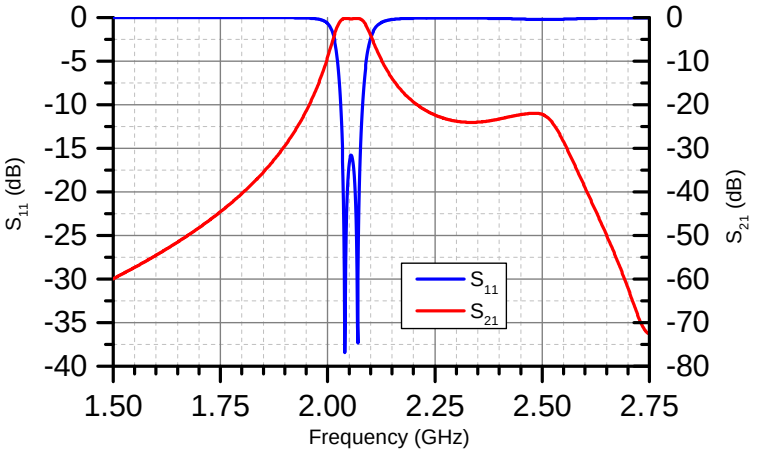

Figure 5.20: The simulated response of a two-pole filter implementing the capacitive input disk.

known as memory metals) could potentially be exploited to control the area of the capacitive probe. These are alloys which assume pre-determined shapes based upon their temperature. This would mean that the filter cavity would be required to be temperature controlled to avoid any unintended actuation. Unfortunately the number of cycles a memory metal can undergo before losing shape is limited. In addition SMAs suffer from hysteresis depending on whether they are in the process of heating or cooling [59]. The second issue with the capacitive disk design is illustrated in figure 5.20. A perturbation is seen in the insertion loss response of the filter with a capacitive input at 2.5 GHz. This would suggest an additional resonance is taking place within the filter.

Thinking back to the Combline circuit model, this capacitive input design is the equivalent of having capacitors in series with the input coupling. Since the stubs act as inductors at frequencies lower than the quarter wave frequency, a series LC (or band-pass) circuit is formed in the coupling. When the capacitive coupling is added to a

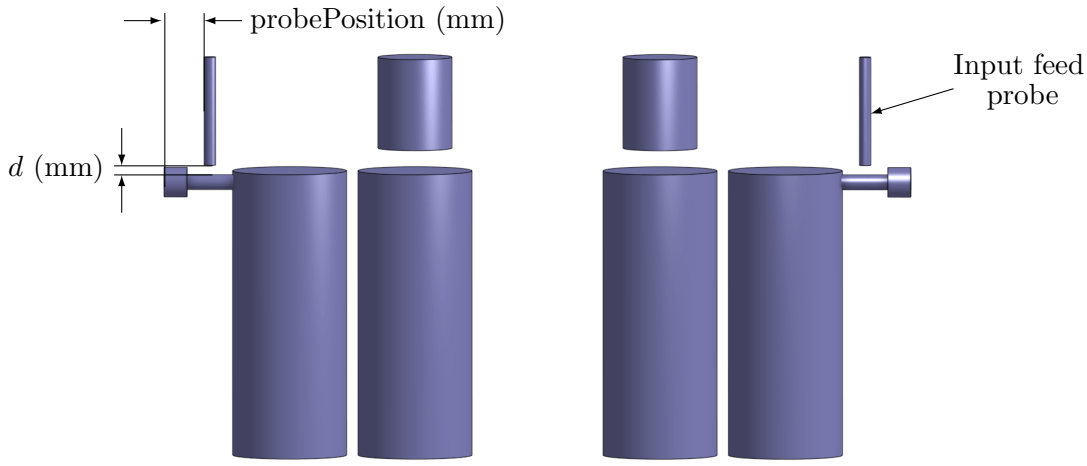

Figure 5.21: Three-dimensional representation of a filter implementing tuning screws over the input feed lines.

design in a circuit model simulator such as Microwave Office, the third resonance (at 2.5 GHz) can be recreated showing that it is an unavoidable by-product of the input capacitance.

Figure 5.21 shows the second design for exploiting the pre-transformer stage of the external coupling. It is a relatively simple concept that utilises probes from the cavity lid to create a capacitance between the input feed and ground. Actuation in a vertical direction i.e. increasing or decreasing d, should alter this capacitance resulting in a change in Q_e.

The change in bandwidth and return loss with actuation is shown in figure 5.22. Here the bandwidth ranges from 46 MHz to 50 MHz, which corresponds to return loss tunability from 15 dB to 19 dB over an actuation range of 5 mm. This is a moderately small amount of tunability which would struggle to match the desired return loss of a filter back to the required specification. On the input feed line, the relative field strength is quite small when compared to somewhere like a resonator simply because at resonance standing waves are formed in the resonators, which maximises the field strength at the resonator ends. Since no modes form on the input feed, the field strength, and therefore the capacitance available between the feed line and probe, is very small. This is why only a limited tunability is achievable here.

Figure 5.23 shows a plot of how the external coupling tunes for a given position of the probe. This graph gives an idea of where the field strength is strongest along the input feed line. Knowing from figure 5.22 that as the capacitance to ground increases, the return loss increases — the maximum field strength will be observed where the return loss is largest. This is seen when probePosition = 11 mm, which incidently happens to be when the probe is close to the middle of the transformer implying that the best tunability with a feed line probe method would ideally be performed over the transformer itself. This is not an uncommon method for post-production optimisation of Q_e, therefore the key points learned from figure 5.23 only help to

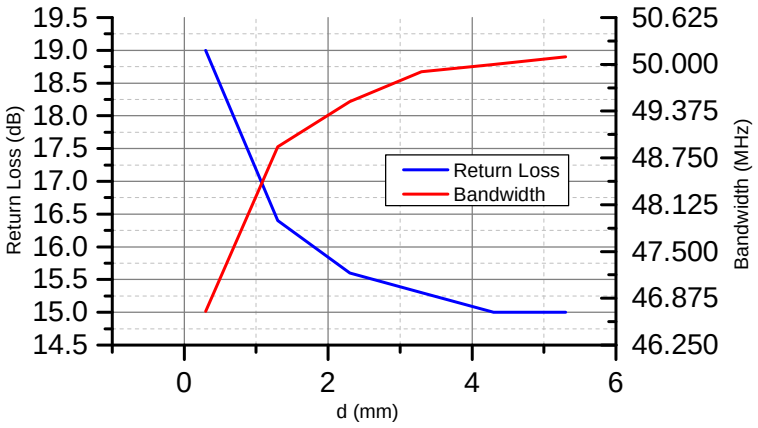

Figure 5.22: Simulated return loss and bandwidth for probe distance, d above input feed line.

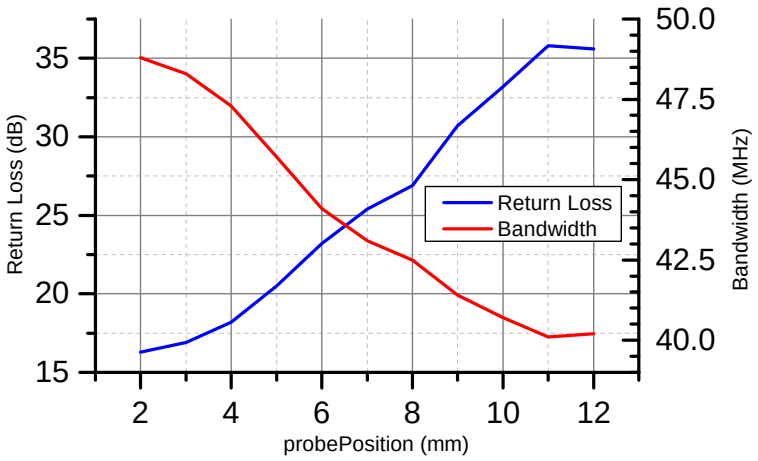

Figure 5.23: Simulation of return loss and bandwidth for horizontal displacement from the side of the filter.

confirm the methodology of standard practice.

To continue from the design in figure 5.21, which utilises a screw from above the input feed line, it would seem sensible for the sake of completeness to see how a screw from beneath the feed line performs. This design is illustrated in figure 5.24. Here a tuning screw is extended from the base of the filter until it is in close proximity with the input connector feed. There two possible effects that the screw coming from the base could have. The first is similar to the previous design where a capacitance is formed between the input feed and ground via the screw, which wouldnt be expected to have much effect on the external coupling. The second effect is due to the proximity of a screw close to the transformer. This could affect how the transformer performs by coupling energy from the transformer to ground in a similar way to a tuning screw mounted above the transformer would.

The graph in figure 5.25 shows a simulated measure of the change in external coupling for a given length of a feed line tuning screw from the base of the filter. The screw was modelled for lengths from 2 mm to 23 mm. The lowest section of the feed line is at a

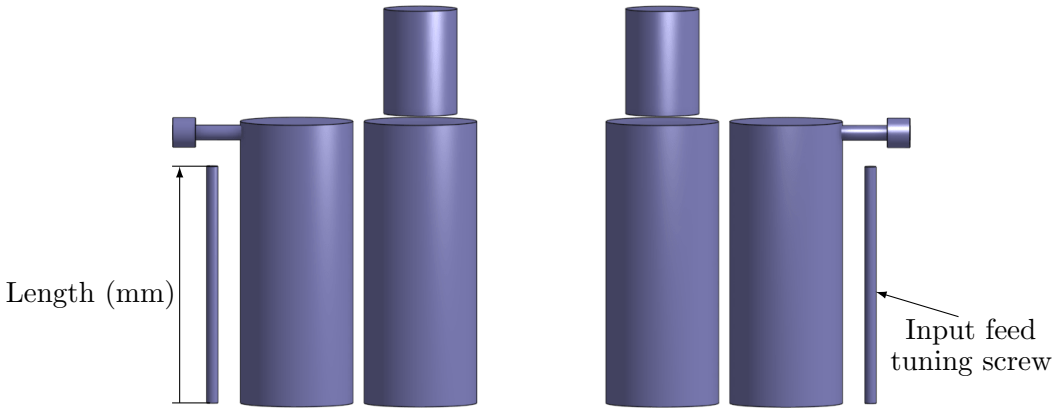

Figure 5.24: Tuning screws from underneath the input feed lines.

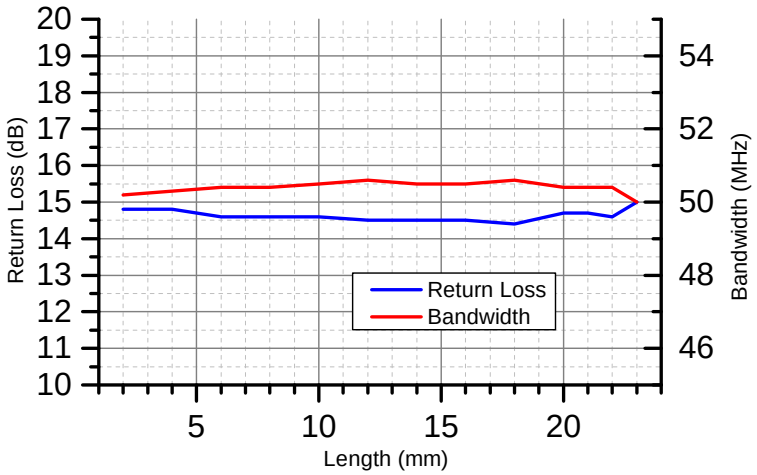

Figure 5.25: Return loss and bandwidth simulations for input feed tuning screws from beneath.

height of 23.4 mm therefore the screw is 0.4 mm from the feed line at its closest. The graph clearly shows that a screw in this position has very little effect on the response of the filter. The maximum swing in bandwidth is only 0.6 MHz. Similarly the maximum and minimum return loss seen are 15.0 dB and 14.4 dB respectively. This method of tuning for the external coupling is shown to be ineffective. It therefore warrants no further investigation.

The second stage of the external coupling with potential for exploitation is the transformer itself. It has already been shown with the probePosition simulations in figure 5.23 that a transformer is best tuned capacitively to ground from above close to its cross-sectional centre. Therefore since a typical filter already implements a screw above the transformer to provide post-production optimisation, a method similar to the raised internal tuning screw technique suggested for resonance tuning in figure 5.13 would be a potential method worth exploration for its ability to affect the external coupling. An illustration of this method is provided in figure 5.27.

The concept of external coupling tunability provided by a screw mounted internally

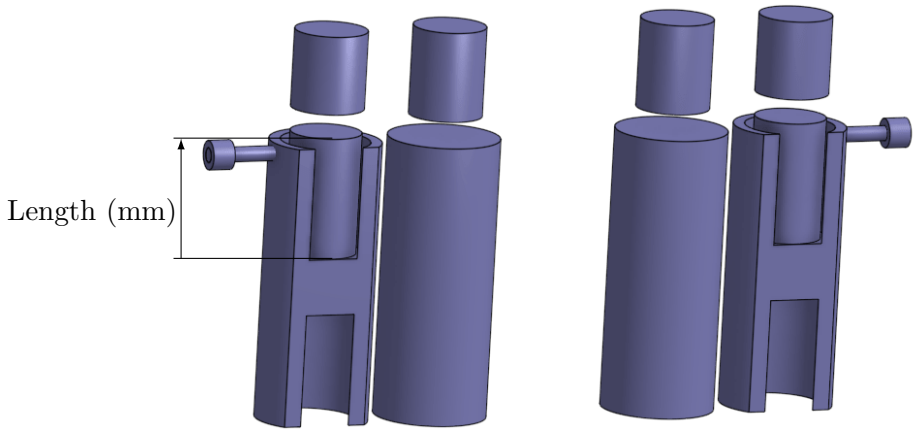

Figure 5.26: Filter internals with raised internal transformer tuning screw.

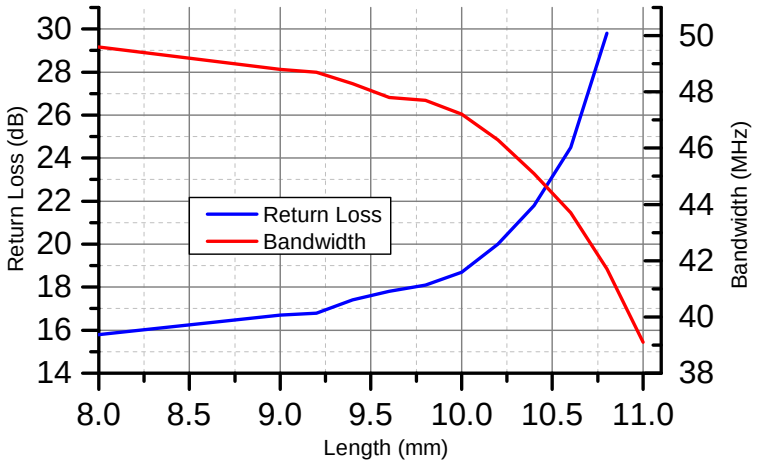

Figure 5.27: Simulation of external coupling versus transformer tuning screw length.

to the transformer is exactly the same as with the method for resonance tuning. It has been shown through simulations thus far that Q_e can be tuned by altering a transformers capacitance to ground — in fact a transformer is essentially a resonator that resonates above the passband. Therefore it is logical to assume it can be tuned using the same method for resonance tuning.

Figure 5.27 illustrates graphically how the external coupling tunes when a screw mounted internally to the transformer is actuated in a vertical direction. Over a range of about 2.5 mm the return loss is shown to tune from about 16 dB to 30 dB, which corresponds to bandwidths from 49 MHz to 39 MHz repectively. As with the resonance tuning, since the internal screw can be actuated to positions where its gap to the grounding screw is very small, technically any capacitance value upwards of the nominal value (when its length value is small) can be achieved at the expense of increasing sensitivity with capacitance. Therefore any bandwidth lower (or return loss higher) than the nominal value is potentially achievable.

Exploitation of the third stage of the external coupling, the input spacing region, can be difficult due to the strong coupling required between transformer and first resonator.

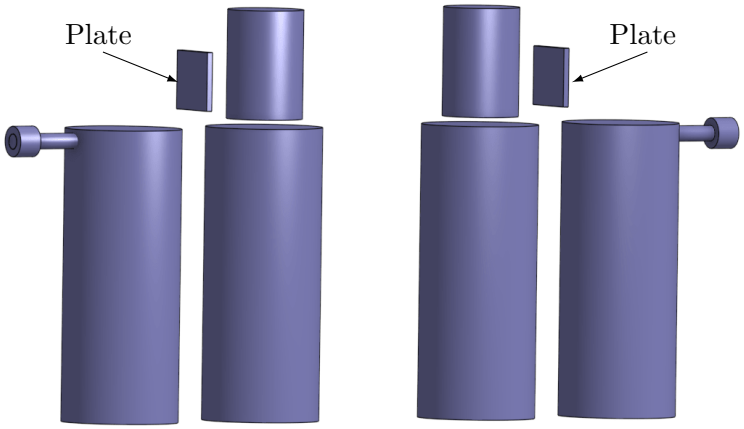

Figure 5.28: Square plates providing capacitance between transformers and resonators.

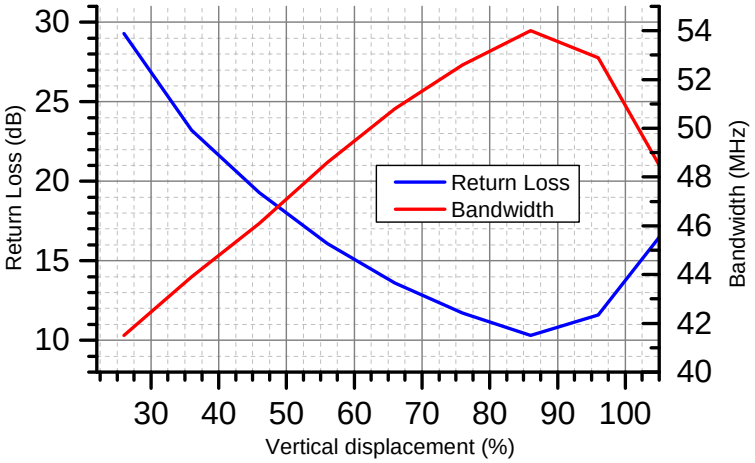

Figure 5.29: Simulated measure of external-coupling tunability using a plate between transformer and first resonator for a given vertical displacement relative to the resonator length.

Therefore the input spacing can often be quite small, sometimes around 3 mm or less. Nonetheless, to recall the work carried out on the inter-resonator couplings in the previous chapter. It was found that a vertically actuating plate in the coupling region can exploit both the electric and magnetic couplings in different phases of the actuation process to either increase or decrease the bandwidth of a filter. One could assume with plausibility that the input coupling could be controlled in a similar way.

Due to the narrow spacing between the resonator and transformer, a rotating plate would not be able to exploit its effective plate area well enough since the capacitance to the plate would be heavily d dominant. Besides, the rotation angle range would not be particularly large before shorting between the two lines occurs. Therefore a vertically actuating plate such as the one described in figure 5.28 provides the best solution for tunability in this stage.

Figure 5.29 shows the tunability afforded by the vertically actuated plate in the input spacing. It was shown earlier that the coupling across the input spacing works inversely to the resonator spacing — in other words, where a capacitance in the resonator spacing

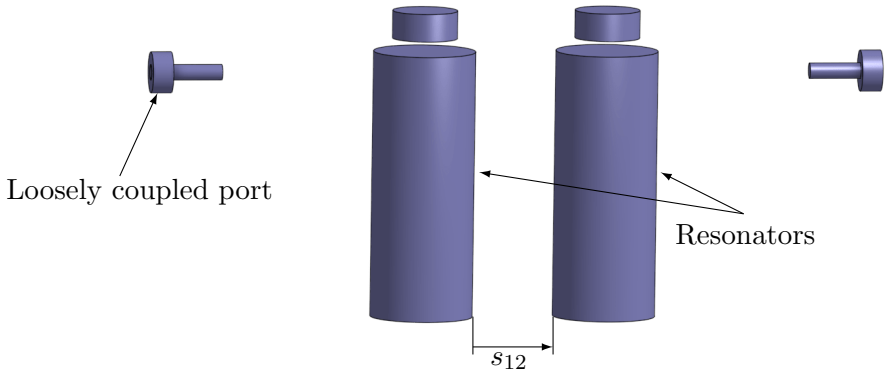

Figure 5.30: Simulation model of two coupled resonators with loosely coupled input and output ports.

reduces the bandwidth, a capacitance introduced to the input spacing will increase the bandwidth. It is known from the experiments performed on inter-resonator coupling that the capacitance of a plate introduced between two resonators occurs at roughly 80% of the resonator height. Here the maximum capacitance is observed at about 83%, which is shown as a peak in the filter bandwidth confirming that a capacitance between the input transformer and first resonator does indeed increase the bandwidth.

The range of bandwidths achievable for the height actuated plate is 12 MHz from 42 MHz to 54 MHz. This corresponds to a return loss ripple level of 10 dB to 29 dB. This method provides marginally more tunability than the capacitance to ground method, however the range of achievable bandwidths seen here corresponds to the maximum range achievable with this technique, whereas the raised Q_e tuning screw technique has a larger tuning potential.

5.3 Modelling of inter-resonator and external-couplings

Up until now, quantification of couplings has been performed via simulation testing of complete filter networks. The effects of tuning either external, or inter resonator couplings have been observed through their effect of the overall filter response — namely the bandwidth. There are however, methods described in [60] that can allow for estimations of coupling bandwidths to be calculated experimentally. Firstly, take for example the network illustrated in figure 5.30. Here two metallic resonators, separated by s_{12} mm, are enclosed within a cavity and loosely coupled to the input and output ports. Since the resonators are identical, they resonate at a frequency, f_0. Displacement of the resonances, Δf is observed in the insertion loss response (figure 5.31) as a direct effect of the coupling between the resonators. This is known as the coupling bandwidth and can be used to determine the achievable ripple bandwidth (BW) range of a filter at a frequency of f_0 through the following formula:

$$BW = \frac{\Delta f}{M_{12}} \tag{5.1}$$

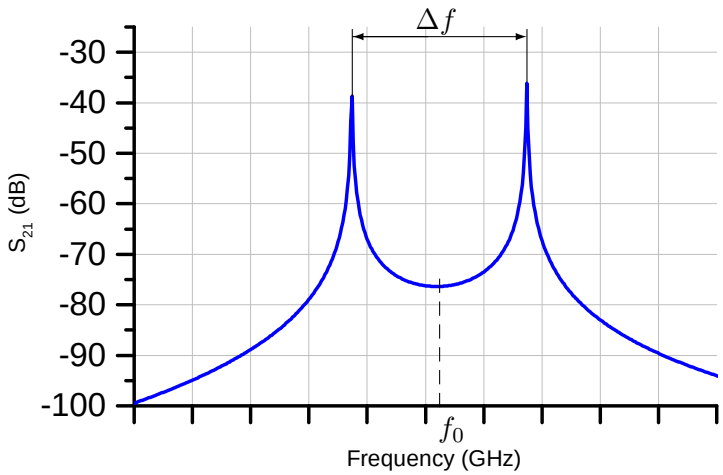

Figure 5.31: Transmission characteristic of a pair of coupled resonators.

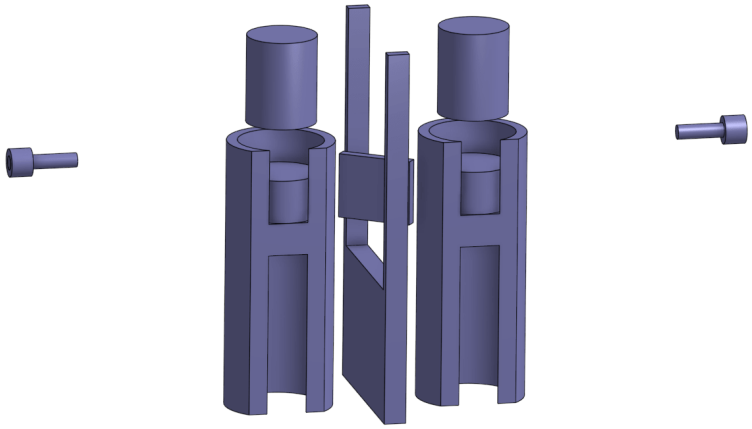

Figure 5.32: Simulation setup for tunable inter resonator coupling bandwidth test.

Where M_{12} is the normalised coupling coefficient between the first and second resonators and can be extracted from the coupling matrix [61].

Figure 5.32 shows a circuit consisting of two tunable resonators implementing the rotating plate method for tunability of the inter resonator coupling. This tuning method was chosen because it was one of the best performing implementations of coupling tunability in the tests performed. Furthermore, since the actuation required for tuning the coupling is rotational, it is relatively simple method to realise. Multiple sweeps of the plate rotation angle from $\phi = 0°$ to $90°$, were performed for different values of inter resonator spacing, s_{12} at 2 GHz. The results are shown in figure 5.33.

Where the spacings are comparable to the width of the plate ($w = 7$ mm), the couplings are shown to become very sensitive as ϕ approaches $90°$. This is a result of the plate edges being in close proximity to the resonators and hence a very large capacitance across the coupling is achieved resulting in the bandwidth rapidly tending towards zero. A filter with a small resonator spacing like this would prove to be too sensitive to ambient vibrations and other environmental disturbances in the vicinity of the filter to be practical. Conversely for resonator spacings larger than about 9.5 mm the

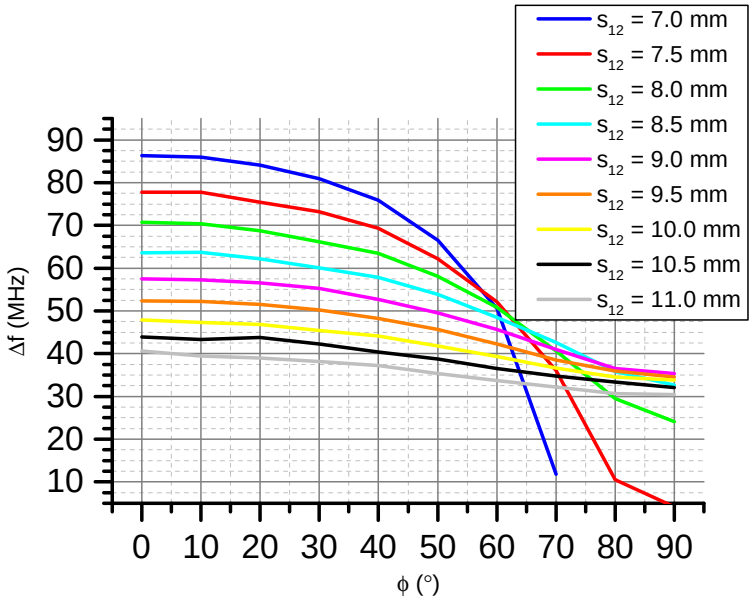

Figure 5.33: Simulated inter-resonator coupling bandwidths for given resonators spacing and plate rotation angle.

gap between resonators is large enough that the capacitive tunability achieved when rotating the plate is insignificant. Therefore very little effect is seen on the coupling.

A similar technique can be employed in order to estimate the external coupling. Figure 5.34 shows a structure designed for the simulation of the input coupling. Here the input port is connected to a transformer which is then coupled into the first resonator. A second 'sniffer port is then loosely coupled to the output of the filter in order to not load the circuit under test. The external coupling is given by the 3 dB bandwidth of the resonance characteristic, which is shown in figure 5.35 as $\Delta f_{3\mathrm{dB}}$. The sniffer port is said to be negligibly loading the circuit when the peak of the resonance curve is below 30 dB. When this requirement is met, the external coupling can be calculated using the following formula:

$$Q_e = \frac{f_0}{\Delta f_{3\mathrm{dB}}} \tag{5.2}$$

It is assumed in this case that the unloaded Q (Q_u) is much larger than the loaded Q (Q_L), therefore the identity $Q_e = Q_L$ applies, since [62]

$$\frac{1}{Q_L} = \frac{1}{Q_e} + \frac{1}{Q_u} \tag{5.3}$$

As with inter resonator coupling, the achievable ripple bandwidth of a filter can also be expressed in terms of the normalised coupling coefficient and Q_e:

$$BW = \frac{f_0}{M_{01} Q_e} \tag{5.4}$$

Figure 5.36 shows the setup for testing the range of achievable external coupling band-

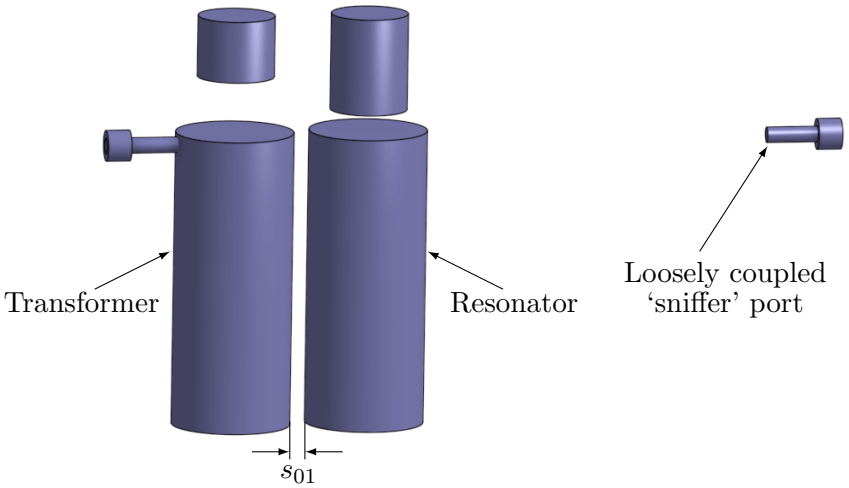

Figure 5.34: General simulation model for the estimation of external coupling bandwidths.

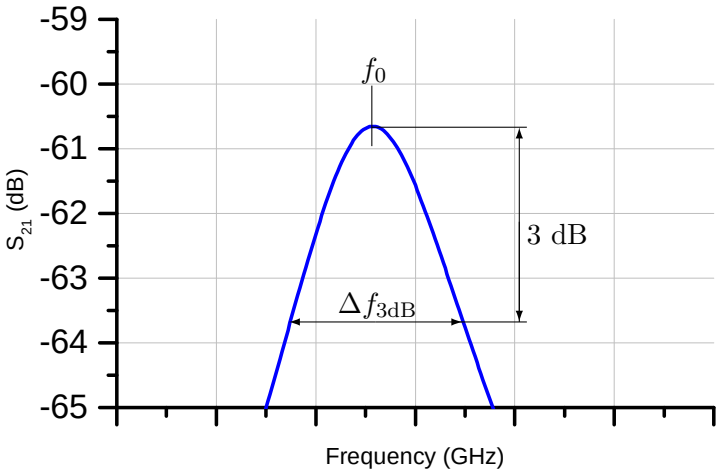

Figure 5.35: Associated external coupling characteristic.

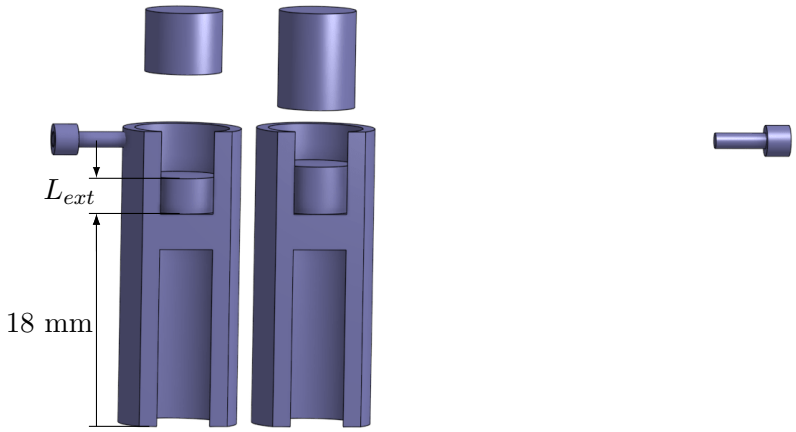

Figure 5.36: Simulation model setup for the estimation of external coupling tunability.

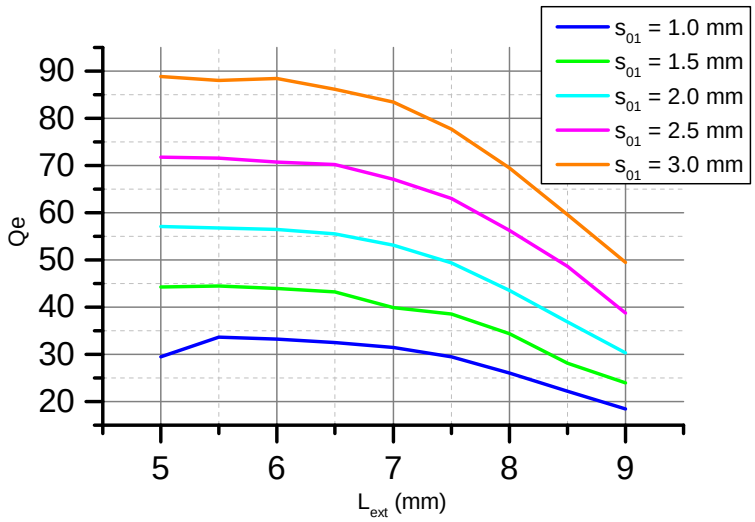

Figure 5.37: Estimated Q_e tuning range for different input spacings.

widths for given input spacings (s_{01}). This model is of the type described in the previous section with the raised internal tuning screw. Minor modification were performed — the L_{ext} screw is now at a height of 18 mm from the base of the transformer (or 7 mm from the top). This is to limit the redundant range of L_{ext}. Results of the test can be seen in figure 5.37. Here it is shown that the external coupling bandwidth range is heavily determined by the choice of s_{01}. This shows that were a filter to implement the tunable inter resonator and external coupling techniques tested here, the range of tunability would be limited by the external coupling.

5.4 Two-pole prototype design

A combination of inter-resonator coupling, external coupling and resonance tuning mechanisms allows for the formation of a fully tunable filter. Careful consideration of the implementation of the each mechanism affords precise control over the centre-frequency, bandwidth and return loss. In order to test a basic combination of all mech-

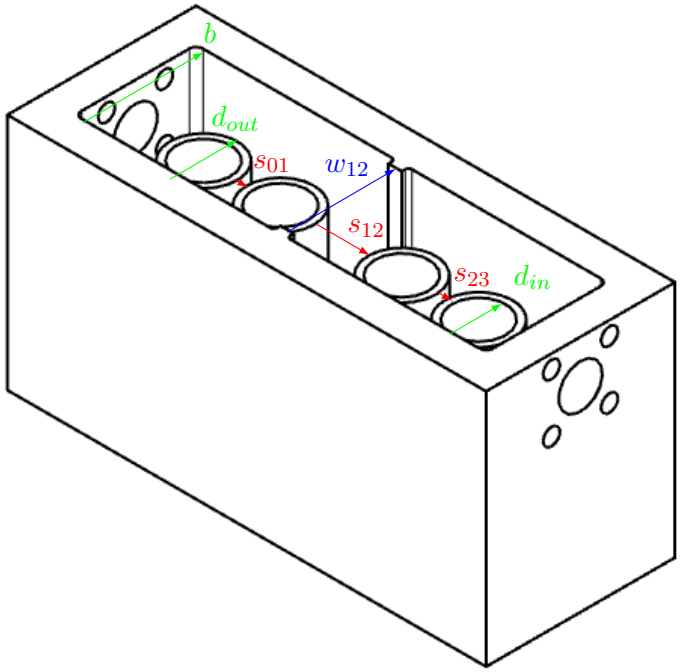

Figure 5.38: Basic setup of the fully tunable two-pole prototype filter.

anisms, a second order combline cavity filter will be designed using the raised internal screw technique for both resonance and external Q tuning, and the single rotating plate method for tunable coupling capacitance. Each of these methods were chosen based on two properties — tunability performance, and feasibility of realisation.

Combination of the data gathered from previous sections shows that a filter with the following specifications can be designed.

$$f_c = 1.75{-}2 \text{ GHz}$$
$$BW = 40{-}60 \text{ MHz}$$
$$RL \geq 10 \text{ dB}$$

Remembering figure 5.12, centre-frequency tunability with the raised internal tuning screw within a hollow resonator is shown to be from 1.6 GHz to 2.2 GHz (27%). Sensitivity however increases greatly as the frequency reduces — with three-quarters of the tuning range occurring in the final quarter of the actuation range. A conservative estimate of the tunability would be to take use of this tuning range (about 13% overall tunability). Applying this to a maximum frequency of 2 GHz and rounded to the nearest 50 MHz gives a lower bound frequency specification of 1.75 GHz.

The required coupling bandwidths can be calculated via the coupling matrix which is independent of frequency. Essentially only the filter order, bandwidth and return loss ripple level are needed for calculation of the couplings, which for the specifications listed above gives coupling bandwidth values for the desired tunability specification

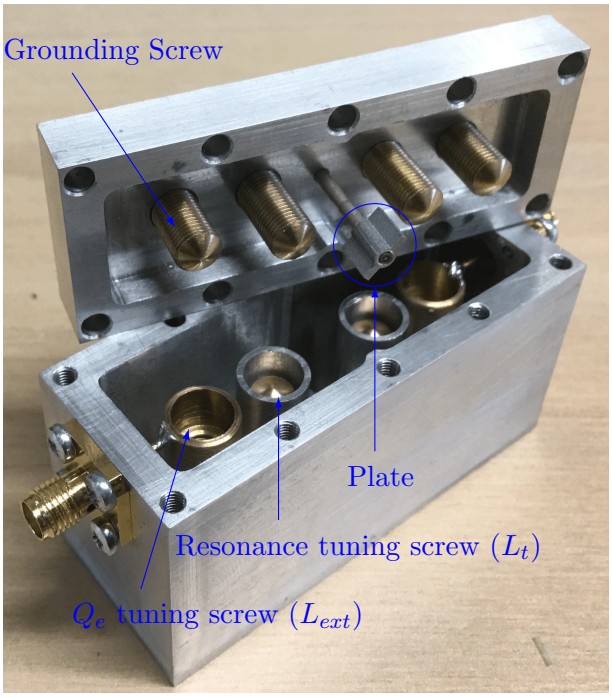

Figure 5.39: Photograph showing the fabricated fully tunable second order prototype filter

of:

$$Q_e = 34.4{-}51.5 \text{ MHz}$$
$$M_{12} = 40.8{-}61.2 \text{ MHz}$$

Therefore the external couplings require bandwidths from 34.4 MHz to 51.5 MHz and the inter-resonator couplings from 40.8 MHz to 61.2 MHz. From this, the input and inter-resonator spacings (s_{01} and s_{12} respectively) can be selected through looking the corresponding tunabilities in the graphs of figures 5.33 and 5.37. Additionally, it should be noted that the inter-resonator spacings can be increased or decreased at will during the design optimisation stages for the same range in couplings by modifying the size of the iris. This can be useful when the plate comes close to contacting the resonators since an increase in the iris means that the spacing must also be increased in order to maintain the coupling.

The structure of the filter is shown in figure 5.38. The corresponding dimensions of the filter are provided below:

$$s_{01} = s_{23} = 1.4 \text{ mm}$$
$$s_{12} = 8 \text{ mm}$$
$$w_{12} = 16 \text{ mm}$$
$$d_{out} = 10 \text{ mm}$$
$$d_{in} = 8 \text{ mm}$$
$$b = 18 \text{ mm}$$

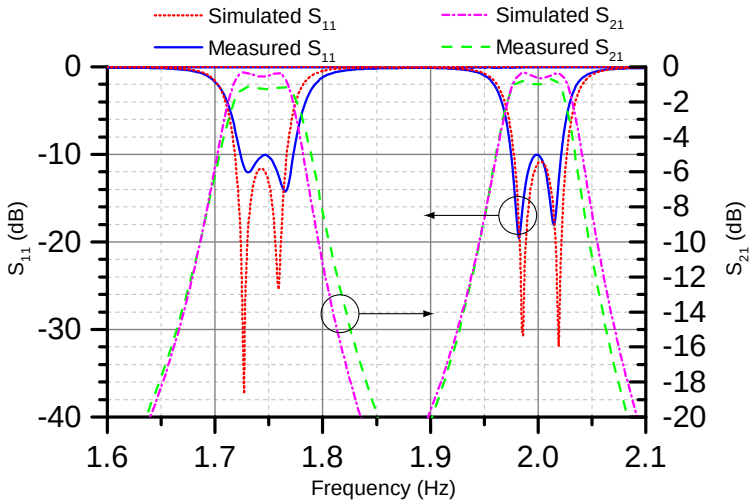

(a) Narrow bandwidth responses

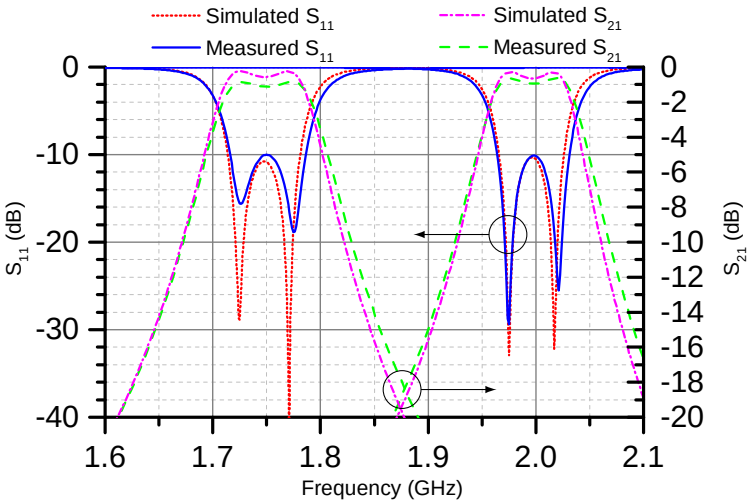

(b) Wide bandwidth responses

Figure 5.40: A comparison of simulated to measured responses for a fully tunable two-pole prototype filter at centre-frequencies of 1.75 GHz and 2 GHz overlayed on the same axes.

Where w_{ij} is the iris width between the ith and jth resonators, d_{out} and d_{in} correspond to the outer and inner diameters for each of the resonators and transformers, and b refers to the ground plane spacing.

A photograph of the fabricated design is shown in figure 5.39. The three tuning mechanisms — Q_e and resonance tuning screws and inter-resonator plate have been highlighted. The grounding screws are also shown in this figure. These are quarter-inch diameter brass screws which are secured by locking nuts on the outside of the filter, to assure a good connection to ground and therefore retain a high Q.

Prior to fabrication, the filter was optimised in HFSS. Knowing the available tunability afforded by the three tuning techniques, the filter was designed at its highest frequency specification, where the L_t tuning screws are positioned outside of the range

of actuation in which the tunability occurs. Similarly, for the external coupling tuning screws, L_{ext}, when they are in their lowest position, the return loss ripple level is at its minimum. From this position, as L_{ext} is increased, the ripple level increases, and the bandwidth narrows. For the rotating plate mechanism, since an increase in bandwidth causes a reduction in the ripple level, the filter should be designed at its narrowest bandwidth. Therefore as the bandwidth is increased through plate rotation, the ripple level can be restored through tuning of L_{ext}.

A comparison of the S-parameter simulation and measurement results is shown in figure 5.40. (a) shows the narrow bandwidth responses, and (b) the wider bandwidth responses for both centre frequencies overlayed on the same axes in each case. The prototype filter was designed with tunability specifications of 1.75 GHz to 2 GHz frequency tuning and bandwidth tuning of 40 MHz to 60 MHz across the frequency range. At a frequency of 1.751 MHz the bandwidth is tunable from 49 MHz to 70 MHz. Similarly at a frequency of 1.998 GHz bandwidth tunability from 41 MHz to 67 MHz is achieved. Although not strictly what the design specifications asked for, bandwidth tunability is shown to be more Fthan required while maintaining the return loss over the range. Passband insertion loss is kept beneath 1.2 dB in every case.

It is clear that the simulation and measurement results are in close agreement with each other — showing that the fabricated prototype does indeed perform as intended. In fact the realised filter proved easier to tune in the laboratory than the simulated filter. HFSS simulation dimensions are limited to quantised lengths of a tenth of a millimetre. The fabricated filter on the other hand is not limited by discrete tuning ranges, since tuning screw lengths and plate angles can be modified in an analogue fashion. Evidence of this is seen for the return loss ripple levels, which for the case of the simulations roughly approximate 10 dB, whereas the realised filter is able to approximate the specified ripple much more closely.

The biggest difference between the simulated and measured results is seen with the in-band insertion loss which in every case is a slightly worse than the simulations. This is due to minor defects, impurities and discontinuities in the fabricated elements which were not accounted for in the simulations. In addition the fabrication process works within a tolerance, which can introduce small discrepancies between the computer model and real-world filter, therefore more energy is dissipated in the filter and a smaller insertion loss is observed. That said however, the insertion loss was kept beneath 1 dB in the majority of cases, which is only 0.5 dB worse than the ideal, lossless case for a 10 dB ripple.

5.5 Fifth order fully tunable filter

The success of the second order prototype filter shows that a basic combination of all three tuning methods in one filter can be designed to a specification with a degree

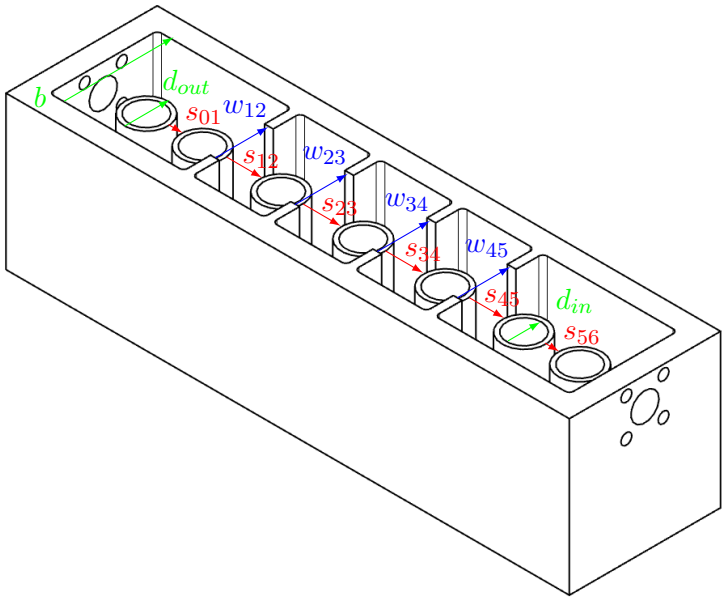

Figure 5.41: Configuration of fifth order design

of accuracy. Scaling the filter up to a higher order would show that the design can cope with a higher complexity due to the increased number of couplings required. For ease of design, since the calculated couplings can be reused, the centre frequency and bandwidth specifications are kept the same as before. The ripple level will instead be designed at 15 dB:

$$f_c = 1.75{-}2 \text{ GHz}$$
$$BW = 40{-}60 \text{ MHz}$$
$$RL \geq 15 \text{ dB}$$

Which corresponds to the following bandwidth denormalised couplings:

$$Q_e = 36.0{-}54.0 \text{ MHz}$$
$$M_{12} = M_{45} = 30.9{-}46.4 \text{ MHz}$$
$$M_{23} = M_{34} = 23.9{-}35.9 \text{ MHz}$$

Following the same processes as for the two-pole prototype, the dimensions of the filter were estimated using coupling bandwidths before optimising dimentions through the use of EM field solving software. Figure 5.41 shows the structure used in for the design where the dimensions are shown in table 5.2.

One of the benefits for the raised internal screw mechanism for f_c and Q_e tunability is that it allows for a cavity to be designed within the resonators. This cavity can be utilised in order to house a motor providing the actuation within the external filter cavity dimensions. Thereby affording the opportunity to add tunability to a filter design without affecting the overall volume — and since filter volume has direct effect on cost, the added tuning functionality without the burden of a higher cost can be

Parameter name	**Symbol**	**Value** (mm)
Resonator spacing (0-1)	s_{01}	3
Resonator spacing (1-2)	s_{12} $(= s_{45})$	8.2
Resonator spacing (2-3)	s_{23} $(= s_{34})$	9
Iris width (1-2)	w_{12}	12.8
Iris width (2-3)	w_{23} $(= w_{34})$	12
Iris width (4-5)	w_{45}	12.4
Plate width	w	7
Plate height	h	6
Plate thickness	t	1
Resonator outer diameter	d_{out}	10
Resonator inner diameter	d_{in}	8
Ground plane spacing	b	25

Table 5.2: Filter dimensions relating to figure 5.41

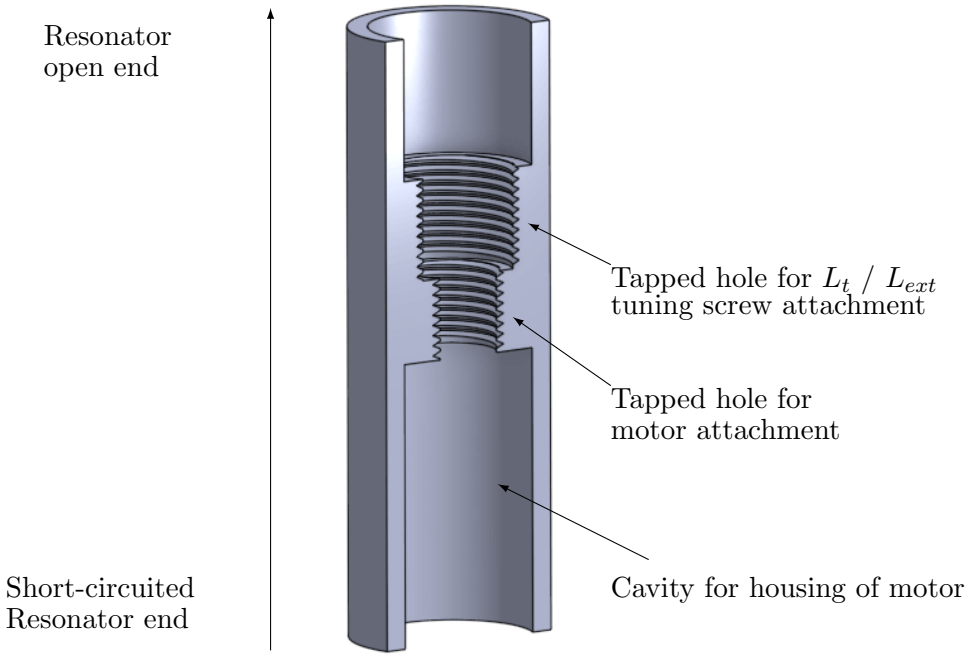

Figure 5.42: Physical design shape of resonators (and transformers) with the front section removed

very appealing to a manufacturer. Faulhaber provide a stepper motor with diameter and length of 6 mm and 9 mm respectively. [63]. This motor has the useful addition of a screw thread at the front end which allows for it to be locked in place. Designing the resonators such that they take the form of figure 5.42 allows for the direct attachment of the motors within the internal cavity. They in-turn can provide the actuation necessary for the tuning of the centre frequency and external couplings.

Figure 5.43 shows photographs of the fabricated filter and the stepper motor. This filter followed the same fabrication process as with the two-pole prototype filter. The only difference being the layout of the resonators, where tapped holes were used to secure the motors inside.

The measured S-parameter results are shown in figure 5.44. Centre frequency tunability is observed from 1.764 GHz to 2.015 GHz and bandwidth tuning ranges of 61 MHz to 89 MHz and 41 MHz to 69 MHz for the lower and upper centre frequencies respectively. The in-band insertion loss is typically observed close to 1 dB and the worst midband losses are measured at 1.4 dB.

When estimating the coupling bandwidths, it was stated that the limitation to the tunability of a filter implementing these three tuning methods is the external coupling tuning mechanism. This is observed in figure 5.44(b) in the lower frequency plot. Here the filter is clearly able to achieve the wide band response, albeit at the expense of a slightly lower return loss than specified — 11.3 dB. Remembering that when the coupling is tuned to increase the bandwidth, the return loss drops. The external coupling is then tuned to restore the return loss to the desired level. In the low frequency, wide bandwidth case of the graph, the external coupling is shown not to be able to restore the ripple to 15 dB. It can be said that Q_e is indeed the bottleneck in the overall tunability performance of a fully tunable filter of this type.

A bandwidth tunability of 50% is still observed at both frequencies. This fits with the original specifications. The issue of Q_e tunability could be overcome by modifying the filter structure so that the lid has less of a cavity inside it. This would result in the resonator and transformer ends being closer to ground, and therefore the grounding screws attached to the lid would not need to be as long as is currently required.

5.6 Review

This chapter has explored external coupling and resonant frequency tuning methods. Tunable capacitance was utilised in both cases. Centre frequency tunability was performed by controlling the loading capacitance to ground. Techniques using dielectric insulators as well as metal-air-metal were thoroughly explored.

For the case of a combline cavity filter, the external coupling was viewed as having three stages at which tunable capacitance can potentially provide tuning to the external Q

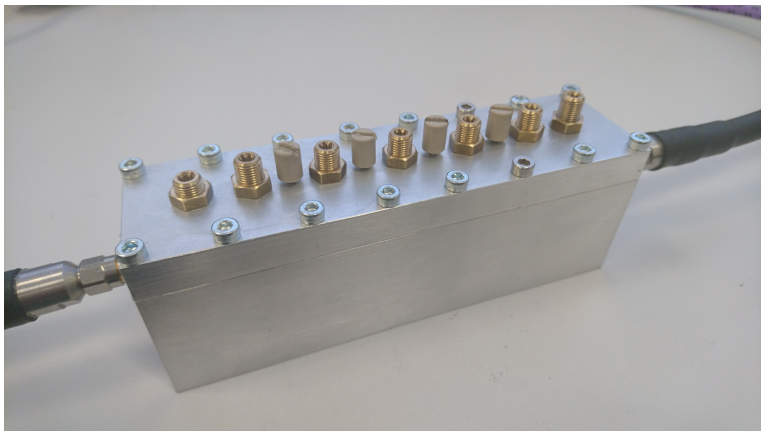

(a) Photograph showing the fabricated fully tunable 5-pole filter

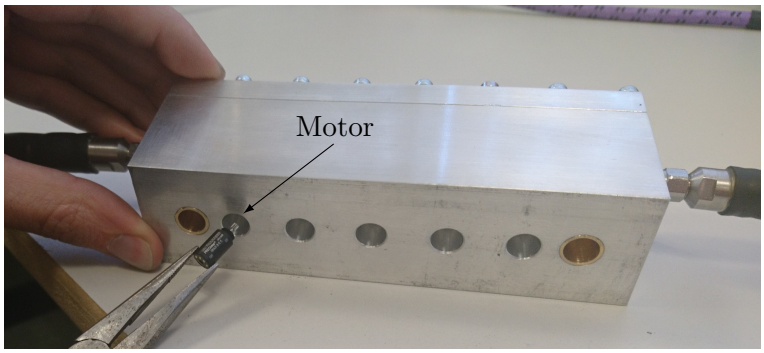

(b) Photograph of a commercially available stepper motor being inserted into a resonator cavity

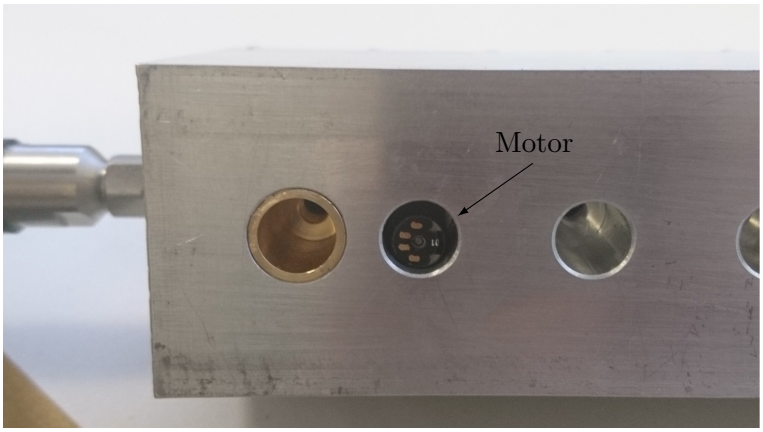

(c) Motor shown inside resonator cavity

Figure 5.43: Fabricated five-pole filter with internal mounting of motor

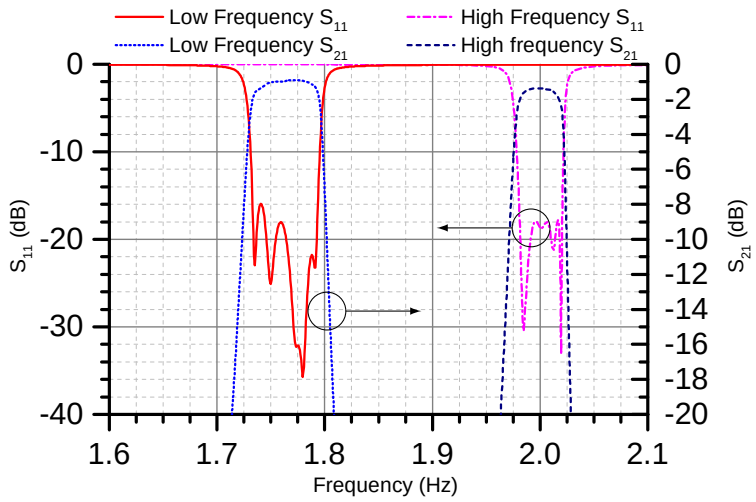

(a) Narrow bandwidth responses

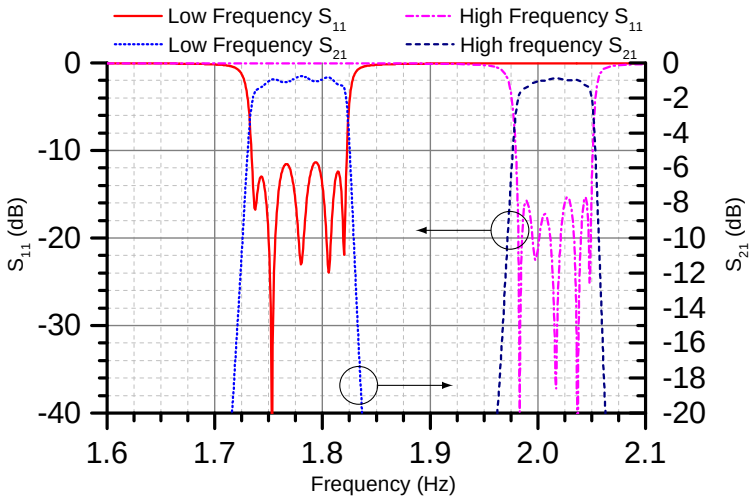

(b) Wide bandwidth responses

Figure 5.44: Measured S-parameter responses for a fifth order filter with centre frequency and bandwidth control.

— pre-transformer, post-transformer, and the transformer itself. Simulation tests were performed using HFSS for various tuning methods at each stage. Visualisation of the tunability was shown via return loss ripple level and bandwidth.

A method of categorising tunability of the individual inter-resonator and external couplings is then used with the intention of designing a tunable filter to a specification. Two filters were then designed, optimised, fabricated and measured. Both filters followed the same design specification of frequency tunability from 1.75 GHz to 2.00 GHz and a bandwidth tuning range from 40 MHz to 60 MHz. The first filter, a simple two-pole design showed good tunability and correlated well with the simulation responses. The second filter followed a similar design procedure, but was of increased complexity — with five resonant elements and four couplings. This filter again showed good centre frequency tunability. It did however suffer due to the limitations of external coupling tunability, which are apparent on the low frequency end of the tuning range. Since the ripple level could not be lowered to the desired 15 dB, larger bandwidths than specified are seen in the measurements. However the desired percentage bandwidth tunability of 50% is still met.

Chapter 6

Conclusions

This research has explored methods for performing bandwidth and centre-frequency tunability of bandpass filters, whilst also maintaining a controllable return loss ripple level. It was shown in the literature that previously explored methods for the application of electronic tunability, such as capacitive diode technologies and micro-electromechanical systems prove to be unable to meet the strict requirements of cellular basestation front end filtering due to issues with linearity and power handling and losses. Tunability provided by mechanical means, at least in contemporary times while transmission power levels are so high, was demonstrated to be the best option for applications of tunable microwave filtering.

Computer modelling and simulation testing of a variety of custom designed mechanism types in a simple combline cavity filter were used in order to build an idea of how the electromagnetic fields interact within the filter. Using this knowledge, the respective fields were then exploited in order to apply a tunable capacitance or inductance at any desired location within the circuit.

Methods for tuning TEM line resonance, external-Q and inter-resonator coupling were developed, quantified and compared with each other for the control of centre-frequency, return loss and bandwidth respectively. Analytical techniques for estimating possible ripple bandwidth achievement from simulated coupling bandwidths were then applied. A combination of the three tuning methods were then implemented simultaneously in two independent filters of differing complexity. First in a second order filter, followed by a fifth order design. Each filter was able to provide the prescribed level of tunability with very minor deviation from the initial specification. The causes of deviations have been identified and given more time can easily be corrected for. The bottleneck for tunability with the designed filters is given by the tuning limits of external-Q.

This work introduces three novelties into a filter design simultaneously. The first, developed in chapter 4, is the method through which bandwidth tunability is realised — using the rotation of a plate between resonators to introduce a tunable capacitance in parallel to the inter-resonator coupling. The second method affords resonance tuning

in the filter. This is provided by screws mounted within resonators (and transformers) which when actuated vertically tune the shunt capacitance to ground of the TEM lines. The third novelty arises as a by-product of the mechanical solution to the frequency tunability method just described. Treating the resonators as hollow cylinders and mounting the actuating screw at a given height leaves a cavity of unused space within the filter footprint. Small motors that drive the actuation for frequency tunability can be mounted in here — thereby incorporating tunability without the need to increase the filter dimensions.

6.1 Supplementary Literature Review

The literature review provided in chapter 3 was performed in 2014. It therefore does not take into account any advances in the field of tunable microwave bandpass filtering since that time. For that reason, a brief review of the work carried out since then will be performed here.

As was concluded in chapter 3, a number of different methods can be implemented in a filter design for the achievement of frequency or bandwidth tunability to be attained. These methods, including but not limited to MEMS, PIN and varactor diodes, were extensively covered. Each was shown to have their own set of drawbacks.

For example, varactor diodes were shown to be able to provide a good tuning range, however they also suffer from high losses and intermodulation distortion. Varactor diodes are useful in planar applications and continue to be extensively researched [64, 65, 66, 67, 68].

Advancing technologies in the fabrication of components has led to the ability to design and realisation of MEMS devices. Although no longer a new technology, there is still some interest in their uses within applications of tunable filtering [69, 70, 71, 72, 73]. That said however, there have been no recent transaction papers published on this topic, only a smattering of conference papers. It could be said that this is indicative of the drawbacks of MEMS devices (such as power handling, fabrication costs and reliability) are still too great for the technology to really take off in tunable filtering applications.

With regards to mechanically tuned filters, additive manufacturing has been employed in waveguide technology to achieve tunability from 5.45 GHz to 5.64 GHz with near constant absolute bandwidth [74].

In Addition to tunable filters, the option for a filter to be reconfigurable can also pose a commercial advantage. Reconfigurability refers to a single piece of hardware being able to provide multiple purposes depending on how it is set up. In [75], a cavity Combline microwave filter is fabricated by the cascading of two asymmetrical filters with no need for isolation between them. Tuning is provided mechanically through the

Work	Tuning Method	Centre Frequency (GHz)	Bandwidth (MHz)	Return Loss (dB)	Insertion Loss (dB)
[64]	Varactor	1.1-1.8	82-97	> 13.5	< 4.3
[65]	Varactor	4.33-6.33	-	-	< 3.5
[66]	Varactor	1.7-2.7	50-110	> 10	< 3.8
[67]	Varactor	0.55-1.1	34-66	> 14	< 2.3
[68]	Varactor	1.5-2.5	-	> 9.5	< 3
[73]	MEMS	7.03-7.18	73-92	-	-
[75]	Mechanical	1.98-2.03	20-25	-	-
[76]	Mechanical	-	11-33	-	-
[77]	Mechanical	2.57-2.63	-	> 16.2	< 2.3
this work	Mechanical	1.764-2.015	41-85	> 11.3	< 1.4

Table 6.1: A comparison of the filter presented in this work to other recently published works.

realignment of tuning screws from the lid.

The results of work described in this section have been compared to the work contained in this thesis in table 6.1. The filter presented in chapter 5 of this work shows a good level of frequency and bandwidth tunability when compared to the similar works. On top of that, it is shown that the insertion loss of this filter provides a 40% improvement (from 2.3 dB to 1.4 dB) on the next best design, despite also having a lower return loss level.

6.2 Future Work

Work on the inter-resonator couplings showed that both the electric and magnetic fields can be exploited with the vertical actuation of a single mechanism in the coupling gap. An extension of this work could look into implementations of this technology without the need for bulky external connections to provide tunability.

It was shown in chapter 4 that for inter-resonator couplings, the inclusion of an iris limits the coupling and therefore allows the same bandwidth requirements to be met with reduced resonator spacings — and therefore a smaller overall filter volume. Controllably altering the size of an iris allows for bandwidth tunability to be acheived, without the need for a component in the coupling gap. Take for example a camera lens diaphragm shutter of a typical digital camera. Installation of this type of shutter in a wall between resonators affords the opportunity to control the size of an iris. Simpler solutions are also possible. The simplest of which would be a screw, or number of screws of a similar diameter to the wall thickness which could open or close holes in the wall, making the coupling stronger or weaker respectively. Exploration of these methods and variations therein would be an interesting avenue of exploration.

The filters designed and fabricated in chapter 5 utilise mechanical actuation in order to achieve the desired tunability. Therefore no active devices are required to be used

for their operation meaning that intermodulation distortion generated is practically zero when compared to varactors, PIN diodes and MEMS. Because of this, testing of IMD was not done on these filters. Passive IMD is a known phenomenon when dealing with high power signals. It occurs due to areas of high current density in a filter, typically due non-ideal electrical connections. Future work could incorporate techniques to minimise passive intermodulation in these designs — silver flushed plating, improved lid connections, blended instead of sharp angled edges and improved connector-transformer contacts are some methods worth exploring in order to optimise intermodulation performance.

Bibliography

[1] J.G. Andrews, S. Buzzi, Wan Choi, S.V. Hanly, A. Lozano, A.C.K. Soong, and J.C. Zhang. What will 5G be? *Selected Areas in Communications, IEEE Journal on*, 32(6):1065–1082, June 2014.

[2] R.R. Mansour, Fengxi Huang, S. Fouladi, W.D. Yan, and M. Nasr. High-Q tunable filters: Challenges and potential. *Microwave Magazine, IEEE*, 15(5):70–82, July 2014.

[3] R. Cameron, C. Kudsia, and R. Mansour. *Microwave Filters for Communications Systems: Fundamentals, Design, and Applications.* John Wiley and sons, 2007.

[4] Ian C. Hunter. *Theory and Design of Microwave Filters.* The Institution of Engineering and Technology, 2001.

[5] R. J. Cameron. General coupling matrix synthesis methods for chebyshev filtering functions. *IEEE Transactions on Microwave Theory and Techniques*, 47(4):433–442, Apr 1999.

[6] W. J. Getsinger. Coupled rectangular bars between parallel plates. *IRE Transactions on Microwave Theory and Techniques*, 10(1):65–72, January 1962.

[7] E. G. Cristal. Coupled circular cylindrical rods between parallel ground planes. *IEEE Transactions on Microwave Theory and Techniques*, 12(4):428–439, Jul 1964.

[8] J.D. Adam, L.E. Davis, Gerald F. Dionne, E.F. Schloemann, and S.N. Stitzer. Ferrite devices and materials. *Microwave Theory and Techniques, IEEE Transactions on*, 50(3):721–737, Mar 2002.

[9] I.C. Hunter and J.D. Rhodes. Electronically tunable microwave bandpass filters. *Microwave Theory and Techniques, IEEE Transactions on*, 30(9):1354–1360, Sep 1982.

[10] J.O Scanlan and R Levy. *Circuit Theory*, volume 1. Oliver & Boyd, 1970.

[11] A.R. Brown and G.M. Rebeiz. A varactor-tuned RF filter. *Microwave Theory and Techniques, IEEE Transactions on*, 48(7):1157–1160, Jul 2000.

[12] S.R Chandler, I.C. Hunter, and J.G. Gardiner. Active varactor tunable bandpass filter. *Microwave and Guided Wave Letters, IEEE*, 3(3):70–71, March 1993.

[13] K. Buisman, L.C.N. de Vreede, L.E. Larson, M. Spirito, A. Akhnoukh, T.L.M. Scholtes, and L.K. Nanver. Distortion-free varactor diode topologies for RF adaptivity. In *Microwave Symposium Digest, 2005 IEEE MTT-S International*, pages 4 pp.–, June 2005.

[14] A. Tombak, J.-P. Maria, F.T. Ayguavives, Zhang Jin, Gregory T. Stauf, Angus I. Kingon, and Amir Mortazawi. Voltage-controlled RF filters employing thin-film barium-strontium-titanate tunable capacitors. *Microwave Theory and Techniques, IEEE Transactions on*, 51(2):462–467, Feb 2003.

[15] Andrei Vorobiev, Pär Rundqvist, Khaled Khamchane, and S Gevorgian. Silicon substrate integrated high q-factor parallel-plate ferroelectric varactors for microwave/millimeterwave applications. *Applied Physics Letters*, 83(15):3144–3146, 2003.

[16] X. Wang, P. Bao, T.J. Jackson, and M.J. Lancaster. Tunable microwave filters based on discrete ferroelectric and semiconductor varactors. *Microwaves, Antennas Propagation, IET*, 5(7):776–782, May 2011.

[17] V.V. Pleskachev and I.B. Vendik. Tunable microwave filters based on ferroelectric capacitors. In *Microwave and Telecommunication Technology, 2003. CriMiCo 2003. 13th International Crimean Conference*, pages 468–470, Sept 2003.

[18] C Y Tan and C K Ong. Planar tunable HTS microwave filter with patterned ferroelectric thin film. *Superconductor Science and Technology*, 19(2):212, 2006.

[19] J. Nath, D. Ghosh, J.-P. Maria, Angus I. Kingon, W. Fathelbab, P.D. Franzon, and M.B. Steer. An electronically tunable microstrip bandpass filter using thin-film Barium-Strontium-Titanate (BST) varactors. *Microwave Theory and Techniques, IEEE Transactions on*, 53(9):2707–2712, Sept 2005.

[20] Yong-Kyu Yoon, Dongsu Kim, M.G. Allen, J.S. Kenney, and A.T. Hunt. A reduced intermodulation distortion tunable ferroelectric capacitor-architecture and demonstration. *Microwave Theory and Techniques, IEEE Transactions on*, 51(12):2568–2576, Dec 2003.

[21] HV Shurner. *Microwave Semiconductor Devices*. Pitman and sons, 1971.

[22] M.F. Karim, Yong-Xin Guo, Z.N. Chen, and L.C. Ong. Miniaturized reconfigurable and switchable filter from UWB to 2.4 GHz WLAN using PIN diodes. In *Microwave Symposium Digest, 2009. MTT '09. IEEE MTT-S International*, pages 509–512, June 2009.

[23] K. Kishino, M.S. Unlu, Jen-Inn Chyi, J. Reed, L. Arsenault, and Hadis Morkoc. Resonant cavity-enhanced (RCE) photodetectors. *Quantum Electronics, IEEE Journal of*, 27(8):2025–2034, Aug 1991.

[24] M.K. Fries, M. Grani, and R. Vahldieck. A reconfigurable slot antenna with switchable polarization. *Microwave and Wireless Components Letters, IEEE*, 13(11):490–492, Nov 2003.

[25] Y.J. Sung, T.U. Jang, and Y.-S. Kim. A reconfigurable microstrip antenna for switchable polarization. *Microwave and Wireless Components Letters, IEEE*, 14(11):534–536, Nov 2004.

[26] D. Peroulis, K. Sarabandi, and L.P.B. Katehi. Design of reconfigurable slot antennas. *Antennas and Propagation, IEEE Transactions on*, 53(2):645–654, Feb 2005.

[27] Fan Yang and Y. Rahmat-Samii. A reconfigurable patch antenna using switchable slots for circular polarization diversity. *Microwave and Wireless Components Letters, IEEE*, 12(3):96–98, March 2002.

[28] Z. Brito-Brito, I. Llamas-Garro, G. Navarro-Muñoz, J. Perruisseau-Carrier, L. Pradell, F. Giacomozzi, and S. Colpo. Precise frequency and bandwidth control of switchable microstrip bandpass filters using diode and microelectro-mechanical system technologies. *Microwaves, Antennas Propagation, IET*, 6(6):713–719, April 2012.

[29] Jr. Lugo, C. and J. Papapolymerou. Electronic switchable bandpass filter using pin diodes for wireless low cost system-on-a-package applications. *Microwaves, Antennas and Propagation, IEE Proceedings*, 151(6):497–502, Dec 2004.

[30] G.M. Rebeiz, K. Entesari, I. Reines, S.-J. Park, M.A. El-Tanani, A. Grichener, and A.R. Brown. Tuning in to RF MEMS. *Microwave Magazine, IEEE*, 10(6):55–72, Oct 2009.

[31] E.R. Brown. RF MEMS switches for reconfigurable integrated circuits. *Microwave Theory and Techniques, IEEE Transactions on*, 46(11):1868–1880, Nov 1998.

[32] D. Peroulis, S. Pacheco, K. Sarabandi, and L.P.B. Katehi. Tunable lumped components with applications to reconfigurable MEMS filters. In *Microwave Symposium Digest, 2001 IEEE MTT-S International*, volume 1, pages 341–344 vol.1, May 2001.

[33] G.M. Rebeiz and Jeremy B. Muldavin. RF MEMS switches and switch circuits. *Microwave Magazine, IEEE*, 2(4):59–71, Dec 2001.

[34] Abbas Abbaspour-Tamijani, L. Dussopt, and G.M. Rebeiz. Miniature and tunable filters using MEMS capacitors. *Microwave Theory and Techniques, IEEE Transactions on*, 51(7):1878–1885, July 2003.

[35] Chuang yuan Lee and Eun Sok Kim. Piezoelectrically actuated tunable capacitor. *Microelectromechanical Systems, Journal of*, 15(4):745–755, Aug 2006.

[36] D. Girbau, Nerea Otegi, L. Pradell, and A. Lazaro. Study of intermodulation in RF MEMS variable capacitors. *Microwave Theory and Techniques, IEEE Transactions on*, 54(3):1120–1130, March 2006.

[37] L. Dussopt and G.M. Rebeiz. Intermodulation distortion and power handling in RF MEMS switches, varactors, and tunable filters. *Microwave Theory and Techniques, IEEE Transactions on*, 51(4):1247–1256, Apr 2003.

[38] F. Martin, F. Falcone, J. Bonache, T. Lopetegi, M. A. G. Laso, and M. Sorolla. Dual electromagnetic bandgap cpw structures for filter applications. *IEEE Microwave and Wireless Components Letters*, 13(9):393–395, Sept 2003.

[39] F. R. Yang, Y. Qian, and T. Itoh. A novel compact microstrip band pass filter with intrinsic spurious suppression. In *Asia Pacific Microwave Conference (APMC)*, pages 593–596, Dec 1998.

[40] T. Lopetegi, M. A. G. Laso, J. Hernandez, M. Bacaicoa, D. Benito, M. J. Garde, M. Sorolla, and M. Guglielmi. New microstrip ldquo;wiggly-line rdquo; filters with spurious passband suppression. *IEEE Transactions on Microwave Theory and Techniques*, 49(9):1593–1598, Sep 2001.

[41] R. Coccioli, Fei-Ran Yang, Kuang-Ping Ma, and T. Itoh. Aperture-coupled patch antenna on uc-pbg substrate. *IEEE Transactions on Microwave Theory and Techniques*, 47(11):2123–2130, Nov 1999.

[42] Young-Taek Lee, Jong-Sik Lim, Jun-Seok Park, D. Ahn, and Sangwook Nam. A novel phase noise reduction technique in oscillators using defected ground structure. *IEEE Microwave and Wireless Components Letters*, 12(2):39–41, Feb 2002.

[43] J. Garcia-Garcia, F. Martin, F. Falcone, J. Bonache, I. Gil, T. Lopetegi, M. A. G. Laso, M. Sorolla, and R. Marques. Spurious passband suppression in microstrip coupled line band pass filters by means of split ring resonators. *IEEE Microwave and Wireless Components Letters*, 14(9):416–418, Sept 2004.

[44] Z. C. Hao and J. S. Hong. Ultrawideband filter technologies. *IEEE Microwave Magazine*, 11(4):56–68, June 2010.

[45] J. Garcia-Garcia, J. Bonache, and F. Martin. Application of electromagnetic bandgaps to the design of ultra-wide bandpass filters with good out-of-band performance. *IEEE Transactions on Microwave Theory and Techniques*, 54(12):4136–4140, Dec 2006.

[46] Y. Guo, S. Kim, X. Liu, H. Gao, and G. P. Li. A compact configurable ebg filter on pcb. *IEEE Transactions on Components, Packaging and Manufacturing Technology*, 5(5):668–674, May 2015.

[47] L. Kurra, M. P. Abegaonkar, A. Basu, and S. K. Koul. Switchable and tunable notch in ultra-wideband filter using electromagnetic bandgap structure. *IEEE Microwave and Wireless Components Letters*, 24(12):839–841, Dec 2014.

[48] M. F. Karim, A. Q. Liu, L. C. Ong, and Y. X. Guo. Micromachined based narrow band fabry-perot tunable bandpass filter. *IET Microwaves, Antennas Propagation*, 6(5):562–568, April 2012.

[49] Z. L. Deng, N. B. Zhang, and J. M. Huang. A tunable ultra-wideband band-stop filter based on ebg structures using mems technology. In *2009 International Conference on Mechatronics and Automation*, pages 3579–3583, Aug 2009.

[50] B. Majumder, K. Krishnamoorthy, J. Mukherjee, and K. P. Ray. A compact electromagnetic band gap ground controlled tunable dual mode band pass filter. In *2014 16th International Symposium on Antenna Technology and Applied Electromagnetics (ANTEM)*, pages 1–2, July 2014.

[51] H. Tang, J. X. Chen, L. H. Zhou, and Z. H. Bao. Tunable dual-mode microstrip patch resonators and filters. *IET Microwaves, Antennas Propagation*, 7(6):408–414, April 2013.

[52] José Carlos Pedro and Nuno Borges Carvalho. *Intermodulation Distortion in Microwave and Wireless Circuits*. Artech House, 2002.

[53] Motorola Inc. *Technical datasheet: Silicon hyper-abrupt tuning diodes*, 1997.

[54] R. Levy, R.V. Snyder, and G. Matthaei. Design of microwave filters. *Microwave Theory and Techniques, IEEE Transactions on*, 50(3):783–793, Mar 2002.

[55] Jia-Shen G Hong and Michael J Lancaster. *Microstrip filters for RF/microwave applications*, volume 167. John Wiley & Sons, 2004.

[56] Terry Edwards. *Foundations of Microstrip Circuit Design*. John Wiley & sons, 1992.

[57] Brian C Wadell. *Transmission Line Design Handbook*. Artech House, 1991.

[58] F.W. Grover. *Inductance Calculations: working formulas and tables*. Dover, NY, 1962.

[59] P. Krulevitch, A. P. Lee, P. B. Ramsey, J. C. Trevino, J. Hamilton, and M. A. Northrup. Thin film shape memory alloy microactuators. *Journal of Microelectromechanical Systems*, 5(4):270–282, Dec 1996.

[60] Morten Hagensen. *Narrowband Microwave Bandpass Filter Design by Coupling Matrix Synthesis*. Guided Wave Technology ApS, Hilleroed, Denmark, 2010.

[61] R. J. Cameron. Advanced coupling matrix synthesis techniques for microwave filters. *IEEE Transactions on Microwave Theory and Techniques*, 51(1):1–10, Jan 2003.

[62] S. Yamashita M. Makimoto. *Microwave Resonators and Filters for Wireless Communication: Theory, Design and Application*. Springer, 2000.

[63] Faulhaber stepper motor series 0620. `https://www.faulhaber.com/en/products/series/dm0620/`. Online: accessed August 2017.

[64] Z. Zhao, J. Chen, L. Yang, and K. Chen. Three-pole tunable filters with constant bandwidth using mixed combline and split-ring resonators. *IEEE Microwave and Wireless Components Letters*, 24(10):671–673, Oct 2014.

[65] F. S. Su, Y. M. Chen, and S. F. Chang. Packaged tunable combline bandpass filters. *IEEE Microwave Magazine*, 16(2):93–98, March 2015.

[66] P. L. Chi, T. Yang, and T. Y. Tsai. A fully tunable two-pole bandpass filter. *IEEE Microwave and Wireless Components Letters*, 25(5):292–294, May 2015.

[67] A. Anand and X. Liu. Reconfigurable planar capacitive coupling in substrate-integrated coaxial-cavity filters. *IEEE Transactions on Microwave Theory and Techniques*, 64(8):2548–2560, Aug 2016.

[68] T. Palomo and G. Mumcu. Microfluidically reconfigurable microstrip line combline filters with wide frequency tuning capabilities. *IEEE Transactions on Microwave Theory and Techniques*, 65(10):3561–3568, Oct 2017.

[69] S. Sirci, J. D. Martnez, R. Stefanini, P. Blondy, and V. E. Boria. Compact smd packaged tunable filter based on substrate integrated coaxial resonators. In *2014 IEEE MTT-S International Microwave Symposium (IMS2014)*, pages 1–4, June 2014.

[70] K. Chun, S. Kim, and J. Kim. Rf devices for reconfigurable transceiver system. In *Proceedings of 2014 3rd Asia-Pacific Conference on Antennas and Propagation*, pages 1316–1319, July 2014.

[71] K. Savin, I. Golubeva, and Y. Prokopenko. A novel concept for the tunable cavity combline resonator. In *2015 IEEE 35th International Conference on Electronics and Nanotechnology (ELNANO)*, pages 520–522, April 2015.

[72] A. J. Alazemi and G. M. Rebeiz. A low-loss 1.4-2.1 ghz compact tunable three-pole filter with improved stopband rejection using rf-mems capacitors. In *2016 IEEE MTT-S International Microwave Symposium (IMS)*, pages 1–4, May 2016.

[73] J. Jiang and R. R. Mansour. High-q tunable filter with a novel tuning structure. In *2016 46th European Microwave Conference (EuMC)*, pages 1365–1368, Oct 2016.

[74] A. Perigaud, O. Tantot, N. Delhote, S. Bila, S. Verdeyme, and D. Baillargeat. Continuously tunable filter made by additive manufacturing using a 3d spiral ribbon. In *2017 IEEE MTT-S International Microwave Workshop Series on Advanced Materials and Processes for RF and THz Applications (IMWS-AMP)*, pages 1–3, Sept 2017.

[75] M. Yuceer. A reconfigurable microwave combline filter. *IEEE Transactions on Circuits and Systems II: Express Briefs*, 63(1):84–88, Jan 2016.

[76] A. I. Abunjaileh and I. C. Hunter. Combline filter with tunable bandwidth and centre frequency. In *2010 IEEE MTT-S International Microwave Symposium*, pages 1476–1479, May 2010.

[77] S. Fouladi, F. Huang, W. D. Yan, and R. R. Mansour. High-q narrowband tunable combline bandpass filters using mems capacitor banks and piezomotors. *IEEE Transactions on Microwave Theory and Techniques*, 61(1):393–402, Jan 2013.